

**A New Design of an UHV-  
High- $T_c$ -SQUID Magnetometer:  
Absolute Determination of  
Magnetic Moments of  
 $3d$ -Transition Metal Films**

im Fachbereich Physik  
der Freien Universität Berlin  
eingereichte Dissertation

vorgelegt von  
**Andreas Ney**  
aus  
Bad Homburg v.d.H.

Mai 2001

**dissertation.de - Verlag im Internet GmbH**

Sonderausgabe des Werkes mit der ISBN /

Special edition of the book with the ISBN:

3-89825-311-2

Tag der Disputation:

9.Juli 2001

1.Gutachter:

Prof. Dr. K. Baberschke

2.Gutachter:

Prof. Dr. P. Fumagalli

**dissertation.de - Verlag im Internet GmbH**

Pestalozzistr. 9

10 625 Berlin

URL:

<http://www.dissertation.de>

To my parents

# Abstract

A novel magnetometer based on a commercial high- $T_c$  SQUID sensor has been designed, constructed, and installed at an ultrahigh vacuum (UHV) chamber to perform magnetic measurements on ultrathin films *in statu nascendi*. The novel magnetometer is easy to handle, cost-effective, and enables measurements of the magnetization of ferromagnetic samples with high precision and submonolayer sensitivity within a few minutes. The magnetometer provides magnetic information on an absolute scale after calibrating once by applying Biot-Savart's law. First results of temperature- and thickness-dependent measurements of Co films grown on a Cu(001) single crystal are presented. The temperature was ranged from 300 to 40 K. The film thickness was chosen between 1.3 and 17 monolayers. The measurements reveal a bulk-like magnetization of 1480 kA/m at the thick film limit which is translated into magnetic moment per atom by extrapolating the temperature-dependent data to  $T = 0$  K yielding  $1.73\mu_B/\text{atom}$ . At the thin film limit (2 monolayers) the magnetic moment is enhanced by 10% to  $1.89(5)\mu_B/\text{atom}$ . The enhancement is attributed to interface effects since the magnetic moment depends linearly on the inverse film thickness  $1/d$ . Spin and orbital magnetic moments can be separated by combining the experimental findings of the novel UHV-SQUID magnetometer with measurements of the x-ray magnetic circular dichroism. The enhancement at the thin film limit originates mainly from a strong increase of the orbital moment by a factor of two due to significant unquenching caused by the reduced symmetry at the surface. By replacing the vacuum-facing interface by a Cu-facing one, i.e. by capping the films with Cu, it is possible to separate interface and surface contributions to the magnetic moment. It will be demonstrated that the surface atoms carry an enhanced moment of  $2.28(8)\mu_B$  while the interface atoms have reduced moments of  $1.43(5)\mu_B$ . Magnetization measurements were performed below 2 monolayers of Co as well. Due to the submonolayer sensitivity and the access to low temperatures it was possible to study metastable magnetic properties at the initial stage of growth of Co/Cu(001).

The UHV-SQUID is able to measure ultrathin Ni films as well, which only possesses 1/3 of the magnetic moment of Co. This was done before and after capping with a protective Cu layer. The magnetization is found to be bulk-like between 4 and 9 monolayers film thickness. For a 9 monolayer thick Ni/Cu(001)

film the easy axis of the magnetization turns from in-plane to out-of-plane upon Cu capping since this film is just below the well-known spin reorientation transition for this system. The reduction of the magnetization caused by a Cu cap is negligible above a film thickness of 5 monolayers, whereas a reduction by 21% is found at 4 monolayers. These results encourage to carry out further measurements on this system and demonstrate the ultimate sensitivity of the novel UHV-SQUID magnetometer.

# Contents

<b>Abstract</b>	<b>iv</b>
<b>Introduction</b>	<b>ix</b>
<b>1 General remarks on ferromagnetism</b>	<b>1</b>
1.1 Magnetization and magnetic moment . . . . .	1
1.2 Ferromagnetism in reduced dimensions . . . . .	4
1.3 $T_C(d)$ and $M(T)$ at low temperatures . . . . .	7
1.4 Contributions to the total magnetic moment . . . . .	9
1.4.1 Spin dependent interactions in EPR . . . . .	10
1.4.2 Formfactors and current densities in PND . . . . .	12
1.4.3 The XMCD sum rules . . . . .	15
1.4.4 The role of the $\langle T_z \rangle$ term . . . . .	17
<b>2 Different types of Magnetometry</b>	<b>20</b>
2.1 MOKE . . . . .	20
2.2 XMCD . . . . .	21
2.3 PNR . . . . .	22
2.4 AGM/cantilever . . . . .	23
2.5 TOM . . . . .	24
2.6 MFM . . . . .	26
2.7 SQUIDs . . . . .	26
2.7.1 Principles of operation . . . . .	27
2.7.2 UHV-compatible setups . . . . .	29
<b>3 Experimental details</b>	<b>32</b>
3.1 Design of the UHV-SQUID magnetometer . . . . .	32
3.1.1 The SQUID sensor . . . . .	33
3.1.2 The UHV-compatible metal dewar . . . . .	34
3.1.3 The sample holder . . . . .	36
3.2 Operation of the magnetometer . . . . .	38
3.2.1 Calibration . . . . .	38
3.2.2 Data acquisition . . . . .	40

3.2.3	The ultimate sensitivity . . . . .	41
3.3	Analysis of the data . . . . .	42
3.3.1	The measuring geometry . . . . .	42
3.3.2	Calculated stray field . . . . .	43
3.3.3	Spatial resolution of the magnetometer . . . . .	45
3.3.4	Determination of the parameters . . . . .	47
3.4	Sample preparation . . . . .	51
<b>4</b>	<b>The system Co/Cu(001)</b>	<b>53</b>
4.1	Structural and magnetic properties . . . . .	53
4.1.1	Growth of Co on Cu(001) . . . . .	54
4.1.2	Sudden increase of $T_C$ . . . . .	54
4.1.3	Magnetic moments from literature . . . . .	56
4.2	Thickness dependence of $M$ . . . . .	60
4.2.1	Thick films . . . . .	60
4.2.2	The effect of the measuring temperature . . . . .	62
4.3	Deconvolution of $\mu_S$ and $\mu_L$ . . . . .	64
4.3.1	Magnetic moments . . . . .	64
4.3.2	Origin of the enhanced $M$ . . . . .	67
4.3.3	The $\langle T_z \rangle$ -term . . . . .	68
4.4	Magnetic moment profile of Co/Cu(001) . . . . .	70
4.4.1	The influence of Cu capping . . . . .	70
4.4.2	The separation of surface and interface moments . . . . .	72
4.5	Films below 2 ML . . . . .	75
<b>5</b>	<b>The system Ni/Cu(001)</b>	<b>81</b>
5.1	Structural and magnetic properties of Ni/Cu(001) . . . . .	81
5.2	First results for capped and uncapped Ni films . . . . .	82
	<b>Conclusion and Outlook</b>	<b>88</b>
<b>A</b>	<b>Drawings of the magnetometer</b>	<b>90</b>
A.1	The UHV-compatible metal dewar . . . . .	91
A.2	The $\mu$ -metal shielding . . . . .	92
A.3	The glass finger tip . . . . .	93
A.4	The sample holder (parts) . . . . .	94
<b>B</b>	<b>Motor control unit</b>	<b>95</b>
B.1	Main power supply . . . . .	96
B.2	Bipolar power supply for the motor drive . . . . .	97
B.3	Trigger unit and voltage bisection . . . . .	98
B.4	Plug assembly . . . . .	99

<b>C Computer programs</b>	<b>100</b>
C.1 Programs to calculate the stray field . . . . .	100
C.2 Programs to control the AD-DA card . . . . .	104
<b>Bibliography</b>	<b>118</b>
<b>List of Publications</b>	<b>119</b>
<b>Acknowledgments</b>	<b>122</b>
<b>Curriculum vitae</b>	<b>124</b>
<b>Zusammenfassung</b>	<b>126</b>

# Introduction

Although magnetism was known to the ancients, it is still impossible to provide a complete theory describing all its phenomena. In the early decades of the 20<sup>th</sup> century, quantum mechanics has offered the first theoretical explanation of the origin of ferromagnetism by introducing the exchange interaction which has no classical analogon. However, magnetism was used for practical applications, especially magnetic recording, without understanding the underlying details of its nature. Today's progress in computer technology pushes the magnetic recording towards highest possible bit-density and therefore to nanometer-scaled ferromagnetic materials. This progress is not only of practical interest. The need to have fundamental insight into the mechanisms behind ferromagnetism urges to fabricate ideal-like systems with reduced dimensions as well since they exhibit magnetic properties which strongly differ from three-dimensional bulk crystals.

In the last decades large progress has been made in both fields, experiment and theory. One topic of major interest is the magnetism of ultrathin films. In the early days, according to the theorem of Mermin and Wagner [1], it was predicted that an isotropic two-dimensional (2D) Heisenberg system would exhibit no long range magnetic order above  $T = 0$ . Later-on, it was shown that anisotropy may stabilize ferromagnetic order in such systems at finite temperatures ( $T > 0$  K) [2]. Nowadays many 2D systems are known to be in a ferromagnetic state [3] and a large variety of new phenomena has been discussed [4]. A lot of experimental effort is required to study 2D systems quantitatively: Ultrahigh vacuum (UHV) is needed for cleanness and time-stability of the prepared systems. Highly sensitive magnetometers and access to low temperatures must be available to gain information about the ground-state properties of the studied ideal-like system. The findings can be compared to state-of-the-art *ab initio* calculations which nowadays are able to calculate even small fractions ( $\leq 10^{-6}$ ) of the total energy with high accuracy. This is crucial because the magnetic anisotropy energy is in the order of  $\mu\text{eV}/\text{atom}$  while the total energy is about  $\text{eV}/\text{atom}$ .

In this work a novel SQUID magnetometer is introduced. The acronym SQUID stands for "superconducting quantum interference device". The applications of the Josephson effect [5] and the concepts of a SQUID have been described in detail [6, 7]. SQUIDs are able to detect even small fractions ( $\sim 10^{-5}$ ) of the flux quantum  $\Phi_0 = 2.07 \cdot 10^{-15}$  wb (Weber) [6], which means that SQUIDs are

the most sensitive magnetometers. They became commercially available about 30 years ago. This work deals with a commercial high- $T_c$  SQUID magnetometer which is combined with a standard UHV chamber to enable *in situ* magnetometry on ultrathin films.

*In situ* magnetometry provides valuable information about magnetic systems, e.g. their macroscopic properties like Curie temperature, anisotropy, and magnetization. These quantities serve for a deeper understanding of the onset of ferromagnetism in reduced dimensions. The possibility to do this inside an UHV chamber permits to study magnetism of ultrathin films during the growth, in dependence of the preparation conditions, and the changes due to protective layers, gas contamination or other magnetic overlayers [8].

This work is structured as follows: Chapter **1** provides a brief overview of basic aspects of magnetism, especially of ferromagnetism in reduced dimensions. The separation of spin and orbital magnetic moment is discussed in detail with respect to polarized neutron diffraction and x-ray magnetic circular dichroism. Chapter **2** summarizes the most common techniques to measure the magnetization *in situ* in UHV.

The experimental aspects of the novel UHV-SQUID magnetometer are given in Chapter **3**. It describes how to calibrate and handle the magnetometer. The sensitivity limit and the data analysis will be discussed. More technical details, drawings, and the computer programs used for the data acquisition can be found in the Appendix.

The main experimental results are presented in Chapter **4**. First the known properties of the system Co/Cu(001) are summarized. A detailed magnetometric study of Co/Cu(001) is performed by thickness- and temperature-dependent measurements. This reveals a complete set of ground-state magnetic moments ranging from bulk-like films to the monolayer. Separation into spin and orbital moment is achieved by using former results of the ratio of both contributions. Taking advantage of the abilities of an UHV magnetometer the influence of subsequent Cu capping on the magnetic moment is studied. This permits to separate surface and interface magnetic moments of Co/Cu(001) films. Moreover a metastable magnetic behavior below 2 monolayers film thickness is found.

First low temperature measurements of system Ni/Cu(001) between 4 and 9 monolayers with and without Cu cap are summarized in Chapter **5**.

# Chapter 1

## General remarks on ferromagnetism

This introductory chapter summarizes the aspects of magnetism which are relevant to perform magnetometric measurements. It is focussed on ferromagnetism of solids since the present work mainly deals with magnetic films solely consisting of few atomic layers. The magnetic observables and their behavior with respect to temperature and dimensionality are described. Finally, the separation of the magnetic moment into its contributing parts – namely the spin and the orbital moment – is discussed.

### 1.1 Magnetization $M$ and magnetic moment $\mu$

The most fundamental magnetic observable is the magnetic moment  $\mu$  itself.<sup>1</sup> In the case of a free atom  $\mu$  consists of three contributions: (i) the intrinsic spin  $\mathbf{S}$  of the particles, (ii) the motion of the electrons (orbital moment) and (iii) the change in the angular momentum of the motion of the electrons due to an external field [9]. (iii) is a general property of each material and the magnetic moment is induced *antiparallel* to the external magnetic field. This phenomenon is called *diamagnetism* and is temperature-independent (see Fig. 1.1, dashed negative line). This is the only magnetic response for atoms with completely filled shells. Some materials possess intrinsic magnetic moments (e.g. originating from unpaired electrons) which align *parallel* to an external magnetic field. This is termed *paramagnetic* behavior. For example, the  $\text{O}_2$  molecule or  $\text{Cr}^{3+}$ -impurities in a solid are paramagnetic. There exist three contributions to paramagnetism. One is the so-called Pauli paramagnetism, which is temperature-independent and is caused by the conduction electrons of a metal (dotted line in Fig. 1.1). The

---

<sup>1</sup>The magnetic moment  $\boldsymbol{\mu}$  and the magnetization  $\mathbf{M}$  are vectors. In the following it will be assumed that the direction is known. Therefore it will always be referred to the absolute value  $M = |\mathbf{M}|$ .

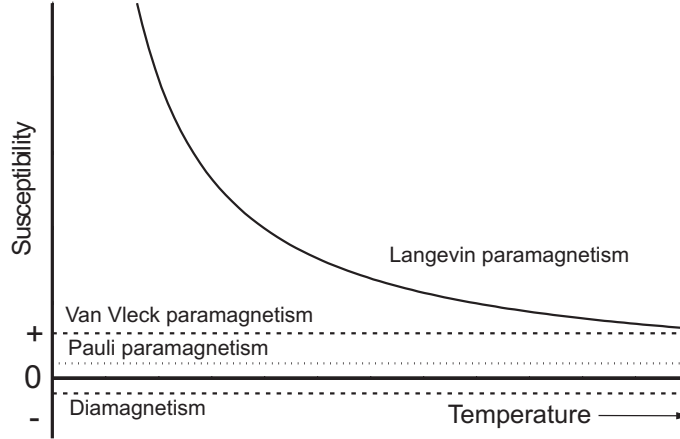


**Figure 1.1:** Magnetic susceptibility  $\chi = M/H$  as a function of temperature [9]. The Pauli paramagnetism originates from the conduction electrons in metals, the Langevin paramagnetism is caused by permanent magnetic moments.

so-called van Vleck paramagnetism is temperature-independent as well (dashed positive line in Fig. 1.1). It is described in first-order perturbation theory when a higher paramagnetic state mixes with the non-magnetic ground state due to a weak external field. The third one is the Langevin paramagnetism which depends on the temperature. It is attributed to localized magnetic moments which ideally would order at  $T = 0$  K; in fact, they order around  $T \sim 1 - 5$  K due to dipolar interactions. In case the intrinsic moments are not aligned randomly in zero external field but exhibit some long-range order below a certain finite temperature this system is called antiferromagnetic (e.g.  $\text{MnO}_2$ ) if the moments completely compensate each other, ferrimagnetic (e.g.  $\text{MnFe}_2\text{O}_4$ ) if they partly compensate, or ferromagnetic (e.g. Fe, Co, Ni, Gd), if they all align parallel.

The permanent magnetic moments  $\mu$  of a paramagnet are no longer arranged randomly if an external field  $H$  is applied. This results in a finite magnetization  $M$ . The response function of  $M$  with respect to  $H$  is the zero-field-susceptibility  $\chi$ :

$$\chi = \left. \frac{\partial M}{\partial H} \right|_{H \rightarrow 0} \quad (1.1)$$

The temperature dependence of the susceptibility is described by the Weiss law:

$$\chi(T) = \frac{C}{T} \quad (1.2)$$

where  $C$  is the Curie constant:

$$C = \frac{N \cdot \mu_0 \mu^2}{3k_B} \quad (1.3)$$

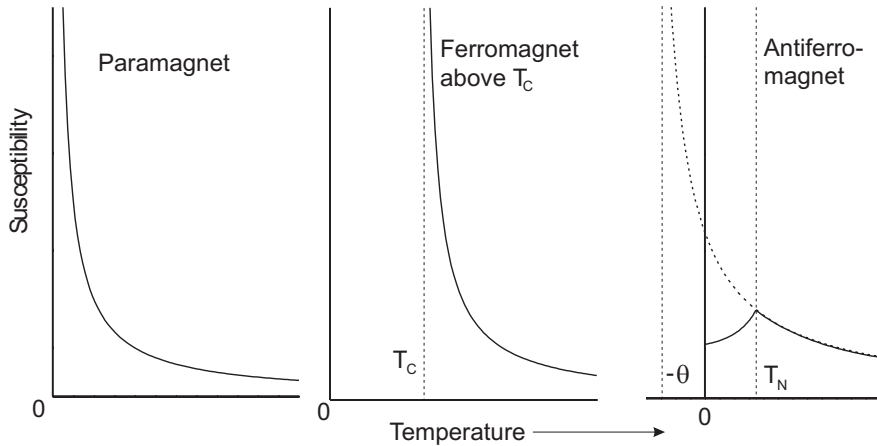


**Figure 1.2:** Susceptibility of a paramagnet, a ferromagnet above  $T_C$  and an antiferromagnet according to [9]. The susceptibility of a ferromagnet below  $T_C$  follows a complicated behavior. An antiferromagnet above  $T_N$  behaves like a ferromagnet with negative Curie temperature  $\theta$ . At  $T_N$  the susceptibility reaches its maximum and drops again forming a kink.

The Curie constant contains the squared magnetic moment  $\mu^2 = \mu(\mu + 1)$  (the “quantum mechanical” square!), the number of atoms  $N$ , and  $\mu_0$ , the permeability of the vacuum, and Boltzmann’s constant  $k_B$ . The temperature dependence of the susceptibility of a paramagnet according to eq. (1.2), is sketched in Fig. 1.2. It should be noted that  $M$  is proportional to  $\mu$  whereas  $\chi$  is related to  $\mu^2$ .

Eq. (1.3) implies that a paramagnetic material possesses a magnetic moment  $\mu$ , but – according to eqs. (1.1) and (1.2) – no magnetization  $M$  can be observed at finite temperatures in zero field. In contrary, ferromagnets exhibit a long-range order of the magnetic moments in zero external field up to a certain finite temperature, the Curie temperature  $T_C$ , resulting in a finite magnetization  $M$ . This is caused by the quantum-mechanical exchange interaction, an interplay of the Coulomb interaction and the Pauli principle. In the Heisenberg model the exchange interaction  $H_{ex}$  between two spins  $\mathbf{S}$  is given by

$$H_{ex} = -2J\mathbf{S}_i \cdot \mathbf{S}_j \quad (1.4)$$

where  $J$  is the exchange integral. In a phenomenological approach this interaction is described with the help of a strong internal magnetic field, the so-called Weiss field. Then, the susceptibility of a ferromagnet above its Curie temperature  $T_C$  is given by the Curie-Weiss law as sketched in Fig. 1.2:

$$\chi(T) = \frac{C}{T - T_C} \quad (1.5)$$

Above  $T_C$  a ferromagnet becomes paramagnetic and therefore, has a magnetic moment  $\mu$ , but it shows no magnetization  $M$ . In the case of an antiferromagnet

Element	$M(T = 0)$	$\mu$ per atom	$T_C$
Fe	1740 kA/m	$2.22 \mu_B$	1043 K
Co	1446 kA/m	$1.72 \mu_B$	1388 K
Ni	510 kA/m	$0.606 \mu_B$	627 K

**Table 1.1:** The ferromagnetic properties of the 3d-transition metals according to [9].

the critical temperature is called Néel temperature ( $T_N$ ) which shows up as a kink in the susceptibility (see Fig. 1.2).

In a first approximation, the magnetic moment is temperature-independent (which is not true over a wide temperature range, e.g. across the melting temperature) while the magnetization is temperature-dependent. To determine the magnetic moment  $\mu$  which is a ground-state property, it is necessary to measure  $M$  for  $T \rightarrow 0$  K so that the moments are all aligned parallel. At finite temperatures, the magnetic moments start to precess/fluctuate and only a thermal average of the magnetic moment is measurable. Therefore the observable magnetization reduces with increasing temperature. At  $T_C$  only the magnetization  $M$  vanishes but not the magnetic moment  $\mu$ . For the itinerant 3d-transition metals the ferromagnetic properties are summed up in Table 1.1. It should be noted that the values in the literature differ by about 1% due to finite experimental accuracy, e.g. for hcp Co between  $1.71$  and  $1.73\mu_B/\text{atom}$ , see Fig. 1.3 and [10].

## 1.2 Ferromagnetism in reduced dimensions

The ferromagnetic properties of a system are correlated with its dimensionality. In principle, there exist four different dimensions which can be studied. The two limiting cases are 0D and 3D – atom and solid. The magnetic moment of a free atom can be calculated using [11]:

$$\mu = g \cdot \sqrt{J(J+1)} \quad (1.6)$$

where  $g$  is the so-called Landé factor and  $J$  the total moment. The Landé factor is given by [11]:

$$g = 1 + \frac{J(J+1) + S(S+1) - L(L+1)}{2J(J+1)} \quad (1.7)$$

This is only valid if the atom is in its Russel-Saunders ground state, i.e.  $L$  and  $S$  are good quantum numbers and they are coupled like  $J = L + S$ . For Co  $S = 3/2$  and  $L = 3$  and – applying Hund's 1<sup>st</sup> and 2<sup>nd</sup> rule –  $J = 9/2$ . Using eq. (1.7) the Landé factor is  $8/6$ . With eq. (1.6) one derives  $6.63\mu_B$  for the free Co atom. This case is mostly studied on paramagnetic impurities in a solid. They exhibit

no long-range order, i.e. observable  $M$ , in zero field at finite temperatures, but their magnetic moment  $\mu$  is widely studied, as in [12]. However, the measured value of  $\mu$  of  $\text{Co}^{2+}$  impurities is about  $4.8\mu_B$  depending on the studied system [13]. The reason is that the orbital moment is partly quenched due to the high symmetry of the surrounding atoms, e.g. [11].

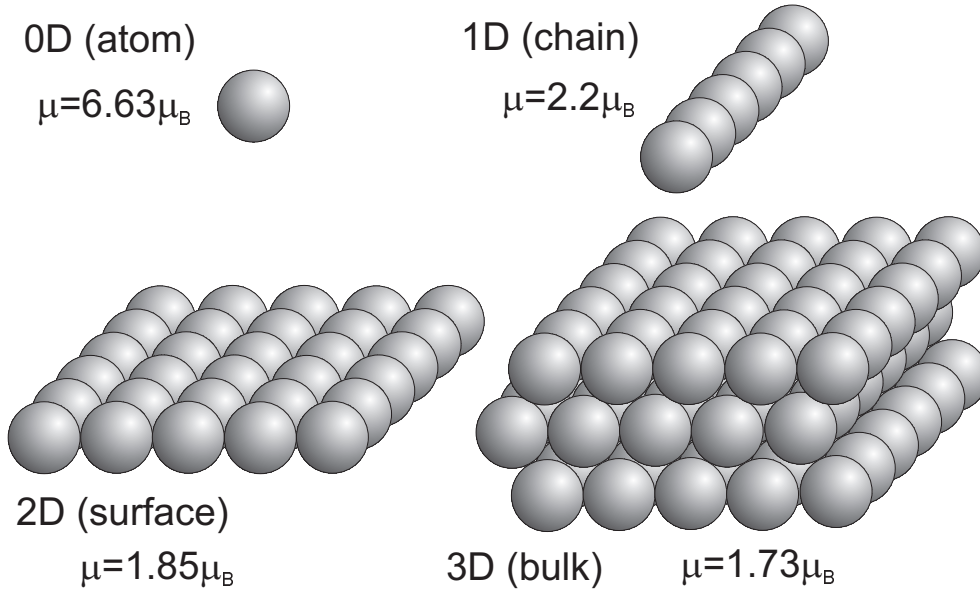


**Figure 1.3:** Evolution of the magnetic moment per atom with respect to the dimensionality of the system. The values for the chain and for the surface are theoretical ones [14] and [15]. The moment of the atom is calculated according to Hund's rules; the bulk value is an experimental one taken from [10].

In theoretical models it was predicted that the magnetic moment per atom decreases step-by-step from a single atom to a chain, to a surface and, finally, to a solid [15]. The magnetic moment which is carried by a paramagnetic Co atom is  $6.63\mu_B$  according to Hund's rules (see above). It should be noted that discussing magnetic moments with respect to dimensionality, the authors quite often refer to the pure spin magnetic moment of the single atom, e.g. in [15, 16]. This is certainly not correct since the orbital contribution is not a small quantity: for the case of Co atom the spin moment is  $3\mu_B$  while the total moment is  $6.63\mu_B$ .

If free atoms are lined up to a one dimensional chain the atoms tend to form electronic bands and therefore the magnetic moments are affected. Theoretical calculations predict a value of  $\sim 2.2\mu_B/\text{atom}$  [14]. Forming a surface, more neighboring atoms are added and the magnetic moment is predicted to further decrease down to  $1.89\mu_B/\text{atom}$  [15]. In a three-dimensional bulk crystal with high symmetry the orbital magnetic moment is (mostly) quenched, i.e. the expectation value of the angular momentum operator  $\langle L_z \rangle$  equals zero. The magnetic mo-

ment is dominated by the spin moment and decreases to the well-known value of  $1.73\mu_B/\text{atom}$  for hexagonal Cobalt [10]. In Fig. 1.3 one may follow this development according to the above description. While paramagnetic impurities, on the one hand, and itinerant ferromagnetism in the bulk, on the other, are well-studied by experiments there exists only little work bridging in-between. In a pioneer work M. Albrecht *et al.*, for example, discussed the moments of Fe on rough W(110) from 1D to 3D and reported a strong enhancement of the magnetic moments due to the reduced symmetry at step sites in agreement with theoretical predictions [16]. Contrary to experiments many theoretical studies revealed increased surface moments compared to the bulk value, see Tables 4.1 and 4.2.

This lack of experimental work occurs because chains (1D) and surfaces (2D) were experimentally inaccessible for a long time. There exist pioneering experimental works in the field of quantitatively studied surface magnetism of Ni(111)/Re(0001) [17] and Fe(110)/W(110) [16, 18] measured with torsion oscillating magnetometry (TOM). The spin-polarized low-energy electron diffraction (SPLEED) was used to determine surface magnetic moments for Ni [19, 20] and Fe [21]. However, later on it was doubted that this method can provide such values without ambiguity [22]. The above works are consistent in reporting enhanced surface moments with respect to the bulk value. This was more pronounced for Fe (39(16)% [18]) than for Ni (5(5)% [19, 20]).

The case of 1-dimensional chains is still an open field. It is possible to fabricate quasi-1D stripes of ferromagnetic materials by growing it on a miscutted single crystal at coverages of about half a monolayer (ML). This was demonstrated for Fe grown on a vicinal Cu (111) surface [23]. The Fe stripes of 1 – 2 atoms height and 5 – 15 atoms width were produced by step-edge decoration and showed clear ferromagnetic behavior although having a quasi-1D appearance. “Dipolar superferromagnetism” was found in Fe(110) monolayer nanostripes on a vicinal W(110) substrate [24] while “dipolar antiferromagnetism” was observed in the same system with the thickness of the stripes increased to two layers [25]. However, up to now these stripes have not been investigated by quantitative magnetometry.

Contrary to theory, the experimentalists have not the opportunity to investigate ideal systems like free surfaces, free standing monolayers, and chains. Studying surface magnetism on ultrathin films, an additional effect has to be considered: A surface of a bulk crystal is quite different from an ultrathin film on a substrate which is usually strained due to pseudomorphical growth. Theoretical calculations demonstrate this effect: the surface magnetic moment of fcc Co(001) is predicted to be  $1.85\mu_B/\text{atom}$  [26] or, by other authors  $1.948\mu_B/\text{atom}$  [27] whereas the ML Co on Cu(001) should have  $2.111\mu_B/\text{atom}$  [27] or – again by other authors –  $2.35\mu_B/\text{atom}$  [28]. Experimental results should only be compared to theoretical values which take into account the strain of the film.

In this work a complete study of the magnetic moments of Co ultrathin films grown on Cu(001) will be presented revealing the surface and the interface con-

tributions to the total magnetic moment of the film separately as well as the deconvolution of spin and orbital contributions.

### 1.3 $T_C(d)$ and $M(T)$ at low temperatures

The magnetization  $M$  of a ferromagnet is a temperature dependent quantity which vanishes at  $T_C$ . To compare experimental values of  $M$  with theoretical calculations of  $\mu$  the measured magnetization has to be translated into the magnetic moment. This is to extrapolate the magnetization to  $T \rightarrow 0$  K to have the ground-state magnetic properties ( $M_0$ ) of the system. The thermodynamically relevant temperature of the system is the reduced temperature  $t = T/T_C$ . If  $t$  is close to zero one approximately measures  $M_0$  which can be related to the magnetic moment per atom. For bulk Co the Curie temperature is about 1390 K (see Table 1.1). Consequently, experimental values for Co for  $M$  at 300 K (1447 kA/m) and at 4 K (1475 kA/m) differ by only 2% [10].

In the case of ultrathin films the situation is different. With decreasing film thickness  $T_C$  equals no longer the bulk value but decreases. This is the so-called finite-size effect [29, 30]. The dependence of  $T_C$  on the film thickness  $d$  can be described by a scaling law with a critical exponent  $\nu$  [29]:

$$\frac{T_C(d)}{T_C(\text{bulk})} = 1 - C \cdot d^{1/\nu} \quad (1.8)$$

where  $C$  is a constant. For ultrathin Co films  $T_C(d)$  is shown in Fig. 4.2 reflecting the finite-size effect:  $T_C$  approaches room temperature at thicknesses around 1.8 ML. Obviously, it is crucial to perform magnetic measurements at low temperatures if ultrathin films are studied. At least the magnetic properties, like magnetization and anisotropy, of films with different thicknesses should be compared at the same *reduced* temperature. This implies the knowledge of  $T_C$  of each film.

The low-temperature behavior of the magnetization  $M(T \rightarrow 0)$  of bulk ferromagnetic materials can be described by the well known  $T^{3/2}$  Bloch-law [9]. This is valid if the temperature dependence of  $M$  is governed by spin-wave excitations. By conversion electron Mössbauer spectroscopy it has been shown experimentally that this law is a good approximation down to the monolayer, at least for the case of Fe/W(110) [31]. For isotropic ultrathin (2D) films there exists standard spin-wave theories which suggest a linear dependence of  $M$  with respect to  $T$  [32]. A more recent theoretical work derives that for 2D ultrathin films with anisotropy the temperature dependence of  $M$  is overestimated by the linear dependence and underestimated by the Bloch-law [33]. The authors suggest a dependence of  $M$  with  $T \ln T$  and they provide a criterion for the crossover from bulk-like  $T^{3/2}$  behavior to 2D ultrathin films [33]: The separation of the low-lying spin-wave branches must be small compared to  $k_B T$  which yields a crossover to 2D behavior

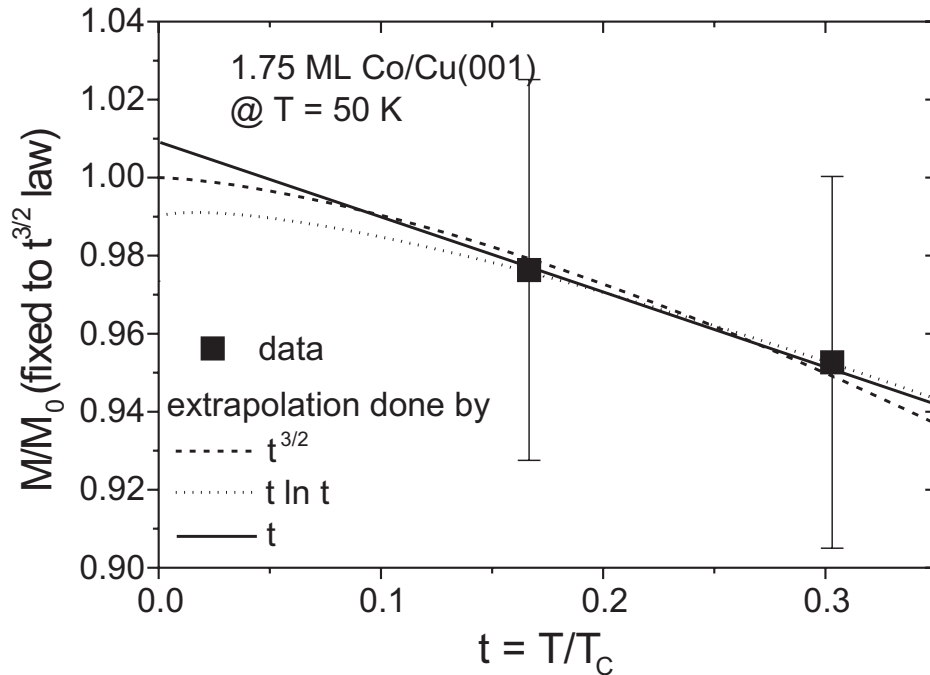


**Figure 1.4:** Reduced magnetization ( $M/M_0$ ) vs reduced temperature  $t$  including a measurement at low temperatures. All three methods of extrapolating to  $T = 0$  K had been fitted to the data (only the low-temperature data are shown here). (i), (ii), and (iii) are almost indistinguishable which demonstrates that measuring at  $t \leq 0.2$  permits precise determination of  $M(T = 0)$  values independent of the chosen model.

at thicknesses around 2 to 3 ML. The non-validity of the spin-wave law for these films can be understood in the following way: Due to dipolar interactions of spin waves in two-dimensional films the dispersion of the spin waves is negative at low temperatures [33].

To derive values for  $M$  at  $T = 0$  K one has to extrapolate the measured data to  $T = 0$  K. If the lowest accessible reduced temperature is close to zero the resulting extrapolated value of  $M_0$  is insensitive to the chosen model. This is illustrated in Fig. 1.4. Two low-temperature data of a measurement taken from Fig. 4.11 are shown in reduced units. The reduced magnetization is taken with respect to the  $M_0$  value derived by the spin-wave law (dashed line) since the agreement of this model is best for the data with  $t \geq 0.4$ . It is obvious that also the  $t \ln t$  law (dotted line) and the linear behavior (full line) lead to almost the same value for  $M_0$  if only the measurements at  $t \leq 0.4$  are taken into account. At  $t \geq 0.4$  both models clearly deviate. Consequently, by measuring at reduced temperatures  $t \leq 0.2$ , uncertainties due to the extrapolation are obviated — no matter which exact functional behavior is assumed to be the correct one. The additional errorbar is at most 1-2% and small compared to the one originating

from the measurement ( $\sim 5\%$ ) indicated in Fig. 1.4.

## 1.4 Contributions to the total magnetic moment

In a non-relativistic theory for free atoms or ions in a solid the magnetic moment  $\mu$  consists of two contributions. The one is the orbital moment  $\mu_L$  originating from the motion of the electrons. The other is the spin moment  $\mu_S$  which is an intrinsic property of the electrons. Both contributions are described by the quantum numbers  $L$  and  $S$ . The fact that  $L$  is a good quantum number is due to the rotational invariance of the system while  $S$  is a good quantum number only if spin dependent interactions are neglected ([11], p. 587). Then  $L$  and  $S$  couple to  $J = L + S$  which is termed Russel-Saunders-type of coupling. The total moment is given by the sum of spin and orbital moment, and the Landé-factor is given by eq. (1.7). However, the calculation of the Landé-factor using eq. (1.7) becomes more or less incorrect if the spin dependent interactions are not negligible compared to the orbital forces [11].

If the magnetic properties of a ferromagnetic solid are discussed in terms of spin and orbital moments it is assumed that  $L$  and  $S$  are – to some extent – good quantum numbers, i.e. their expectation value is observable. As stated above, the presence of spin dependent forces makes this approximation somewhat incorrect. However, the localized ionic picture is applied to solids in literature as well, e.g. in the framework of x-ray magnetic circular dichroism. The discussion of magnetism with respect to spin and orbital contribution is motivated by the following: The orbital moment is the microscopic origin of anisotropy since it couples the moment to the lattice via the spin-orbit coupling. For example, a recent theoretical approach by Bruno suggests that the magnetic anisotropy is proportional to the orbital moment anisotropy and the spin-orbit coupling constant [34]. Moreover the origin of enhanced magnetic moments at surfaces can be elucidated since the magnetic moment in a solid is dominated by the spin while the orbital contribution is mostly quenched due to the high symmetry of the surrounding atoms, see e.g. [11]. An enhanced surface moment can be attributed to the reduced symmetry and therefore to significant unquenching of the orbital moment if  $\mu_L$  is enhanced. These examples may demonstrate that it is useful to discuss magnetism in a solid in terms of spin and orbital moment. In any case, it is insufficient to regard magnetism as a phenomenon which is solely caused by the spins of the material.

Most of the classical magnetometries measure the *total* magnetization  $M$  or magnetic moment  $\mu$ . Few techniques are in a position to separate the contributing parts. One possibility is to measure the total magnetic moment with a classical magnetometry and combine the results with gyromagnetic measurements of the Landé factor  $g$  (e.g. Einstein-de Haas effect, see e.g. Chikazumi's book [35])

applying Kittel's formula [36]:

$$\frac{\mu_L}{\mu_S} = \frac{g - 2}{2} \quad (1.9)$$

Measurements of anisotropic  $g$  values using ferromagnetic resonance yield anisotropic orbital moments by applying eq. (1.9) [37]. Using polarized neutron diffraction (PND) a form factor analysis can provide separate values for  $\mu_L$  and  $\mu_S$  [38, 39]. In the case of x-ray magnetic circular dichroism (XMCD) the sum rules [40, 41] enable the determination of  $\langle S_z \rangle$ , and  $\langle L_z \rangle$  (and  $\langle T_z \rangle$ , the so-called magnetic dipole vector).

In the following the separation of spin and orbital contributions to the magnetic moment is briefly sketched within the framework of PND and XMCD, especially discussing the role of the  $\langle T_z \rangle$  term. This becomes of relevance upon comparing the findings of XMCD with classical magnetometric measurements. Since both, XMCD and PND, use a localized ionic picture within the analysis, the electron paramagnetic resonance (EPR) will be discussed first. This is done with respect to spin-dependent interactions because they are responsible for deviations from the ideal case of pure  $L$  and  $S$  states.

### 1.4.1 Spin dependent interactions in EPR

The most important spin dependent interaction is the spin-orbit coupling (SOC). The SOC is the microscopic origin of anisotropy since it couples the spin to the lattice. The Hamiltonian is of the form  $H_{SOC} \sim \lambda \mathbf{L} \cdot \mathbf{S}$ . Since the shape of the

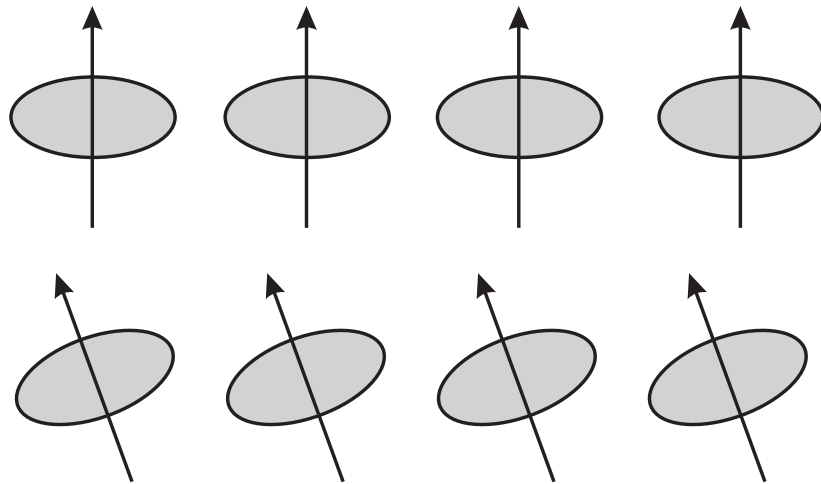


**Figure 1.5:** Two interacting charge clouds (light gray) whose shapes are depending on the spin direction via the SOC. Arrows represent the spin direction [42].

electronic clouds is linked to the orbital moment the SOC couples the clouds to the spin direction ([42], p. 158). This gives rise to an interaction which depends on the spin direction due to the quadrupolar moment (and higher orders) of the electronic charge distributions. This is illustrated in Fig. 1.5. The quadrupolar moment of the electronic charge distribution is given by ([11], p. 627)

$$Q_{ij} = \sum_p \left( 3x_i^p x_j^p - (r^p) \delta_{ij} \right) \quad (1.10)$$

where  $x_i^p$  are the coordinates of the electrons of an atom. An interaction which depends on the spin direction is often called *anisotropic* exchange. This anisotropy is not due to the direct exchange between the spins which is certainly *isotropic* and of the form  $H \sim (\mathbf{S}_i \cdot \mathbf{S}_j)$ . The anisotropic contribution to the spin-spin interaction is due to a second order perturbation treatment of the SOC if the electronic charge distribution is of lower than spherical symmetry [42]. It is of the form  $H \sim (\mathbf{S}_i J_{ij} \mathbf{S}_j)$  where  $J_{ij}$  in its explicit form describes the type of interaction.

Another relevant spin-dependent interaction is the magnetic dipole coupling between two moments  $\mu_i$  and  $\mu_j$  ([11], p. 53), see Fig. 1.6. A magnetic dipole  $\mu_j$  at a distance  $r$  gives rise to a local field  $(H_{loc})_j$  at site  $i$ :

$$(\mathbf{H}_{loc})_j = \frac{\mu_0}{4\pi} \sum_j \frac{\mu_j - 3\mathbf{r}_j(\mathbf{r}_j \cdot \mu_j)}{r_j^3} \quad (1.11)$$

This interaction is of magnetostatic character and depends on the explicit spatial

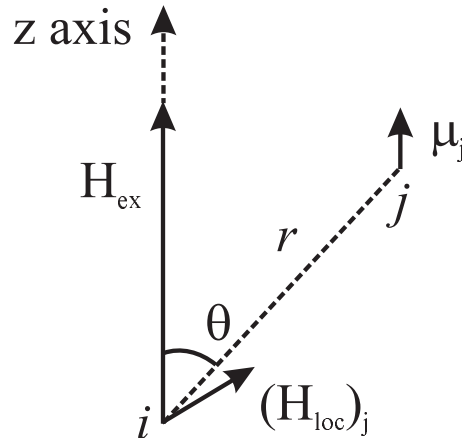


**Figure 1.6:** The local field  $H_{loc}$  set up at site  $i$  by the magnetic dipole  $\mu$  at site  $j$ . The z-component of  $H_{loc}$  varies like  $(3\cos^2\theta - 1)$  if the paramagnetic properties of  $j$  are isotropic. A strong external field along the  $z$  axis is assumed [11].

arrangement of the spins. The local field acts on the magnetic moment at site  $i$

and leads to a slight change in the direction of the spin ([42], p. 198), see also ([43], pp. 1072).

All spin dependent interactions give rise to a small anisotropic contribution of the interaction of two spins although the exchange interaction itself is isotropic. In classical EPR literature this is often discussed in terms of *effective* spins or *anisotropic*  $g$ -factors [11].

### 1.4.2 Formfactors and current densities in PND

The well-known value for the magnetic moment of hexagonal Co is between 1.71 and  $1.73\mu_B/\text{atom}$  [10]. The separation into spin and orbital contributions is based on an old measurement using PND [38]. In that work, the magnetic moment

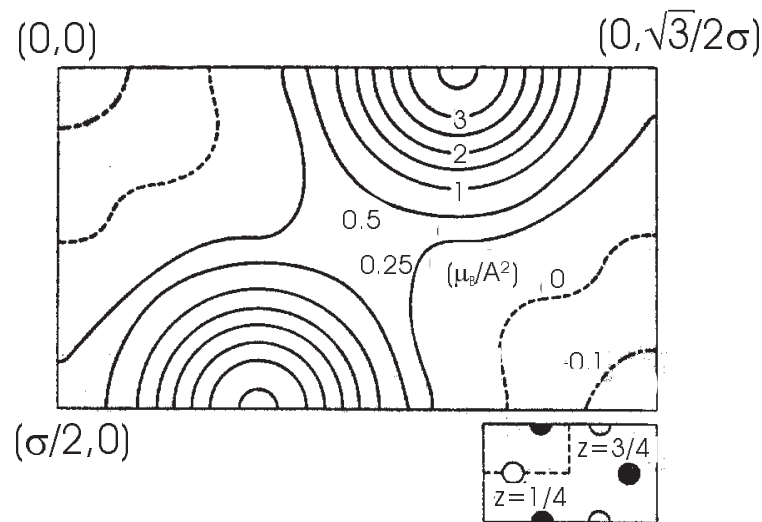


**Figure 1.7:** Projection of magnetic moment density on the basal plane for hexagonal cobalt. Lower right diagram shows the projected positions of atoms in the orthorhombic unit cell. Dashed lines indicate portion of cell shown in the density map [38].

density on the basal plane is given with the help of a Fourier projection (see Fig. 1.7). It can clearly be seen, that the major part of the spin density is located near the nucleus and that the interstitial space is negatively polarized. Although having an itinerant  $3d$  ferromagnet the moment density is mostly located at one atomic site. This may encourage the use of the localized ionic picture to describe band-ferromagnets in a first approximation, keeping in mind that there is some (smaller) amount of delocalized moment density in the interstitial space.

Following [38] a form factor analysis of the scattering amplitude provides the separation into spin and orbital contributions but a small deviation from

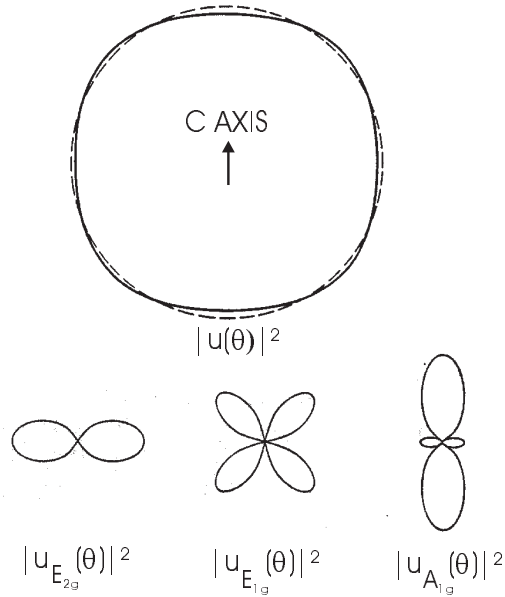


**Figure 1.8:** Angular dependence of the spin density in hexagonal cobalt [38]. Dashed circle is for spherical symmetry corresponding to  $|u(\theta)|^2 = 0.4|u(E_{2g})|^2 + 0.4|u(E_{1g})|^2 + 0.2|u(A_{1g})|^2$ . The solid figure sketches the aspherical distribution from the form factor analysis yielding  $|u(\theta)|^2 = 0.394|u(E_{2g})|^2 + 0.416|u(E_{1g})|^2 + 0.190|u(A_{1g})|^2$ .

the spherical symmetry must be considered to reproduce the measurements adequately. This is caused by a crystalline-field splitting of the  $3d$  electrons into three sub-states, two doubly degenerated levels with rotational properties like  $xy$ ,  $x^2 - y^2$  and  $yz$ ,  $xz$  and a single level like  $3z^2 - r^2$ . This can be visualized by plotting the  $\theta$  dependence of the squared angular part of the wave function for these substates as illustrated in Fig. 1.8. The spin density along the  $c$  axis (easy axis of magnetization) is reduced by about 6%. The different substates are sketched as well. The analysis in [38] suggests that the crystalline-field distorts the  $3d$  electronic cloud leading to a small non-spherical contribution to the spin density. The spin distribution according to Fig. 1.8 can be modeled by a sum of two parts: an atomic  $3d$  density function located at each atomic site and a negative constant. The contributions to the total magnetic moment are splitted into three parts [38]: (i) a spherical  $3d$  spin ( $1.86(7)\mu_B/\text{atom}$ ), (ii) a constant negative spin ( $-0.28(7)\mu_B/\text{atom}$ ) and (iii) a  $3d$  orbital one ( $0.13(1)\mu_B/\text{atom}$ ). The total magnetic moment is given by the sum of (i), (ii) and (iii).

In [39] the current density picture of the magnetic scattering of neutrons is used to discuss the reliability of the separation of spin and orbital contributions within a formfactor analysis.

The magnetic scattering of neutrons can be formulated in terms of current

densities  $\mathbf{j}(\mathbf{r})$  to deduce the magnetic moment  $\mu$ :

$$\int_V \mathbf{M}(\mathbf{r})dV = \frac{1}{2} \int \mathbf{r} \times \mathbf{j}(\mathbf{r})dV = \mu \quad (1.12)$$

It should be noted that the total magnetic moment is simply derived by extrapolating the measured formfactors to  $q = 0$  ( $q$  denotes the scattering vector) which is exact [39]. The separation of spin and orbital contributions can be achieved by splitting  $\mathbf{j}(\mathbf{r})$  into spin ( $\boldsymbol{\sigma}(\mathbf{r})$ ) and orbital ( $\mathbf{j}^0(\mathbf{r})$ ) contributions represented by an expansion with respect to the vector spherical harmonics  $\mathbf{Y}_{\mathcal{L},\mathcal{M}}^{\mathcal{L}}$  [39]. Calculating the expectation value of the current density in eigenstates of the  $z$  component of the total magnetic moment,  $\mathcal{M}$  will vanish ( $\mathcal{M} = 0$ ). The remaining contributions to  $\mu$  are only the dipolar components of the current densities, i.e. terms with  $\mathcal{L} = 1$  [39].

The separation of spin and orbital contribution is then linked to the Racah double tensors  $W_0^{(0,1)1}$ ,  $W_0^{(1,0)1}$ , and  $W_0^{(1,2)1}$ . This is based on the fact that they, on the one hand, appear in the dipole component of the scattering amplitude, and, on the other hand, are related to the operators of the angular momentum [39]:

$$\boldsymbol{\sigma}(\mathbf{r}) \sim W_m^{(1,0)1} = \left(\frac{2}{2l+1}\right)^{1/2} S_m \quad (1.13)$$

$$\mathbf{j}^0(\mathbf{r}) \sim W_m^{(0,1)1} = \left(\frac{3}{2l(l+1)(2l+1)}\right)^{1/2} L_m \quad (1.14)$$

The operator  $W_0^{(1,2)1}$  is not related to  $S_m$  or  $L_m$  in a simple way which complicates separation of  $\mu_L$  and  $\mu_S$  since it contributes to  $\boldsymbol{\sigma}(\mathbf{r})$  as well. Unless this term is neglected in the usual dipole approximation, it must be taken into account within the *proper* dipole approximation to determine the ratio of  $\mu_L$  and  $\mu_S$  [39].

$W_0^{(1,2)1}$  stands for a dipolar contribution involving the second order Bessel component in the multipole expansion of the spin current density. An operator equivalent constructed from spin and position vectors of  $W^{(1,2)1}$  is the so-called dipolar vector  $\mathbf{T}$  and in cartesian coordinates the components are given by [39]:

$$T_\alpha = \sum_\beta Q_{\alpha\beta} S_\beta \quad (1.15)$$

where  $Q_{\alpha\beta}$  is the quadrupole tensor of the charge distribution comparable to eq. (1.10):

$$Q_{\alpha\beta} = \delta_{\alpha\beta} - 3r_\alpha r_\beta / r^2 \quad (1.16)$$

The operator  $\mathbf{T}$  represents the coupling of the quadrupole moment of the charge distribution to the spin moment [39] which is illustrated in Fig. 1.5. As a matter of fact another operator equivalent of  $W^{(1,2)1}$  reflects the emergence of the SOC see [39] and ([11], p. 692). It should be noted that  $\mathbf{T}$  is a vector involved in a *dipole* approximation.

### 1.4.3 The XMCD sum rules

Unlike the PND the x-ray magnetic circular dichroism (XMCD, x-ray near edge absorption spectroscopy with circularly polarized light) is not in a position to provide values for the total magnetic moment  $\mu_{tot}$ . The separate values of spin and orbital magnetic moment are derived by applying the so-called XMCD sum rules which imply various approximations [40, 41, 44]:

- An atomistic picture is used (only intra-atomic hybridization of the wave functions is taken into account).
- Only  $d$ -states are taken into account.
- The core hole is not screened (“sudden approximation”).
- The radial part of the matrix elements is assumed to be energy-independent.

The uncertainty of these approximations is assumed to be between 5 and 30% depending on the measured system [41, 45]. However, for thick Fe and Co films the validity of the sum rules has been confirmed experimentally [46]. The sum rule for the orbital moment was derived first from Thole *et al.* [40]:

$$\langle L_z \rangle = \frac{2}{3} \frac{n_H}{P_c \cdot \cos \theta} \cdot \frac{\int_{L_3} (I^+ - I^-) d\omega + \int_{L_2} (I^+ - I^-) d\omega}{\int_{L_3+L_2} (I^+ + I^-) d\omega} \quad (1.17)$$

where  $I^+$  and  $I^-$  denote the absorption spectra with the photon helicity vector parallel (+) and antiparallel (−) to the magnetization. The contribution of the  $sp$ -states has to be subtracted from the spectra before the integration. Besides the spectral intensities, the number of  $d$ -holes  $n_H$ , and the degree of polarization of the synchrotron radiation  $P_c$  enter the moment determination as parameters. They can be derived either by optical considerations ( $P_c$ ) and calculations ( $n_H$ ) or by using a bulk specimen as a reference sample [47, 48]. The  $3d$  orbital magnetic moment is given by:

$$\mu_L = -\langle L_z \rangle \cdot \mu_B \quad (1.18)$$

The sum rule for the spin moment includes an additional term, namely the magnetic dipole operator  $\langle T_z \rangle$ :

$$\langle T_z \rangle = \sum_i \mathbf{s}_i - \frac{3\mathbf{r}_i(\mathbf{r}_i \cdot \mathbf{s}_i)}{r_i^2} \quad (1.19)$$

This term provides a measure of the anisotropy of the field of the spins when the atomic cloud is distorted, either by the spin-orbit interaction or by crystal field effects [41]. Therefore, it is a measure for the non-sphericity of the spin density

(discrepancy between solid and dashed line in Fig. 1.8). The sum rule for the spin moment is [41]:

$$\langle S_z \rangle + \frac{7}{2} \langle T_z \rangle = \frac{1}{2} \frac{n_H}{P_c \cdot \cos \theta} \cdot \frac{\int_{L_3} (I^+ - I^-) d\omega - 2 \int_{L_2} (I^+ - I^-) d\omega}{\int_{L_3+L_2} (I^+ + I^-) d\omega} \quad (1.20)$$

In the cubic phase of Fe, Co, and Ni the  $\langle T_z \rangle$  term is assumed to be negligibly small ( $< 10\%$ ) [41]. Then, the  $3d$  spin moment can be derived from the spectral intensities and the calibrating parameters  $n_H$  and  $P_c$ :

$$\mu_S = -2 \cdot \langle S_z \rangle \cdot \mu_B \quad (1.21)$$

If this is the case the total moment is the sum of  $\mu_S$  and  $\mu_L$ .

The determination of the ratio of  $\mu_L/\mu_S$  is safer since the calibrating parameters  $n_H$  and  $P_c$  cancel out each other by dividing eq. (1.17) by eq. (1.20). This yields:

$$\frac{\mu_L}{\mu_S} = \frac{\langle L_z \rangle}{2 \langle S_z \rangle + 7 \langle T_z \rangle} = \frac{2 \int_{L_3} (I^+ - I^-) d\omega + \int_{L_2} (I^+ - I^-) d\omega}{3 \int_{L_3} (I^+ - I^-) d\omega - 2 \int_{L_2} (I^+ - I^-) d\omega} \quad (1.22)$$

The derived ratio can be compared with gyromagnetic measurements using eq. (1.9). For bulk-like Co and Fe a good agreement is reported [46].

In case of a non-negligible  $\langle T_z \rangle$  contribution the spectral intensities provide only a measure of an effective spin moment  $\langle S_z \rangle_{eff} = \langle S_z \rangle + 7/2 \langle T_z \rangle$ . The  $\langle T_z \rangle$  term becomes important in case of non-cubic symmetry, e.g. at surfaces. For Co films sandwiched between Au(111) angular dependent measurements using XMCD determined the  $\langle T_z \rangle$  value independently [49]. The contribution of  $\langle T_z \rangle$  is found to be antiparallel to the spin moment and increases with decreasing film thickness. This is confirmed by theoretical calculations which predict a  $\langle T_z \rangle$  contribution of  $-0.014$  for the central layers of hcp Co while it is enhanced to  $-0.24$  at the surface [28].

A more general discussion of the nature of the  $\langle T_z \rangle$  term can be found e.g. in [50]. The magnetic dipole vector  $\mathbf{T}$  is the tensor product of the quadrupole moment  $Q_{\alpha\beta}$  of the charge distribution with the spin  $\mathbf{S}$  as given by eq. (1.15). There exists a formal relationship between the *intraatomic* magnetic dipole operator, see eq. (1.19), and the *interatomic* dipole field, see eq. (1.11). The latter describes the field at a given atomic site generated by all other magnetic dipoles at position  $r_j$  in the sample and was discussed above, see Fig. 1.6. The *intraatomic* dipole interaction contributes to the magnetic anisotropy in higher order through a quadrupole term [50].

It should be noted that the *intraatomic* dipole or  $\langle T_z \rangle$  term of XMCD represents the same phenomenon that is described by the  $W_0^{(1,2)1}$  operator within the current density picture for the neutron scattering. The fact that there is a non-spherical contribution to the spin density distribution which gives rise to a finite value of  $\langle T_z \rangle$  was already measured in [38] and is illustrated in Fig. 1.8.

### 1.4.4 The role of the $\langle T_z \rangle$ term

The UHV-SQUID magnetometer presented in this work measures the total magnetization  $M$  of a sample, or, after extrapolating to  $T = 0$  K, the real ground-state total magnetic moment  $\mu_{tot}$ . This quantity can be compared to the findings of measurements using PND, vibrating sample magnetometer, or torsion oscillation magnetometer. Comparing with results derived by a sum rule analysis, this requires the knowledge if the  $\langle T_z \rangle$  term contributes to the total magnetic moment. In most cases this question needs not to be answered since the  $\langle T_z \rangle$  term is negligible in most of the experiments which have been done so far. Only by now it is possible to compare the ground-state magnetic properties of ultrathin films measured with a classical magnetometry to XMCD data. At the ultrathin film limit the low symmetry at the surface gives rise to sizable quantities of  $\langle T_z \rangle$  (0.24 for the Co surface) [28, 50], however, it is a small effect ( $\sim 5\%$ ). Three different cases for the role of the  $\langle T_z \rangle$  term will be discussed in the following sketching a physical picture and discussing the consequences for the comparison between SQUID and XMCD.

(i) The most simple assumption is that  $\mu_{tot} = \mu_S + \mu_L$ , which is straightforward and common sense. Then the comparison between XMCD and UHV-SQUID data would enable to determine  $\langle T_z \rangle$  without performing angular-dependent XMCD measurements. This occurs because there are three variables ( $\langle L_z \rangle$ ,  $\langle S_z \rangle$ , and  $\langle T_z \rangle$ ) and three equations linking the variables to a measurable quantity (two sum rules and  $\mu_{tot}$  of the SQUID). The outcome of such an analysis is given in Section 4.3.3.

(ii) Contrary to that, the formal relationship between the *intraatomic* magnetic dipole operator, see eq. (1.19), and the *interatomic* dipole field, see eq. (1.11) may suggest that the influence of a non-vanishing  $\mathbf{T}$  may be similar to the effect sketched in Figs. 1.5 and 1.6. This is, that a single spin is canted by the field generated by all other spins within one atomic sphere. Such a behavior is sketched in Fig. 1.9 and the (somewhat simple) picture may trigger some theoretical work to offer an answer on more solid grounds. Following this,  $\mathbf{T}$  is supposed to describe a small change in the direction of the spin  $\mathbf{S}$  due to the quadrupolar moment  $Q_{\alpha\beta}$  of the charge distribution.  $\mathbf{S}$  represents the spin direction when no interaction due to the quadrupolar moment of the charge distribution is taken into account.  $\mathbf{T}$  describes a small change in the direction of  $\mathbf{S}$  resulting in an effective spin  $\mathbf{S}_{eff}$  due to the SOC. Therefore the projection of  $\mathbf{S}$  on the quantization axis changes by the projection of  $\mathbf{T}$ . This may illustrate why the contribution of the  $\langle T_z \rangle$  term along the quantization axis may be measurable with a classical magnetometer as well. To verify this it has to be shown, that the above-mentioned analogy between the operator  $\mathbf{T}$  and the local field  $H_{loc}$  holds indeed.

(iii) Another approach to understand the role of the  $\langle T_z \rangle$  term is based on the discussion of the sum rules in [50]. In that work it is reported that the spin moment of an ultrathin Co film is smaller in the film plane ( $\mu_S^{\parallel}$ ) than out-of-

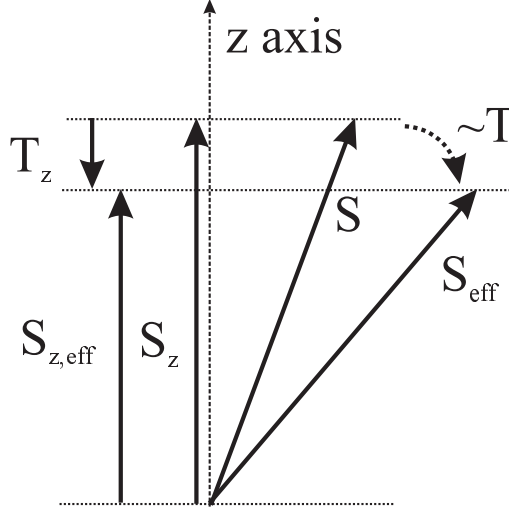


**Figure 1.9:** Suggested picture for the influence of  $\mathbf{T}$ . The quadrupolar moment of the charge distribution rotates the spin  $\mathbf{S}$  by a small angle. The  $\langle T_z \rangle$  term then provides a measure for the change in the projection  $S_z$  of the spin  $\mathbf{S}$  on the quantization axis ( $z$ ).

plane ( $\mu_S^\perp$ ). The total isotropic spin is given by  $\mu_S = 2\mu_S^\parallel + 3\mu_S^\perp$ . Hereby the  $d$ -projected spin magnetic moments are summed up, e.g.  $\mu_S^\perp = \mu_S^{xz} = \mu_S^{yz} = \mu_S^{3z^2-r^2}$ . XMCD offers the possibility to probe the spin density distribution within the unit cell by angular dependent measurements under a strong external field for complete saturation of the sample. In each direction the *intraatomic* dipole term contributes to the measurement as well:  $\mu_D^\alpha = (7/2) \sum^i Q_\alpha^i \mu_S^i$  ( $\alpha$  denotes the three different directions  $x, y, z$ ). In the angle averaged measurement  $\mu_D^\alpha$  cancels out:  $1/3 \sum_\alpha \mu_D^\alpha = 0$ . Following this, a measurement using XMCD in only one direction without external field measures not the total isotropic spin but only a reduced spin moment (e.g.  $\mu_S^\parallel$ ) plus the respective  $\mu_D^\parallel$  contribution along the measuring direction. In that case the missing contribution from the spin density and the additionally  $\mu_D^\alpha$  “moment” cancel out each other since the  $\mu_D$  reflects the asphericity of the spins yielding the total isotropic spin. Therefore the total magnetic moment  $\mu_{tot}$  would equal  $\mu_S$  and  $\mu_L$ . However, XMCD spectra taken in remanence along one single direction do not measure  $\mu_S$  but only  $\mu_S^\parallel$  (if the easy axis is in-plane) plus  $\mu_D^\parallel$ . To clarify this, a theoretical sound analysis of the sum rules for the remanent state has to be performed. Unfortunately, [50] generally assumes a strong external field within the entire discussion.

From the experimental point of view it is almost impossible to distinguish between (i), (ii), and (iii). This would require magnetometry with high accuracy ( $\leq 5\%$ ) and sensitivity to measure magnetic films with a thickness of few atomic layers only. XMCD measurements and the UHV-SQUID magnetometer presented in this work offer sufficient sensitivity. Unfortunately, this is not true concerning

the accuracy. The SQUID offers about 5%, however, the derivation of the sum rules causes an uncertainty of at least 5 to 10%, see above. Nevertheless, some experimental findings are discussed in Section 4.3.3 which are not significant due to the finite experimental accuracy.

In summary, it is not trivial or straightforward to relate the total magnetic moment with the quantities  $\langle S_z \rangle$ ,  $\langle L_z \rangle$ , and  $\langle T_z \rangle$ , especially if the XMCD measurements are not performed angular-dependent. Therefore, a direct proof of the validity of a sum rule analysis for ultrathin films (where  $\langle T_z \rangle$  reaches sizable quantities) is complicated. It is not the aim of the above discussion to give an explicit answer but just to rise some questions concerning the role of the  $\mathbf{T}$  operator and - perhaps - to trigger some work to offer a physical description on more solid grounds. Consequently, the comparison between XMCD and UVH-SQUID in Section 4.3.3 refers to both possibilities, (i) and (ii) ((iii) has the same consequences as (ii)). The whole section may demonstrate that a disentanglement of the contributions to the magnetic moment enlightens the explicit mechanisms behind ferromagnetism within a local picture. This should not deny the merits of describing ferromagnetism in terms of energy-bands.

# Chapter 2

## Different types of magnetometry

This Chapter gives a brief overview of different types of magnetometry to demonstrate the abilities of the novel UHV-SQUID magnetometer compared to well-established techniques. Therefore, this discussion is restricted to magnetometries applicable *in situ* in UHV. Some of the methods are widely used (MOKE and XMCD) while others are only applied by few experimental groups. The comparison concerns mainly the sensitivity, the accessible temperature range, the calibration, and the experimental restrictions, e.g. suitable substrates.

### 2.1 Magneto-optical Kerr effect (MOKE)

The systematic investigation of magnetism using electro-magnetic radiation started more than 150 years ago with the discovery of the Faraday effect [51]. The polarization vector of linearly polarized light was found to rotate while traveling through ferromagnetic materials. The same behavior was observed for the reflected light by Kerr about 30 years later [52]. MOKE is widely used to study magnetism, see e.g. [53]. It is one of the standard methods to investigate all kinds of ferromagnetic materials. Since it is linked to interband-transitions within the valence band the effect depends also on the frequency of the light (MOKE-spectroscopy). There exists a second order Kerr-effect as well, i.e. reflected light with the doubled frequency of the incident light. This so-called second harmonic generation (SHG) is sensitive only to the layers with broken symmetry, e.g. surfaces [54].

The MOKE works under external fields and therefore it permits recording hysteresis loops. The sensitivity limit is about 1 to 2 ML of Co (in-plane geometry, the so-called longitudinal MOKE) using a standard HeNe laser. If the films are magnetized perpendicular to the film plane (polar MOKE) the sensitivity is about a factor of 10 higher. The absolute value of the rotation of the light is proportional to the magnetization of the sample. It depends on the optical constants of the studied material and must be calibrated for each material sep-

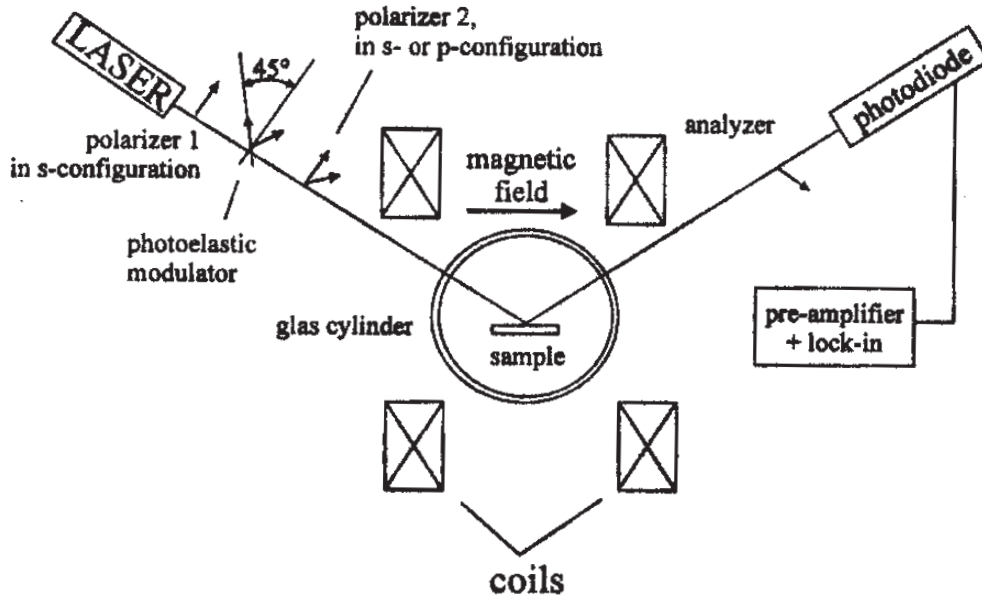


**Figure 2.1:** Principle setup of an *in situ* MOKE magnetometer. The sample can be kept under UHV while the setup with polarizer and laser may be outside the vacuum chamber. The light can be sent through a glass window (which should show minimum Faraday effect).

arately. This can be done with respect to a bulk specimen, e.g. [55]. In that sense it should be termed as a *relative* magnetometry. However, the application of MOKE mostly provides results for the magnetization in arbitrary units (“Kerr rotation”) whereas the anisotropy, the coercive field, and the Curie temperature can be determined directly. The latter is often measured with a modulation technique, the ac-MOKE which measures the susceptibility  $\chi$ . This implies that the signal is measured as a function of temperature. There are no principle limitations concerning the accessible temperature range or the samples.

## 2.2 X-ray magnetic circular dichroism (XMCD)

Extending the MOKE to the energy range of the x-rays Erskine and Stern predicted the XMCD [56] which was first observed experimentally by Schütz *et al.* [57]. The XMCD method was established quite fast and is widely used within the synchrotron community [58]. Since the synchrotron radiation excites electrons from core level states, this technique is element- and site-specific. This offers the unique possibility to study the different materials in alloys or multilayers *separately*, e.g. [59].

The difference of the absorption of left and right circular polarized light pro-

vides a difference spectrum which is proportional to the magnetization. These difference signals can be detected at coverages down to 1/100 of a ML, in diluted alloys, or in microscopy. Depending on the detection mode of the absorption, application of even large (5–7 T) external fields is possible, e.g. [49, 59]. If secondary electron yield is detected the application of an external field may lead to artefacts in the recorded spectra. Therefore, only the remanence is measured in [47, 60]. Cooling and heating of the sample is not limited by the technique, so that one can measure at least down to 10 K with standard IHe cooling facilities.

Applying the sum rules [40, 41] it is possible to derive quantitative information about spin and orbital moment (and the  $\langle T_z \rangle$  term, e.g. [49]). As discussed in Section 1.4.3 two calibrating parameters are needed, i.e. the polarization of the synchrotron radiation  $P_c$  and the number of  $d$ -holes  $n_H$  to derive absolute numbers.  $P_c$  can be taken from optical considerations and theory provides numbers of  $n_H$ . This results in an *absolute* determination of the magnetic moments. However, the signals are often calibrated with the help of a bulk sample like in [47, 48]. In that sense, this method mainly provides *relative* magnetometric information. In [46] the authors derived *absolute* values for bulk-like films of Co and Fe to test the validity of the sum rules. However, especially the number of  $d$ -holes was (experimentally) found to depend on the film thickness [61] which complicates the determination of the magnetic moments at the ultrathin film limit. Some measurements on ultrathin Ni and Co films were published in [47, 62]. The accuracy of the sum rule analysis further depends on the integration of the spectral intensities and the subtraction of the  $sp$ -states in the spectra. This procedure leads to an uncertainty of at least 10% in the derived values for the magnetic moments corresponding to  $0.05\mu_B$ .

## 2.3 Polarized neutron reflection (PNR)

The investigation of ferromagnetic materials with polarized neutrons provides standard literature values, e.g. the well-known bulk value of Co in the Landolt-Börnstein [10] was taken from an old study using PNR [38]. These measurements were discussed in Section 1.4.2. Although widely used (see e.g. Table 4.3), this method was applied in UHV only recently [63].

The principle setup of the PNR magnetometer is sketched in Fig. 2.2. The main feature is a quartz cylinder to shine the neutron beam onto the sample. In principle, the *in situ* PNR is submonolayer sensitive, however, only Fe films down to 1 nm thickness were measured in [63]. The reported accuracy ( $\sim 0.05\mu_B/\text{atom}$ ) in determining the magnetic moment per atom is comparable to XMCD. This determination does not depend on the precise knowledge of the sample structure or thickness and can be done as a function of temperature since cooling with IHe down to 80 K is possible [63]<sup>1</sup>. This type of magnetometry needs only the

---

<sup>1</sup>Obviously the accessible temperature range can be optimized.

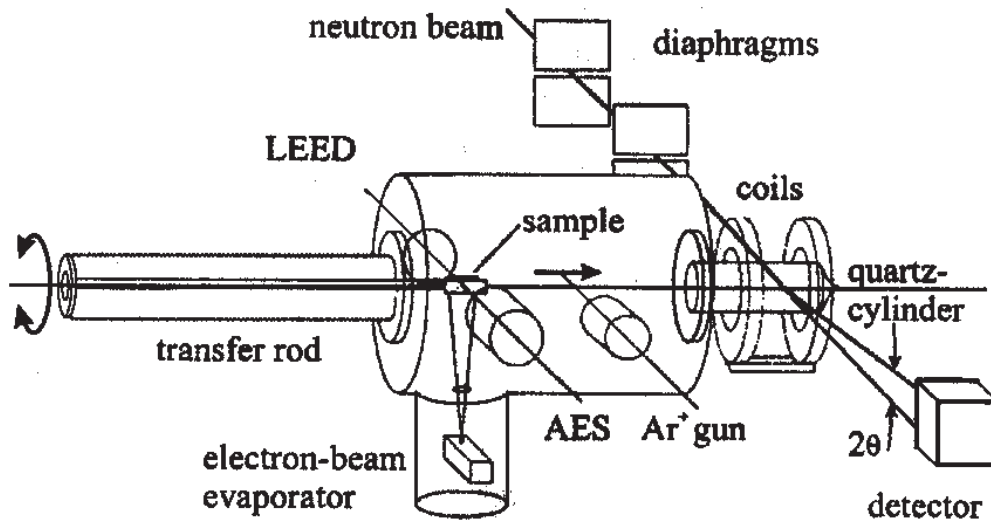


Figure 2.2: Principle setup of an *in situ* PNR magnetometer taken from [63].

degree of polarization of the neutrons as an input parameter which is assumed to be almost 100% [64]. In that sense the *in situ* PNR is an *absolute* method to measure the magnetic moment since the outcome only depends on fundamental constants like the spin of the neutron. However, up to now the setup is only able to detect the in-plane component of the magnetization. Taking advantage of the *in situ* techniques Fe films on V(110) and Cr(110) prepared under different conditions were studied with PNR [65].

## 2.4 Alternating gradient magnetometer (AGM) and cantilever magnetometers

An alternating gradient magnetometer with sensitivity of at least  $10^{-8}$  emu has been described by Flanders [66]. In principle, the torque of a ferromagnetic sample in an oscillating, inhomogeneous magnetic field is measured. The original setup is shown in Fig. 2.3. Later on a similar system was installed inside an UHV chamber [67]. This magnetometer works only at ambient temperature and does not offer heating possibility above  $180^{\circ}\text{C}$  (which hinders appropriate preparation of various substrates) since the glue used for the mounting of the cantilever can not stand higher temperatures [68]. The sensitivity is comparable to the *ex situ* setup. An external field must be applied for the measurements. In principle, an AGM allows *absolute* determination by calibrating with a current coil. However, this calibration is cross-checked with a bulk sample which is measured with an *ex situ* SQUID magnetometer as well [68].

A similar method to determine the magnetization *in situ* is based on can-

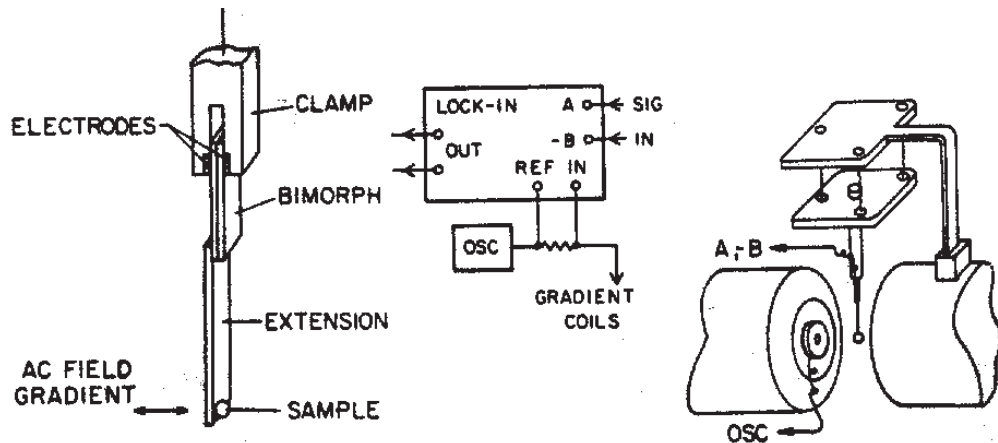


**Figure 2.3:** Principle setup of an AGM. The drawing was taken from [66].

tilt magnetometers. The torque of a ferromagnetic sample in a static external field is measured. Some setups are specialized on magnetostrictive measurements which implies that the substrate is bendable [69]. Such a setup is calibrated via the torque of a known weight to deduce absolute values. 5 ML of Fe were measured with a signal-to-noise ratio of about 5; the accuracy of the magnetization determination was 80 kA/m corresponding to  $\sim 5\%$  [69]. The measurements are restricted to 300 K. A similar setup is discussed in [70]

Another solution was recently designed for single-crystal samples [71]. This setup is restricted to ambient temperature as well. 2.5 ML of Fe/Cu(001) could be measured with a signal-to-noise ratio of about 5, the bulk magnetic moment was determined from thickness dependent measurements yielding  $2.2(1)\mu_B/\text{atom}$ . The relatively large errorbar was attributed to a background signal originating from magnetic parts of the sample holder which had to be subtracted [71].

The main limitation of the different cantilever methods is the restriction to room-temperature measurements when applied in UHV. All these magnetometries are in principle in a position to determine the magnetization of ultrathin films but they will fail as soon as the Curie temperature is close or even below room temperature. This is not due to lack of sensitivity or accuracy but only an experimental obstacle: a sample mounted on a cantilever is difficult to cool inside an UHV chamber.

## 2.5 Torsion oscillation magnetometer (TOM)

The torsion oscillation magnetometry was first described by Griffiths and MacDonald [72]. It measures the torque of a magnetic sample in an oscillating external field. The sample is attached at a torsion wire. Since the results only depend

on the geometry, the applied field, and the torsion module of the wire TOM provides absolute magnetometric information. The sensitivity of this method was improved by Gradmann. Later on, TOM was realized in UHV [30]. The setup is sketched in Fig. 2.4. Since the substrate is mounted to a torsion wire, cooling of

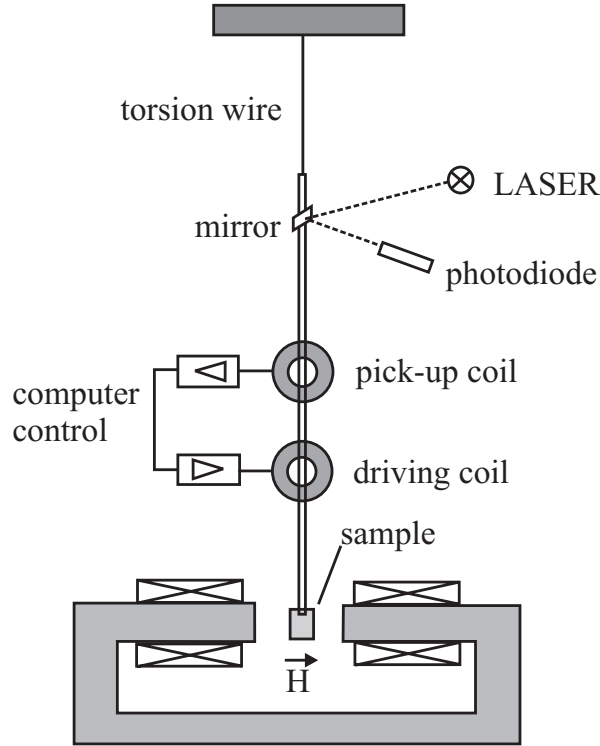


**Figure 2.4:** Principle setup of a TOM. The drawing was taken from [73].

the sample is only possible down to 260 K [30]. With a second setup, magnetometry is possible between 130 and 700 K [18]. Moreover the mounting of the sample hinders easy compatibility with other techniques. The sensitivity is estimated to be  $10^{-2}$  ML of Ni [30]. The magnetometer requires an external magnetic field for the measurements. The TOM provides precise values for magnetic anisotropies and magnetic moments of bare and capped ultrathin films and pioneering results on Ni and Fe surfaces are reported in Section 1.2. However, like for the AGM, the sensitivity does not limit the measurements but the accessible temperature range. Compared to the AGM, the possibility to cool down to 130 K is a valuable improvement.

## 2.6 Magnetic force microscopy (MFM)

The MFM is one of the promising methods to perform space resolved magnetometry [74]. This method is based on atomic force microscopy (AFM) with magnetic cantilevers. Although not applicable in UHV yet<sup>2</sup>, the MFM provides magnetometric information on a  $\mu\text{m}$ -scale. The calculation of the magnetization needs corrections with respect to the sample geometry since the sensor (cantilever) is in close proximity to the sample. Up to now the measurements have a large uncertainty of  $\sim 30\%$  but within the monopole approximation for the sample geometry the outcome roughly agrees with a comparative SQUID measurement [74]. However, it is possible to gain quantitative magnetic information on a magnetic dot with a diameter of 270 nm.

## 2.7 Superconducting quantum interference devices (SQUIDs)

A SQUID consists of a superconducting loop and a weak link, the so-called Josephson junction [5]. These devices give rise to an output voltage signal, which is a periodic function of the flux  $\Phi$  threading the superconducting loop in which one or two weak links are inserted. The latter geometry is termed dc-SQUID (constant bias current  $I_B$ ). Those with a single junction are called radio frequency (rf)-SQUIDs (oscillating bias current  $I_{rf}$ ), see Fig. 2.5. If the superconducting material has a critical temperature  $T_c$  below  $\sim 10$  K (conventional superconductor) the device is called low- $T_c$  SQUID. These devices are mainly made of Niobium (Nb,  $T_c = 9.25$  K). If  $T_c$  is above this temperature one speaks of a high- $T_c$  SQUID. High- $T_c$  superconducting ceramic oxides were discovered in 1986 by Bednorz and Müller [75]. Since then rapid progress has been made in fabricating high- $T_c$  SQUIDs mainly made from  $\text{YBa}_2\text{Cu}_3\text{O}_{7-x}$  (YBCO,  $T_c = 93$  K) which needs only liquid nitrogen ( $\text{LN}_2$ ) for cooling, see [76] for a review. Using ( $\text{LN}_2$ ) for cooling has important advantages: it is cheaper, easier to handle and has a greater cooling power than liquid Helium (lHe) which is required for Nb. There exists a large variety of possible applications for SQUIDs like magnetocardiology, microscopy [77, 78], geophysics, and non-destructive evaluation [79]. Since there exists a large amount of books and review articles dealing with the underlying physics of a SQUID, e.g. [6, 7] only a short discussion of the principles of operation will be given here.

---

<sup>2</sup>Since an AFM is applicable in UHV, this should be possible for the MFM as well, and it certainly will be realized soon.

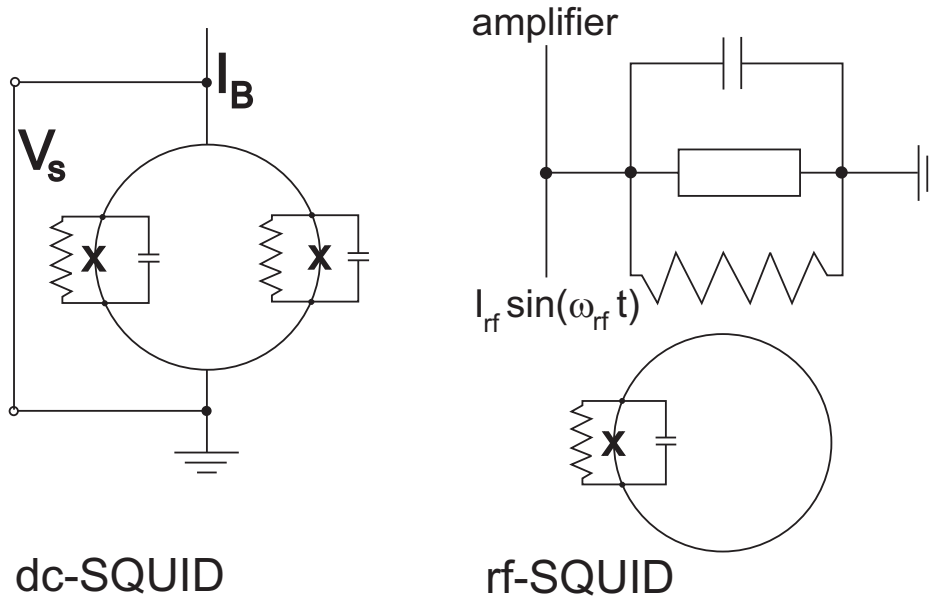


**Figure 2.5:** Schematics of a dc- and a rf-SQUID. The Josephson junctions are marked by “x”. The dc-SQUID is biased with a dc current  $I_B$ . The rf-SQUID is inductively coupled to a rf tank circuit with an oscillating bias current  $I_{rf}$ . Each Josephson junction is shunted by a resistor, the physical capacitance of the junction is indicated as well.

### 2.7.1 Principles of operation

A Josephson junction is a thin insulating layer which interrupts a superconductor. Its electrical properties are governed by the two Josephson equations. Since the junction is non-superconducting only a tunnel current is able to flow through it. Let  $\Psi = \Psi_0 e^{i\Theta_i}$  be the superconducting order parameter and  $\Theta_i$  are the phases on the two sides of the junction. Then the relative phase  $\delta = \Theta_1 - \Theta_2$  is the relevant quantity. The current  $I$  through the ideal junction is given by the dc Josephson equation:

$$I = I_0 \sin \delta \quad (2.1)$$

while the voltage  $V$  across the ideal junction is given by the ac Josephson equation:

$$V = \frac{\hbar}{2e} \left( \frac{d\delta}{dt} \right) \quad (2.2)$$

A real junction has its own physical capacitance and is shunted by a resistor, both joined in parallel to the junction as indicated in Fig. 2.5. They must be considered in an accurate model of the electrical properties of the SQUID [79].

A superconducting loop will contain flux only in multiples of the flux quantum  $\Phi_0$ , i.e.  $n\Phi_0$ , where  $n$  is any integer. A change in flux applied to the loop will cause currents to oppose that change leading to a change in the relative phase

which according to eq. (2.2) gives rise to a voltage leading to a typical  $I - V$  characteristic sketched in Fig. 2.6 (a) for a dc-SQUID. The voltage oscillates between  $V_{min}$  and  $V_{max}$  when  $\Phi$  changes by  $\Phi_0$  as indicated in Fig. 2.6 (b). Thus the SQUID acts as a nonlinear flux-to-voltage transducer.

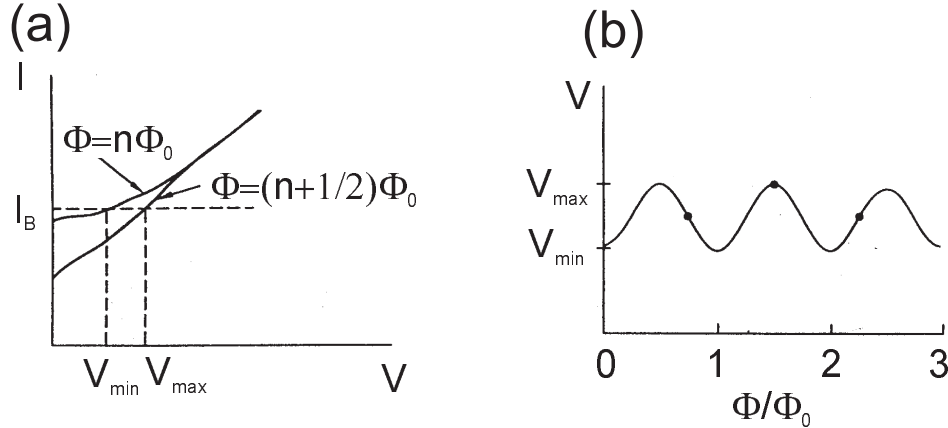


**Figure 2.6:** (a) The  $I - V$  characteristics of a dc-SQUID. The amount of flux  $\Phi$  determines the output voltage  $V$  for a particular value of the bias current  $I_B$ . As the applied flux varies between  $n\Phi_0$  and  $(n + 1/2)\Phi_0$  the output voltage changes between  $V_{min}$  and  $V_{max}$ . (b) The resulting  $V - \Phi$  curve of a dc-SQUID at a given bias current [79].

The  $V - \Phi$  curve is linearized with the help of the so-called flux-locked loop (FLL). The mechanism of the FLL is described in detail e.g. in [7] and in [79]. The basic idea is to keep the system at a constant flux of  $(n/2)\Phi_0$ , i.e. one of the extrema in the  $V - \Phi$  curve. A modulating flux with an amplitude smaller than  $\Phi_0/2$  is applied and the response of the SQUID is fed into a lock-in amplifier. On changes in the applied flux the output of the SQUID will contain a component of the modulating flux and lock-in detection will give rise to a dc-signal. This signal is essentially an error signal which is fed into an integrator. The output voltage of the integrator can be calibrated with a known field.

Besides the direct detection of magnetic flux with the SQUID loop itself there is also the possibility to set up a flux transformer to bridge the distance between sample and SQUID. A flux transformer consists of a superconducting wire which forms two coils with different area and number of turns. Besides flux transformer detection a gradiometer setup of two or more SQUIDs can be used to detect magnetic flux gradients. A flux transformer with three or more different coils can be used for a gradiometric setup as well, see e.g. Fig. 2.7. These gradiometers are able to work even in a magnetically unshielded environment. A large variety of different detection geometries and gradiometric setups was invented for different applications and it will go beyond this work to discuss this large variety, see e.g.

[76] and [79] for a review. Moreover details about noise and sensitivity limits can be found there. The intrinsic sensitivity of a SQUID is in the order of  $10^{-12}\text{T} - 10^{-15}\text{T}/\sqrt{\text{Hz}}$  whereas it turned out, that the signals expected in this work are in the nT-regime (even in the case of 1 ML of Ni). Therefore the sensitivity of a high- $T_c$  SQUID is in principle by far sufficient to detect the magnetic signal of a single ML of Ni.

### 2.7.2 UHV-compatible setups

In this work a novel UHV-SQUID magnetometer is described based on a high- $T_c$  SQUID. Low- $T_c$  SQUID magnetometry has been applied in UHV before [80, 81]. In comparison to the low- $T_c$  SQUIDS the present setup is more simple, cost effective, and needs only  $\text{LN}_2$  for cooling which simplifies the combination with an UHV chamber and with other techniques. The main disadvantage of the novel UHV-SQUID is that it is impossible to apply an external magnetic field during the measurements so far. This occurs because the magnetometer measures directly the stray field of the sample.

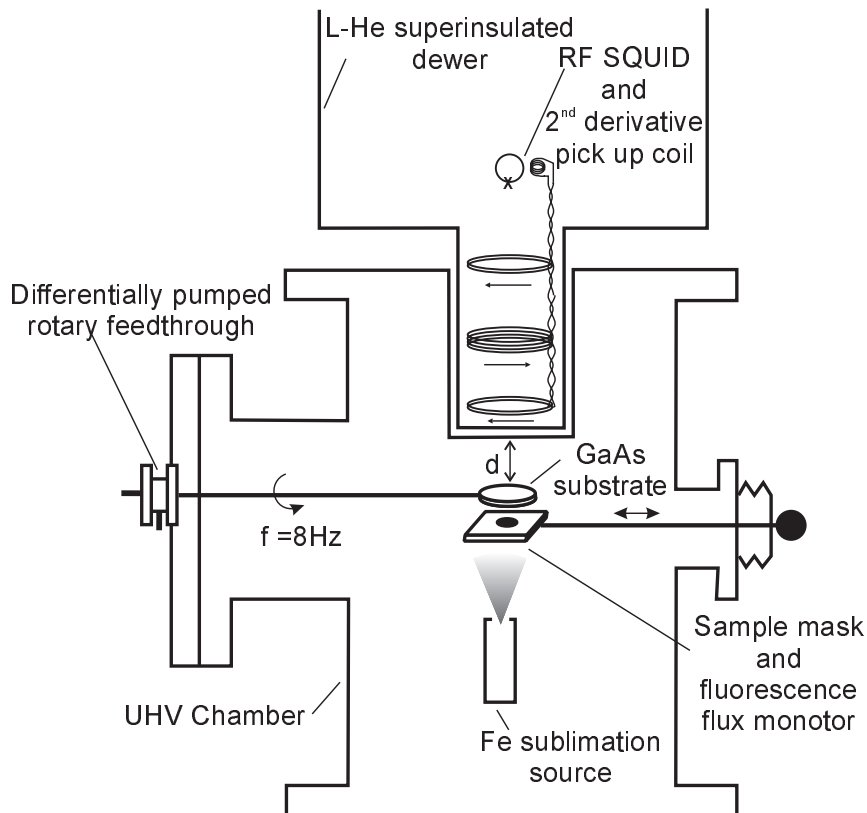


**Figure 2.7:** Schematics of the UHV low- $T_c$  SQUID setup discussed in [80].

One of the former solutions (sketched in Fig. 2.7) used a rotating sample (8 Hz) and a second derivative gradiometer setup [80]. The spinning sample caused experimental difficulties: On the one hand, vibrations of the sample lead to uncertainties in calibrating the machine. Therefore, this has to be done with the help of a bulk sample. On the other hand, cooling of the sample and applying an external field was not possible. The sensitivity limit is  $10^{-6}$  emu [80].

Another UHV-SQUID magnetometer offers the possibility to cool the sample down to 4.2 K and to apply an external field since it uses a standard low- $T_c$  SQUID magnetometer [81]. In order to combine this with an UHV chamber, a complicated transfer mechanism was built up to bring the sample inside the magnetometer. The mounting of the sample causes a magnetic background of  $\sim 10^{-6}$  emu. Measurements with signals of  $6 \cdot 10^{-4}$  emu were shown in [81]. The authors estimate the sensitivity limit to be in the order of the background of the sample holder and therefore it is comparable to the one in [80].

Both solutions for an UHV-low- $T_c$  SQUID magnetometer suffered from its complicated detection mechanisms. The rotating sample led to a loss of almost all advantages of an *ex situ* SQUID, i.e. the absolute calibration, the possibility to cool the sample, and to apply an external field. The direct combination of a standard low- $T_c$  SQUID magnetometer with an UHV chamber offers all abilities but complicates the handling of the sample leading to slow measurements, to a large and expensive machine, and to difficulties in combining the magnetometry with other magnetometric techniques. The capabilities of the present setup will be discussed in detail in the following Chapter.

### Summary

The experimental capabilities of the *in situ* magnetometries discussed in this Chapter are summarized in Table 2.1. The sensitivity<sup>3</sup> is given in emu, where  $10^{-6}$  emu roughly correspond to 0.1 ML of Fe or Co over a  $0.5 \text{ cm}^2$  area. The  $M(T)$ -column indicates the possibility to access *low* temperatures to measure the ground-state magnetic properties.

Method	Sensitivity	M(T)?	M(H)?	absolute?	Ref.
<b>MOKE</b>	$10^{-5}$ emu	yes	yes	no	e.g. [53]
<b>XMCD</b>	$< 10^{-7}$ emu	yes	yes	no	e.g [50]
<b>PNR</b>	$< 10^{-5}$ emu	yes	yes	yes	[63]
<b>AGM</b>	$10^{-8}$ emu	no	yes	yes	[67]
<b>TOM</b>	$< 10^{-7}$ emu	$> 130 \text{ K}$	yes	yes	[18]
<b>low-<math>T_c</math>-SQUID</b>	$10^{-6}$ emu	no	no	no	[80]
<b>low-<math>T_c</math>-SQUID</b>	$10^{-6}$ emu	yes	yes	yes	[81]
<b>high-<math>T_c</math>-SQUID</b>	$10^{-6}$ emu	yes	no	yes	this work

**Table 2.1:** Different types of *in situ* magnetometries. Listed are the sensitivity, the possibility to cool, and to measure under an external magnetic field according to the given references.

---

<sup>3</sup>For XMCD and PNR no explicit sensitivity limit is given in the References. Both techniques should be submonolayer-sensitive ( $\leq 10^{-8}$  emu). The stated values correspond to published measurements (as a rough estimate).

# Chapter 3

## Experimental details

This chapter describes the design of the novel UHV-SQUID magnetometer. Furthermore, details of the calibration and the data analysis will be given. The development and the characterization of this type of magnetometer was done for the first time in the present thesis. Therefore, it may serve as a reference for future work and provides technical informations of interest. Detailed drawings and the wiring diagrams of the motor control can be found in the Appendix. Finally, a brief section describes the sample preparation.

### 3.1 Design of the UHV-SQUID magnetometer

Before setting up a novel magnetometer the desired properties of the intended machine have to be specified. The basic idea behind the novel setup was to combine the high sensitivity of a SQUID with the possibility to measure *in situ* in UHV to determine ground-state magnetic properties on an absolute scale. Prior setups of UHV-SQUID magnetometers [80, 81] resulted in quite large and complicated constructions combining commercial low- $T_c$  SQUID magnetometers with an UHV chamber. The requirements for the present solution were the following: The magnetometer should be simple, fast, cost-effective and easy to combine with other measuring techniques, i.e. combining SQUID magnetometry with MOKE or Ferromagnetic Resonance (FMR). The chosen solution is a commercial high- $T_c$  SQUID magnetometer, an UHV-compatible metal dewar with glass-finger tip shielded with a double  $\mu$ -metal cylinder, and an usual UHV-manipulator with lHe cooling capabilities. The magnetic stray field of the sample is measured directly by the SQUID while scanning the magnetic sample along the SQUID plane. So far, this has hindered applying an external field and restricts the measurements to the remanent state.

A brief “checklist” may summarize the most important general requirements for a successful combination of UHV and SQUID:

1. Cooling of the SQUID in combination with an UHV chamber.

2. Magnetical shielding of the SQUID.
3. Electrical shielding of the SQUID.
4. Easy compatibility with other UHV techniques like LEED, AES ...
5. Sample holder suitable for a temperature range from 40 to 870 K.
6. No ferromagnetic signal originating from the sample holder.
7. Accurate determination of the geometry of the measurement.
8. Dense recording of the stray field of the sample.

These points are only in favor of a setup that directly measures the stray field. The chosen solutions concerning these requirements are the following:

1. A metal dewar (Fig. A.1) with a CF 35 flange and suitable SQUID sensor (Fig. 3.1).
2. Double  $\mu$ -metal cylinder (Fig. A.2) surrounding the dewar tip.
3. Electrical decoupling of the chamber (dewar) and the rf-shield of the SQUID using a dewar with a glass finger tip (Fig. A.3).
4. Usage of a standard UHV manipulator.
5. He cooling facility of the manipulator, Cu-made sample holder, and resistive heating capability provided by W wire mounting.
6. PtRh thermocouple, sample holder solely made of Cu, W and ceramics. (Fig. 3.3).
7. Usage of a quartz-balance combined with a high-precision evaporation mask (Fig. 3.11).
8. Continuous driving of the manipulator and light barrier triggered read-out of the SQUID output (Fig. 3.5).

### 3.1.1 The high- $T_c$ -rf-SQUID sensor

In the last decade high- $T_c$  superconductors became commercially available. There exist companies providing complete systems of high- $T_c$  SQUID magnetometers. The SQUID system of the F.I.T. company (HM1, [82]) used in this work consists of an rf-SQUID made out of YBCO deposited on a SrTiO<sub>3</sub> substrate with a single weak link fabricated by oxygen-ion implementation. The modulation frequency of the tank circuit is 19.6 MHz. The ultimate sensitivity is specified to be  $2.0 \cdot 10^{-12}$  T/ $\sqrt{\text{Hz}}$ . The magnetometer was originally intended for applications

like field distribution measurements of magnetic minerals [83]. For the present setup the sensor was rebuilt according to Fig. 3.1 to fit inside the dewar. The magnetic flux is measured over an area of about  $200 \times 200 \mu\text{m}^2$ . In principle, this offers the possibility to have spatial resolution in the same order of magnitude. In general, the resolution of a SQUID microscope is limited by the size of the hole of the superconducting ring or the distance to the sample depending on which quantity is larger [77], see Section 3.3.3.

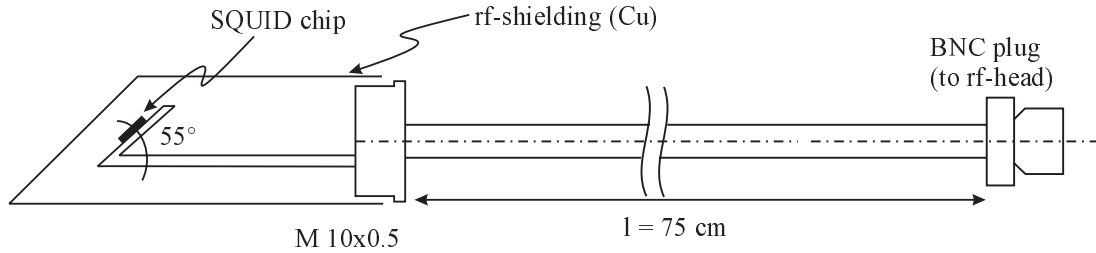


**Figure 3.1:** Sketch of the SQUID sensor (“Cryogenic probe”). The chip is glued to the holder using polymethyl methacrylate (PMMA). The coil and the capacitor of the tank circuit are not shown; the coil is glued directly on top of the chip.

A control unit is available as well and provides an output signal ( $\pm 10 \text{ V}$ ) proportional to the measured flux. The sensitivity can be reduced by a factor of 10 or 100 to have the possibility to measure larger magnetic signals. The use of frequency filters provided by the power supply did not improve the noise while running the SQUID combined with the UHV chamber and, therefore, was not necessary. On the other hand it was necessary to avoid a common electrical grounding of the vacuum pumps and the SQUID power supply. Otherwise operation of the SQUID was impossible due to strong electrical background noise. The connecting cable between SQUID power supply and rf-head should be kept in the largest-possible distance from the turbo-pump to minimize radio-frequency noise. In summary, the operation of the SQUID magnetometer in an usual UHV laboratory environment is possible.

### 3.1.2 The UHV-compatible metal dewar

The SQUID sensor (Fig. 3.1) is kept *ex situ* under  $\text{LN}_2$  in an UHV-compatible metal dewar and is removable. This is necessary during the baking procedures and for warming up (by blowing dry air to the chip) since the SQUID chip can stand neither temperatures above  $80^\circ\text{C}$  nor water. The dewar is mounted at the chamber under an angle of  $55^\circ$  to the verticality by a CF 35 rotatable flange as sketched in Fig. 3.2.<sup>1</sup> The dewar ends in a CF 16 flange on the vacuum side, see

<sup>1</sup>The angle is given by the used vacuum chamber.

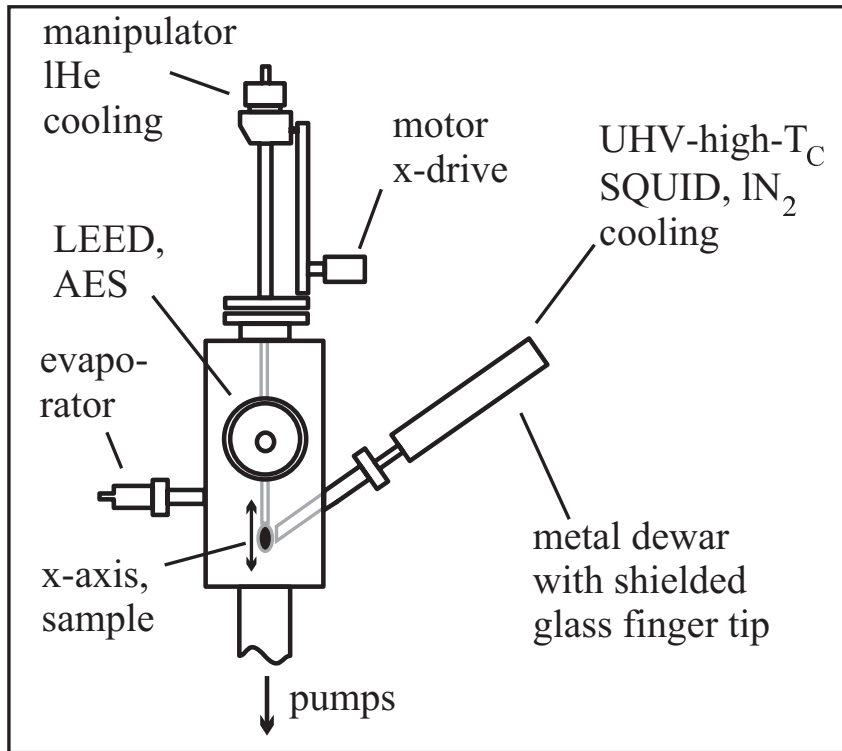


**Figure 3.2:** Sketch of the dewar mounted at an UHV-chamber. The shielded glass finger tip pointing inside the chamber is indicated.

Figs. A.1 and A.3. This enables mounting different tips for different measuring geometries depending on the requirements of the experiment. In this case, a glass metal transition (Pyrex-to-Kovar) is used (see Fig. A.3). This turned out to be the adequate solution to minimize radio-frequency noise in the tank circuit of the rf-SQUID since a metallic dewar-tip would act as an antenna. The CF 16 flange offers the opportunity to mount a double  $\mu$ -metal cylinder as magnetic shielding (Fig. A.2). This suppresses the magnetic background down to  $\sim 0.02$  nT. The remaining background is due to radio frequency noise originating from the turbo-pump and the pre-pump of the vacuum system<sup>2</sup>. The static field of the ion-getter-pump does not affect the operation of the SQUID.

The magnetically shielded tip of the dewar points inside the chamber (see Fig. 3.2) and can be retracted since the dewar is connected to the chamber with a linear motion. The sample enters the shielding through a small slit of  $4 \times 8$  mm<sup>2</sup> (indicated by the arrow in Fig. A.3). The sample is separated from the SQUID by the glass window of the dewar tip. The minimum distance between SQUID and sample is given by space limitations: The glass window is 1.3 mm

<sup>2</sup>Of course, an 1 T magnet in operation in a distance of  $\sim 5$  m would cause a background of  $\sim 10$  nT which hinders reliable data acquisition.

thick, the SQUID is covered by the coil of the tank circuit (0.5 mm) and kept inside a Cu cylinder (1.5 mm) to screen radio frequencies. Another 0.5 mm of vacuum separates the sample from the glass window. This sums up to  $\sim 4$  mm of minimum distance.

During about 1.5 years of operation it turned out, that the glass-to-metal transition is suitable for UHV applications concerning baking procedures and cooling with  $\text{LN}_2$ , i.e. temperatures between 77 and 550 K. However, filling the dewar directly with  $\text{LN}_2$  may lead to small cracks in the glass-metal transition resulting in considerable leakage ( $10^{-5}$  mbar range). Therefore, it should be assured that the glass is cooled down before the metal, e.g. by blowing cold  $\text{N}_2$  gas into the tip. This avoids thermal tensions between glass and metal (which cools down much faster than the glass). A suitable procedure is to fill the  $\text{LN}_2$  with the help of a small pipe at a low rate directly into the glass tip instead of pouring the liquid into the dewar. Moreover, a Pyrex-to-Kovar transition should be preferred although Kovar is magnetic. The Pyrex-to-Kovar transition is the better choice since the thermal expansion coefficients of these two materials match better compared to stainless steel and the magnetometer is able to operate in the static magnetic field caused by the Kovar. Nevertheless, one can succeed with a stainless steel transition as well.

### 3.1.3 The sample holder

A sample holder suitable for measuring the magnetic stray field must solely consist of non-ferromagnetic material. It should have good thermal conductivity to reach low temperatures, and provide heating capabilities for the sample preparation. Its dimensions must fit the small slit in the  $\mu$ -metal cylinder ( $4 \times 8 \text{ mm}^2$ ) and it must be UHV-compatible. A Cu-made<sup>3</sup> sample holder with a crystal mounted by a W wire fulfills these requirements. The wire enables resistive heating of the crystal. A non-ferromagnetic Pt-PtRh thermocouple is used to monitor the sample temperature. The whole setup is sketched in Fig. 3.3. The length of the crystal mounting is determined by the diameter of the magnetic shielding. To access the whole inner diameter of the cylinder the length must not be shorter than 3 cm. For a better thermal conductivity the W wire is not used over the entire length of the holder but is partly replaced by Cu tubes. The wire itself must be electrically isolated with respect to the manipulator to provide resistive heating capabilities. This is realized by two Cu parts which enable mounting of the Cu tubes (Fig. A.4). They are electrically isolated with the help of a Polyimide foil. The losses in cooling power due to the 0.1 mm thick foil result in a by 1-2 K higher sample temperature, see Fig. 3.3. The sample is a Cu(001) single crystal having its in-plane [110] crystallographic axis parallel to the verticality.

The sample holder permits to measure at temperatures from 300 K to 40 K

---

<sup>3</sup>The used Cu is oxygen-free, so-called OFHC.

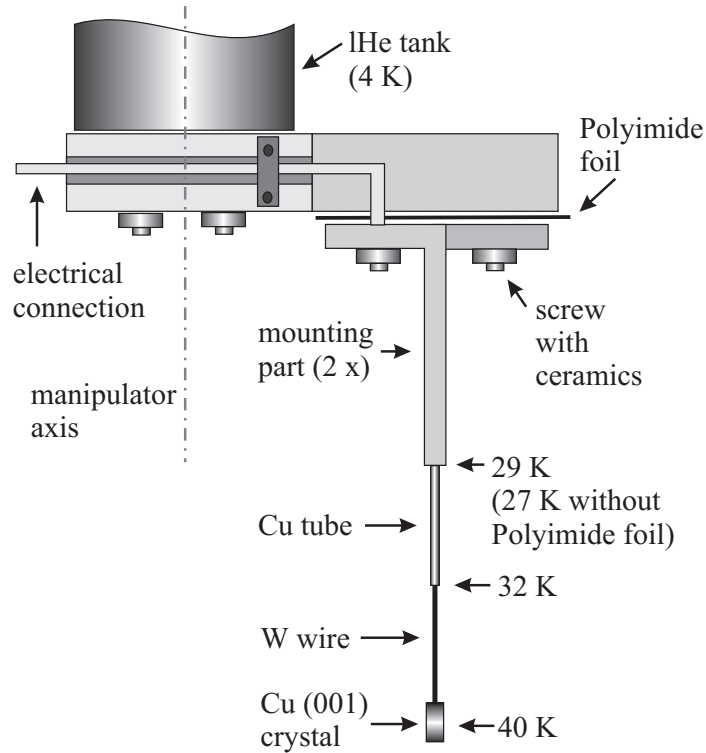


**Figure 3.3:** Sketch of the sample holder. Measured temperatures at different spots are shown to follow the temperature gradient to figure out the major losses of cooling power. A detailed drawing of the two mounting parts can be found in Fig. A.4.

if lHe is used for cooling; by using  $\text{LN}_2$  the lowest accessible temperature is about 90 K. It should be stated that the use of a Pt-PtRh thermocouple makes the temperature determination difficult below  $\sim 80$  K since the thermocouple coefficient does not behave linearly in this temperature regime. Therefore, a careful calibration with a ferromagnetic Ni-CrNi thermocouple (which is at least suitable for temperatures down to 10 K) was performed to calibrate the Pt-PtRh thermocouple. For the crystal preparation annealing temperatures of 870 K are required which are easily reachable by applying a current of about 5-7 A to the W wire. Measuring temperatures higher than 300 K are not easily accessible because resistive heating causes magnetic fields close to the SQUID so that no reliable measurements are possible. A solution for temperatures up to 400 K may be to pour hot water into the cryostat of the manipulator. This would require the possibility to pump liquids from the cryostat to get rid of the water after the measurement and was not tested so far.

In Fig. 3.3 one can follow the temperature gradient along the sample holder. This may help to find the major losses of cooling power. One can see that at the end of the Cu tube the lowest possible temperature is about 32 K which is within

the estimated region for such a type of sample holder (for a rough estimate see e.g. Appendix of [84]). The large gradient between the end of the Cu tube and the Cu crystal is caused by three major losses: (i) the length of the W wire, (ii) the transition between Cu tube and the W wire and (iii) the transition between crystal and wire. The optimization of (i) is limited: The length of the W wire is determined by two conflicting interests: a long wire ( $\sim 2 - 3$  cm) permits low currents for heating ( $\sim 2 - 3$  A) but the lowest measuring temperature is then about 70 – 80 K. A short wire (below  $\sim 1$  cm) allows a temperature around 50 K but then a current of 10 A is hardly sufficient to reach the desired annealing temperature. (ii) can be minimized by squeezing the Cu tube. The inner diameter of the used tubes is about 0.5 mm while the diameter of the wire is 0.3 mm. (iii) can not be optimized in a simple manner. The most recent experiments on Ni films (see Chapter 5) were performed with an optimized mounting of the crystal following carefully the above discussion resulting in a sample temperature of 40 K – the lowest temperature reached with this holder so far.

## 3.2 Operation of the magnetometer

The description of the operation of the novel UHV-SQUID magnetometer contains the calibration of the sensor, the data acquisition, and the discussion of the sensitivity limit.

### 3.2.1 Calibration of the SQUID

A SQUID is able to detect the magnetic flux across its area and to convert this into an output-voltage. In order to obtain the output of the SQUID in absolute field units the magnetometer has to be calibrated. With the SQUID control unit of the F.I.T. company (model HM 1U) [82] this calibrating factor can not be changed by the settings of the control unit. Using a control unit with more tuning possibilities for the tank circuit (e.g. a S.H.E. electronic [85]) this factor can be changed. Therefore a re-calibration is necessary each time the tank circuit is newly tuned. Note, that the SQUID runs well with both electronics, F.I.T. and S.H.E., although the latter was originally designed for an older low- $T_c$  SQUID. The SQUID is calibrated using two different coil geometries, a Helmholtz coil and a long coil yielding the same values (within 0.1%) for the calibrating factor. Both geometries assure that the applied field is homogeneous within  $10^{-5}$  over the area of the SQUID which is  $5 \times 5$  mm<sup>2</sup>. An *ex situ* setup is used for the calibration. It consists of a glass dewar with a tip surrounded by the calibrating coil which is kept inside a  $\mu$ -metal screening. The whole dewar is surrounded by an Al-cylinder for radio-frequency screening and another  $\mu$ -metal screening. A high-precision current of a few  $\mu$ A is sent through the calibrating coil. By applying Biot-Savart's law, the applied magnetic field is calculated which can be

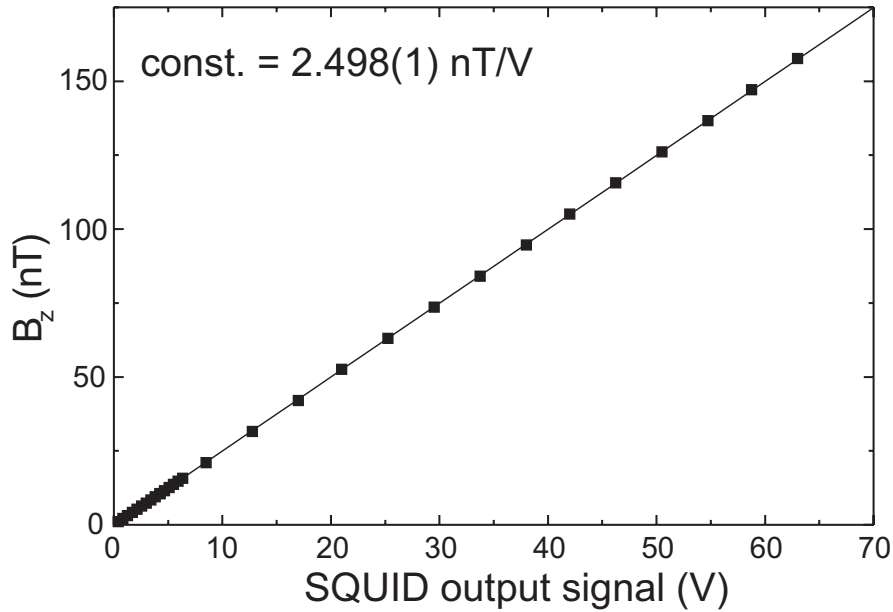


**Figure 3.4:** Calibration of the SQUID output signal using a long coil. One derives 2.498(1) nT/V for the UHV-SQUID.

plotted versus the output-voltage of the SQUID as shown in Fig. 3.4.

The number of turns  $n$  of the Helmholtz coil is three and its radius  $r = 28.6(1)$  mm. The resulting field  $B$  depending on the current  $I$  is:

$$B = \frac{3.2\pi \cdot n}{r\sqrt{125}} \cdot 10^3 \frac{nT}{A} \cdot I \quad (3.1)$$

which gives  $B = 0.094(2) \cdot nT/\mu A$  for the used coil. In case of the long coil the number of turns  $n$  is 72. The radius  $R = 0.0159(1)$  m and the length  $L = 0.080(1)$  m. The resulting field on the axis in the center of the coil is given by [86]:

$$B = \mu_0 \frac{n}{\sqrt{4R^2 + L^2}} \cdot I \quad (3.2)$$

or  $B = 1.051(8) \cdot nT/\mu A$ . In Fig. 3.4 a calibration using the long coil is shown yielding 2.498(1) nT/V as calibrating factor.

Unlike the procedure performed for XMCD or MOKE the calibration of the UHV-SQUID magnetometer does not depend on the investigated ferromagnetic material. It is more comparable to the one done for a vibrating sample magnetometer (VSM). Only the given measuring geometry and the proportionality factor of the electronics are determined while the measurement itself is not sensitive to the intrinsic sample properties like optical constants. In that sense the UHV-SQUID magnetometer performs *absolute* measurements. A “real” absolute measurement depends only on elementary constants like the quantum Hall effect.

### 3.2.2 Data Acquisition

During first experiments to test the magnetometer the manipulator was moved manually and the output voltage was recorded with a  $y(t)$ -plotter. The achievable density of data points turned out to be insufficient to determine the distance between the sample and the SQUID. As this parameter is a crucial input – the error in determining the distance governs the uncertainty of the fitted magnetization – another solution had to be found. This is to use a motor driven manipulator controlled by a newly designed motor control unit and data acquisition with the help of a computer as sketched in Fig. 3.5. Details concerning the motor control unit and the computer programs can be found in the Appendix.

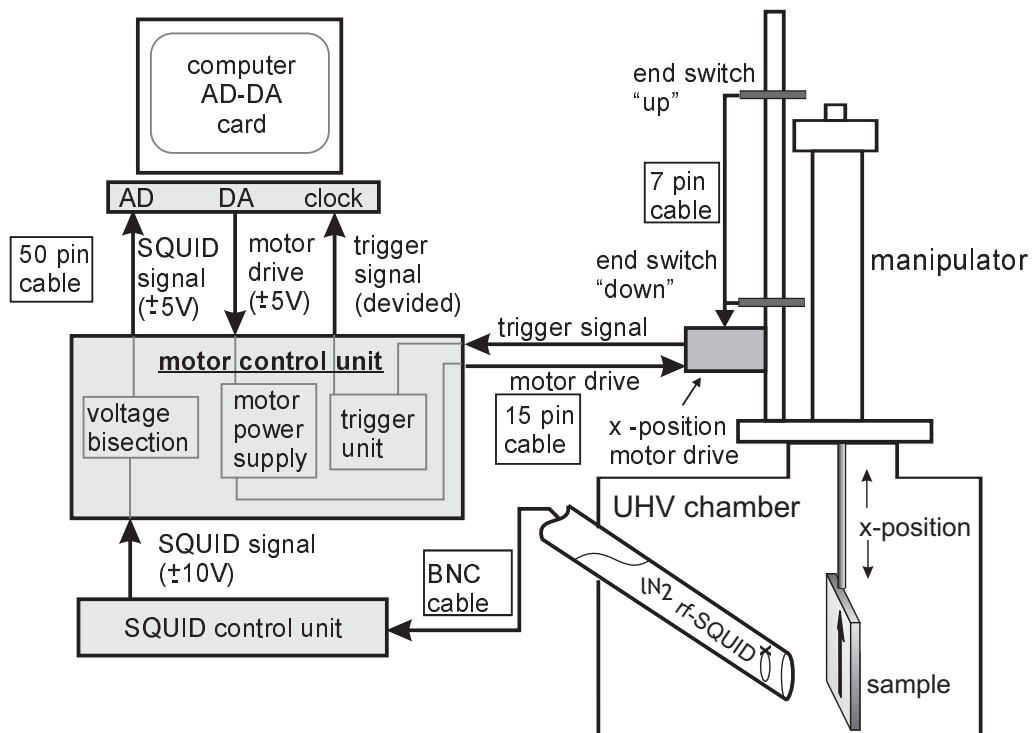


**Figure 3.5:** The data acquisition is performed by a computer in the following way: a voltage of  $\pm 5$  V from the digital-to-analogue (DA) converter can be applied to the motor control unit to drive the manipulator up/down. While the motor is rotating, a light barrier triggers the “clock”-input of the computer card to trigger analogue-to-digital (AD) conversion of the bisected SQUID output signal. Two end switches define the range of the accessible x - position.

The manipulator is driven by a motor with a gear reduction of 125:1 where one turn of the manipulator corresponds to 1 mm of movement. Every turn the motor interrupts a light barrier and triggers a single read-out of the SQUID

output voltage by a AD-DA computer card. The manipulator is driven continuously starting with the sample inside the  $\mu$ -metal shielding until the sample is completely outside the screening (to obtain the zero line) and then backwards to exclude hysteresis effects in the measurement. The motor control enables reducing the density of the recorded points by a factor of 8, 16, 32 etc. It turned out that a reduction factor of 8 is sufficiently dense. Accordingly, the stray field is recorded in steps of 0.064 mm. It is important to avoid using a stepper motor to minimize the vibrations of the manipulator.

The data are recorded with the help of an AD-DA card controlled by a simple C+ program given in the Appendix. The maximum voltage allowed is  $\pm 5$  V with a resolution of 12 bit<sup>4</sup>. This corresponds to a resolution of  $\sim 2.4$  mV which is sufficient since the background noise corresponds to about 80 mV. The sampling frequency of the card is in the order of kHz while the motor rotates at about 10 to 20 Hz. This implies that one field scan over the whole inner diameter of the shielding (2.88 cm = 450 steps using a reduction factor of 8) – for both directions, “up”, and “down” – takes only 3–4 minutes. Since a single scan is sufficient to determine the magnetization, the new UHV-SQUID magnetometer offers the possibility of very fast measurements minimizing the contamination of the sample by residual gases.

### 3.2.3 The ultimate sensitivity

The sensitivity of the UHV-SQUID magnetometer is mainly given by the electrical and magnetic noise originating from the laboratory environment. The resulting noise while running the SQUID inside the UHV chamber is  $\sim 0.2$  nT. It should be noted that the noise does not increase with decreasing temperature. This implies that the sensitivity of the magnetometer is available over the complete accessible temperature range from 300 to 40 K. Figure 3.6 shows a  $3 \times 3$  mm<sup>2</sup> film of 2.9 ML of Co measured at ambient temperature. Only one single scan was taken and no data smoothing has been performed. The magnetic peak-to-peak signal of the sample is about 8 nT. This yields a signal-to-noise ratio of 40:1. The measured signal scales linearly with respect to the film thickness and magnetization. The limiting signal-to-noise ratio is assumed to be about 3:1. Therefore, the sensitivity limit is about 0.3 ML of Co for one single scan (!). This corresponds to  $10^{-6}$  emu which is in the same order of magnitude as for low- $T_c$  UHV-SQUIDS. Consequently, the present setup of an UHV-SQUID magnetometer provides *submonolayer sensitivity*. This is confirmed by recent measurements on Ni films, see Chapter 5.

---

<sup>4</sup>Since the output of the SQUID is  $\pm 10$  V, the signal has to be bisected first.

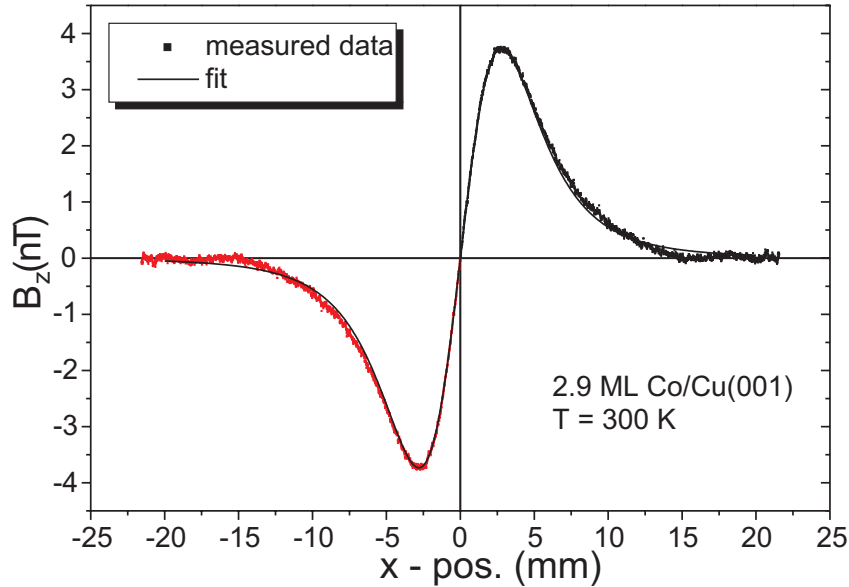


**Figure 3.6:** Measured stray field for a 2.9 ML Co/Cu(001) film for one single scan without any data-smoothing. The recording time was about 4 min. The signal-to-noise ratio is about 40:1 which shows the ultimate sensitivity of the present setup. The fit is discussed in the following.

### 3.3 Details of the data analysis

The data recorded with the UHV-SQUID are analyzed by fitting them with a calculated stray field distribution, see Fig. 3.6. This Section introduces the formulas which are used to discuss the expected shape of stray field distribution as well as the spatial resolution of the magnetometer. It is described how to derive the necessary parameters of the measurement to fit the magnetization.

#### 3.3.1 The measuring geometry

Performing measurements with the UHV-SQUID magnetometer the magnetic stray field of the sample is recorded as a function of space. The majority of the studied samples is magnetized in the sample plane. For that reason Fig. 3.7 only shows this case, it can easily be generalized for a sample magnetized perpendicular to its plane. The stray field of a sample with magnetization  $M$  in the film plane is sketched in Fig. 3.7. As a SQUID can only detect magnetic flux perpendicular to its plane it is only sensitive to the  $z$ -component of the stray field using the coordinate system of Fig. 3.7. Varying the  $x$ -position ( $x - pos.$ ) of the sample, the magnetic field component  $B_z$  is recorded keeping the film centered with respect to the SQUID loop. The distance  $h$  between the sample and the

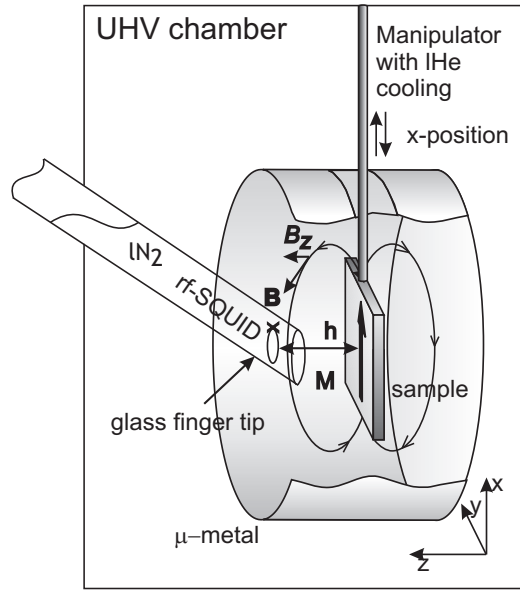


**Figure 3.7:** Schematic sketch of the geometry of the measurement. The measured quantity  $B_z$  and the distance  $h$  between sample and SQUID are indicated.

SQUID is indicated as well.

Unlike other UHV-SQUID magnetometers [80, 81] the present setup measures the stray field generated by the sample. This is usually done if SQUID microscopy is performed like in [77, 78, 87, 88]. This is more cost-effective and the technical realization is less complicated. The use of a standard UHV-manipulator in combination with IHe cooling capabilities obviates complicated transfer mechanisms like in [81].

### 3.3.2 Calculated stray field

Following [88] (see also [77] for current densities) the stray field of a thin film can be calculated by integrating elementary magnetic moments across the sample area. The field  $d\mathbf{B}$  of a magnetic dipole  $d\mathbf{m}$  in a distance  $\mathbf{R}$  is given by:

$$d\mathbf{B} = \frac{\mu_0}{4\pi} \cdot \frac{(3\mathbf{n} \cdot d\mathbf{m}) \cdot \mathbf{n} - d\mathbf{m}}{R^3} \quad (3.3)$$

where  $\mathbf{n} = \mathbf{R}/R$  is an unit vector. By using eq. (3.3) it is assumed that the stray field only originates from magnetic dipoles. This is justified since the stray field is detected at a distance of  $\sim 5$  mm. This assures that the higher order contributions (quadrupole, octupole ...) are negligible small since they vanish with higher ( $5^{th}$ ,  $7^{th}$ , ...) powers of  $1/R$ . The assumption that the magnetization of the sample is caused by a magnetic dipole density is made for other measurements as well, e.g. VSM.

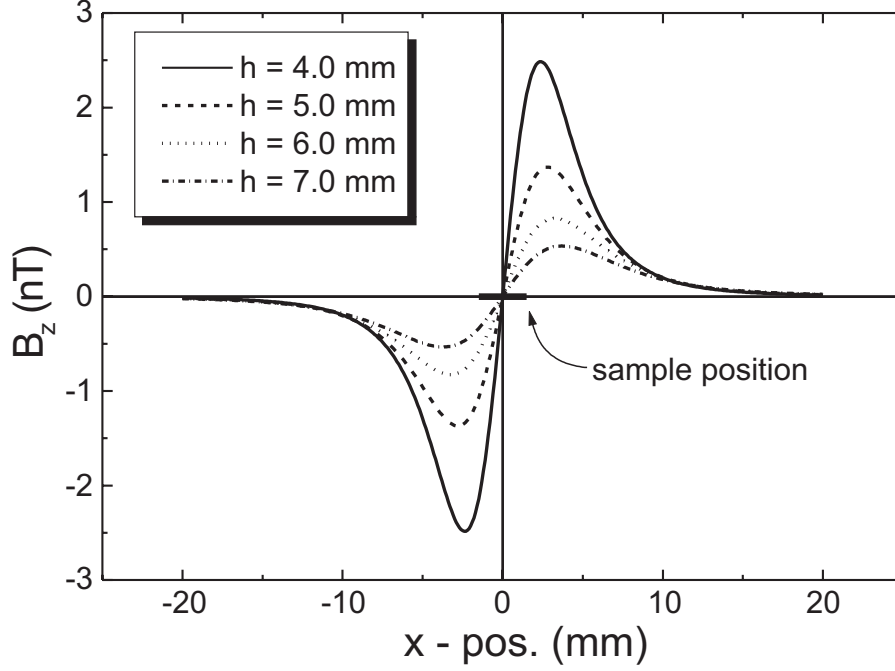


**Figure 3.8:** Calculated stray field distribution of an in-plane magnetized film for various distances  $h = 4, 5, 6,$  and  $7$  mm according to eq. (3.4). The signal corresponds to a square-shaped 1 ML Co film of a width of 3 mm and a bulk-like magnetization of 1475 kA/m.

The sample is square-shaped and of width  $a$ . The film thickness is  $d$ , the magnetization  $M$  is oriented in the film plane. The magnetic dipoles  $d\mathbf{m}$  are located at the position  $(x, y, 0)$  in the film plane. It is assumed that  $d\mathbf{m} = (m, 0, 0)$  has only a  $x$  component  $m$  where  $M \cdot d = \int_A d\mathbf{m} \cdot dx dy$ . Therefore the magnetization is solely of dipolar character and all contributions to the magnetization are projected on the  $x$  axis. This implies that the sample is mounted in a way that the easy axis coincides with the  $x$  axis (direction of movement). The SQUID is moved in a constant distance  $h$  in the  $(u, v)$ -plane measuring the  $z$  component of the stray field  $B_z$  at  $(u, v, h)$ . The integration of eq. (3.3) leads to:

$$B_z^{tot}(u, v, h) = \frac{3\mu_0}{4\pi} M \cdot d \cdot h \cdot \int_{-a/2}^{a/2} \int_{-a/2}^{a/2} \frac{u-x}{R^5} dx dy \quad (3.4)$$

where  $\mathbf{R} = (u-x, v-y, h)$ . The measurement is performed keeping the film centered, i.e.  $v = 0$ . A simple Fortran90 program to calculate  $B_z$  numerically can be found in the Appendix. For this integral there exists a lengthy analytical solution as well (see Appendix). The resulting stray field distribution exhibits two characteristic peaks. Their position and shape depend on  $h$  and the size of the film. Their “amplitudes” (peak-to-peak height) are determined by  $h$ ,  $M$  and

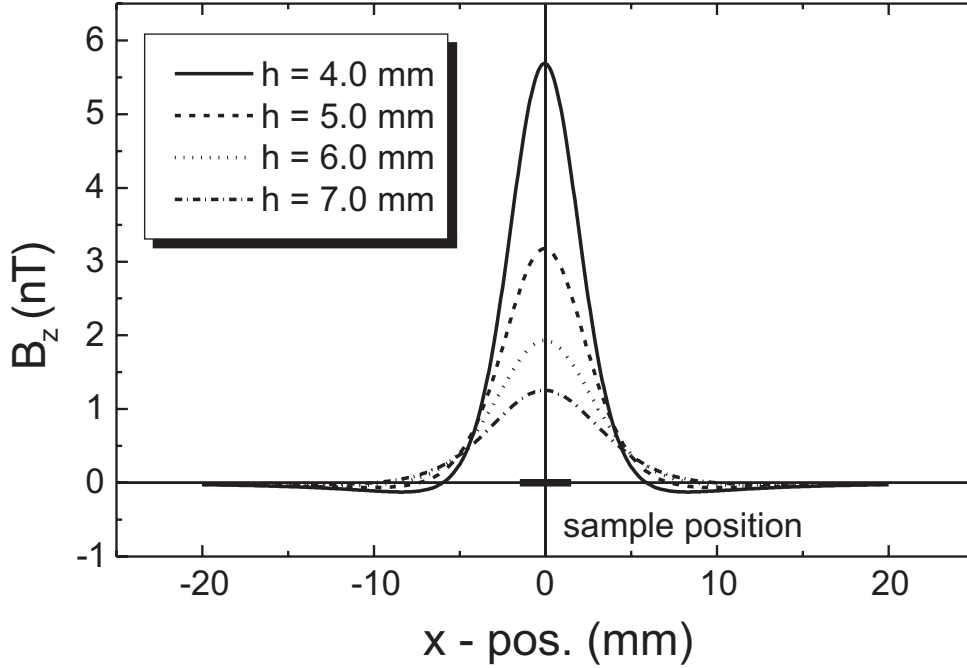


**Figure 3.9:** Stray field distribution for the same film as in Fig. 3.8 but with out-of-plane magnetization according to eq. (3.5).

*d.* To illustrate this, the calculated stray field of a 1 ML Co film with a bulklike magnetization of  $M = 1475$  kA/m is shown for various distances  $h$  in Fig. 3.8.

It is also possible to calculate the stray field for an out-of-plane magnetized film where  $d\mathbf{m} = (0, 0, m)$ . Eq. (3.4) then changes to:

$$B_z^{tot}(u, v, h) = \frac{\mu_0}{4\pi} M \cdot d \cdot \int_{-a/2}^{a/2} \int_{-a/2}^{a/2} \frac{3h^2}{R^5} - \frac{1}{R^3} dx dy \quad (3.5)$$

This integration can be performed by almost the same program as used for eq. (3.4) and is given in the Appendix as well. To illustrate the result, the outcome of eq. (3.5) is plotted in Fig. 3.9 for the same sample as in Fig. 3.8. This yields a field distribution having a single peak. The maximum field value depends strongly on the distance  $h$ , but the shape – especially the width – of the peak is insensitive to changes in  $h$ . It should be noted that for out-of-plane magnetized films the weak dependence of the shape of the field distribution with respect to  $h$  makes the determination of  $h$  difficult resulting in a large uncertainty in deriving  $M$ .

### 3.3.3 Spatial resolution of the magnetometer

As stated above it is – in principle – possible to perform spatial resolved measurements with the UHV-SQUID magnetometer and the resolution is limited by

the distance between the sample and the SQUID [77] which is about 5 mm. The sample size is  $3 \times 3 \text{ mm}^2$ . For thickness dependent measurements it would be

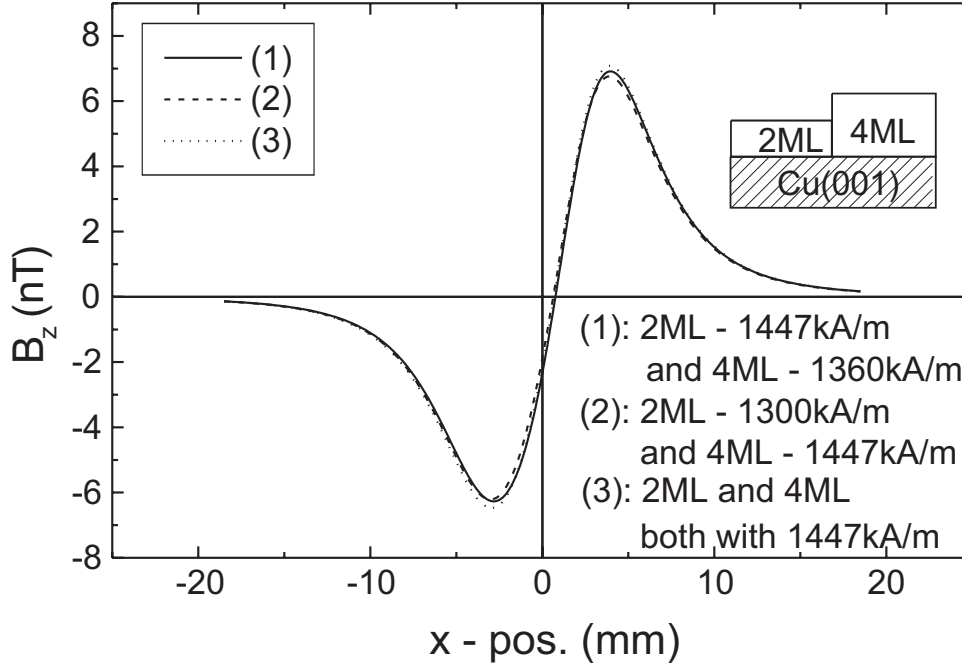


**Figure 3.10:** Calculated stray field for a stepped film with three limiting cases. Either the two parts of the sample have the same magnetization or one of the parts has a by 10% reduced magnetization. One can see that there is no significant difference in the stray field within 0.2 nT.

convenient to measure stepped samples, like in [49]. To test if there is the possibility to measure and analyze a stepped sample with the UHV-SQUID the most ideal case – a sample with one single step – is assumed and the stray field is calculated. Three limiting cases are discussed in Fig. 3.10 for a 2/4 ML Co film. (1) the thick film has a lower magnetization, (2) the thin film magnetization is lower or (3) both magnetizations are equal. (3) is equivalent to the stray field originating from a 3 ML thick film which is slightly shifted with respect to the coordinate system<sup>5</sup>. Figure 3.10 reveals that there is only a small difference in the corresponding stray fields of such samples. The deviations are found to be in the order of 0.1 nT which is smaller than the noise level.

This leads to the conclusion that it is not possible to analyze stepped samples measured with the present setup. The ability to yield spatial resolution gets lost because the distance between sample and SQUID is too large.

<sup>5</sup>The coordinate system for the calculation is usually centered within the film plane. The measurement provides no direct measure of the coordinate system but only a relative  $x$  value.

### 3.3.4 Determination of the parameters

The determination of the magnetization  $M$  with the UHV-SQUID magnetometer needs the following procedure to fit the measured data. In a first step, the stray field  $B_z$  has to be extracted from the measured data. Then the necessary parameters as required by eq. (3.4) have to be determined: the thickness  $d$  of the measured film and its width  $a$ , that is – in other words – the volume of the sample. The knowledge of the distance  $h$  between sample and SQUID plays a crucial role since the uncertainty of  $h$  equals the uncertainty of  $M$ . The last step is to fit the stray field by adjusting the only free parameter left: the magnetization  $M$  of the measured film.

#### Extracting the measured stray field $B_z(x)$

The fact that the sample is moved inside the  $\mu$ -metal cylinder which fits inside a CF 35 flange limits the accessible  $x$ -range. Both maxima of the stray field distribution can be recorded but the zero line is only accessible on one side of the scan range by recording data with the sample outside the shielding. The entire distribution as shown in Fig. 3.6 is derived as follows: The data set  $B_z(x)$  is transformed into  $-B_z(-x)$  and both are plotted together. A linear background attributed to thermal drifts can be subtracted in a way, that the corresponding maxima fall onto each other. If this analysis is valid, the peak shapes of both data sets should be the same and the field for  $|x| \geq 15$  mm should equal zero since the sample is outside the  $\mu$ -metal shielding. In Fig. 3.6 this was done leading to a stray field distribution with flat zero line and matching peaks.

After numerous cycles of preparation and subsequent sputtering of the sample some amount of ferromagnetic dirt was found on the sample holder. This led to a magnetic background not originating from the measured film. It turned out, that for two films of the same thickness the derived magnetization was the same no matter if they were measured with a clean or a slightly contaminated sample holder. In the case of an unstructured background the two peaks unambiguously originate from the film. Therefore, by adjusting the peaks one can still derive a reliable magnetization value no matter if the zero line is flat or not. This is not valid if the background of the sample holder exhibits some peak-like features which then can not be distinguished from the ones originating from the sample. However, one should take precautions not to contaminate the sample holder, e.g. to sputter with the help of a shutter made from non-magnetic material (e.g. Cu) which covers the whole sample holder except the crystal itself.

#### Determination of the number of atoms

As mentioned above, one needs an accurate determination of the number of atoms of the measured film. The determination of the thickness of the film is done by a water-cooled quartz crystal microbalance. Usually, the uncertainty of the

absolute thickness determination is assumed to be about 10%. Since the mea-

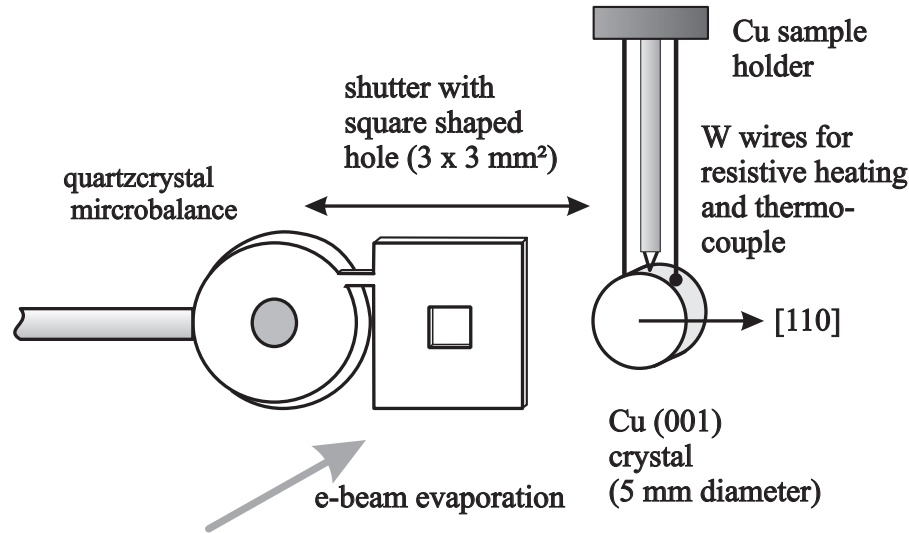


**Figure 3.11:** Sketch of the shutter attached to the quartz crystal microbalance to yield a well defined geometry of the evaporated film. It also avoids contaminating the sample holder with ferromagnetic material.

surements are performed thickness-dependent one can test the reliability of the thickness determination at the thick film limit. The derived values are expected to be bulk-like. A shutter with a square-shaped hole of well-defined geometry is attached directly to the quartz-balance as sketched in Fig. 3.11. Note, that during evaporation on the quartz-balance the crystal is retracted in a way that it is still covered by the shutter. The hole was made by an electrical erosion technique with an accuracy of 0.01 mm. The size is  $3.00 \times 3.00 \text{ mm}^2$ . Before and after preparation of the film the evaporation rate is monitored by the quartz-balance. In between the film is evaporated through the hole of the shutter. The Cu(001) crystal is kept in a distance of  $\sim 0.1$  to 0.5 mm right behind the aperture. The evaporant is about 15 cm away. Therefore, the film is of the same size as the hole of the shutter. The shutter is moved perpendicular to the direction of evaporation. Consequently, the distances quartz-balance/evaporant and shutter/evaporant are equal. The so-called “tooling factor” which corrects with respect to geometrical considerations for the thickness determination is 1. The used commercial evaporator [89] has a spot profile of 1.5 cm diameter in a distance of 15 cm and a homogeneity of at least 99%. This was confirmed previously by using x-ray absorption edge-jump analysis with a relative error of 1/50 of a ML, see [90]. The film is therefore homogeneous over its total size and the number of atoms can be derived by the film thickness and its area.

### Determination of the distance $h$

Another input parameter is the distance between the sample and the SQUID plane  $h$  as indicated in Fig. 3.7. According to eq. (3.4) the measured stray field scales like  $1/h^3$ . This was experimentally confirmed by measuring a thick Co film

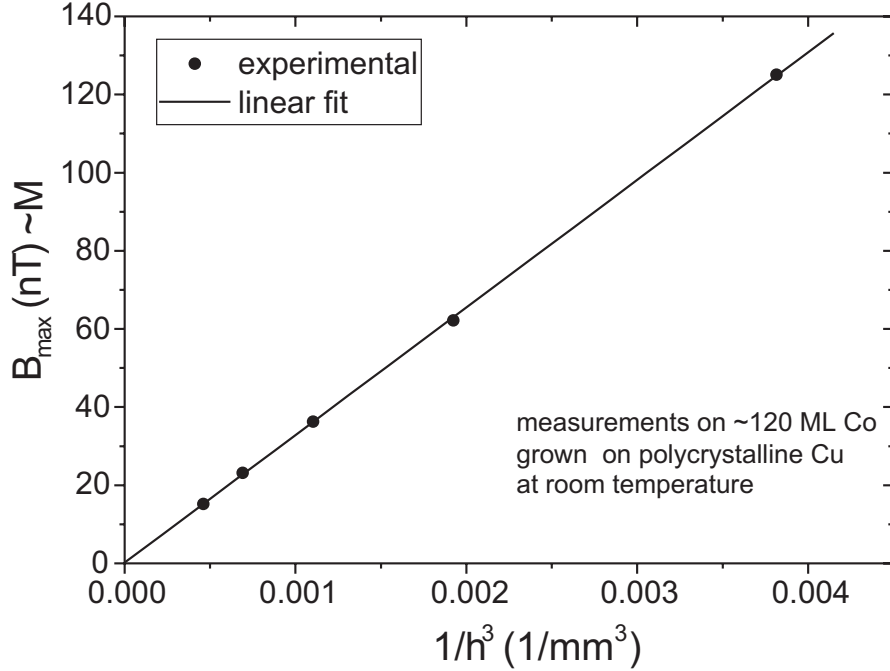


**Figure 3.12:** Experimental test of the  $1/h^3$  dependence of the maxima of the measured stray field.

on polycrystalline Cu at various distances. The outcome of this test measurement in the early stage of the experiment is shown in Fig. 3.12. The data (circles) follow nicely the expected  $h^{-3}$  behavior (line).

The strong dependence of the measured signal on the distance implies that one should be able to determine  $h$  within 0.1 mm of accuracy if the magnetization ought to be measured with an error <10%. It turned out, that it is impossible to determine  $h$  directly since the SQUID is kept inside the dewar (*ex situ*) while the sample is inside the  $\mu$ -metal screening (*in situ*). Therefore, an indirect technique is applied to extract  $h$  from the measured data. As it can be seen from eq. (3.4) the shape of the stray field of an in-plane magnetized sample depends on the geometry including the distance  $h$  while the amplitude of the field is governed by the film thickness  $d$  and the magnetization  $M$ . In Fig. 3.8 one can follow the change in the position of the maxima of the stray field with respect to the distance  $h$ . This allows to fit various calculated stray field distributions for different  $h$  which were scaled to the same amplitude (see Fig. 3.13). Then, the lowest least mean

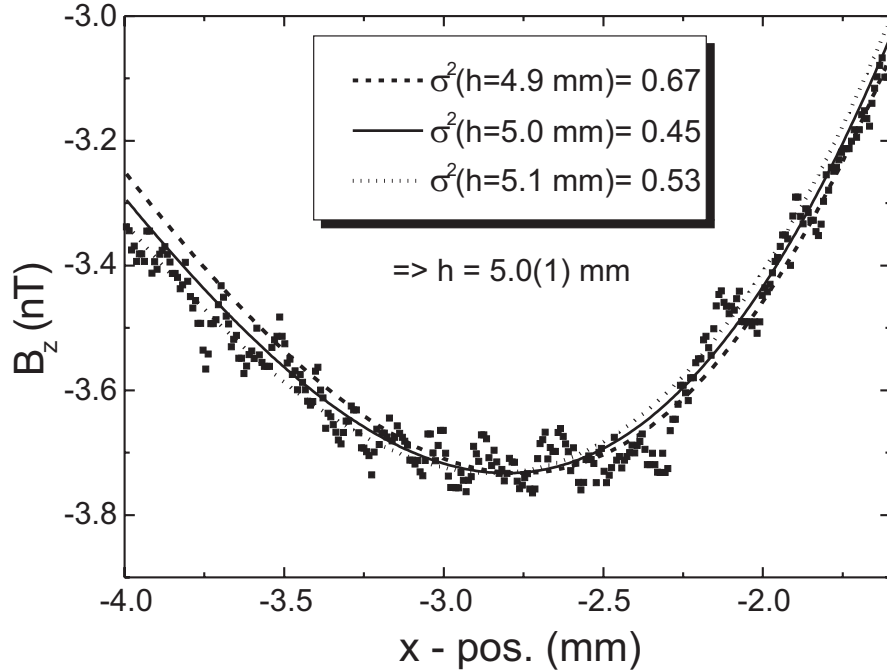


**Figure 3.13:** Enlarged negative maximum of the stray field distribution shown in Fig. 3.6. The three lines correspond to a fit using eq. (3.4) with different values for the distance  $h$  and  $M$  to match the peak height. The resulting uncertainty in  $h$  is 1/10 mm corresponding to an error of 60 kA/m in  $M$ .

square deviation  $\sigma^2$  is calculated yielding the best value for  $h$ . From Fig. 3.13 the error of this method can be discussed as well. The dotted line corresponding to  $h = 4.9$  mm fits the data well only on the right side of the peak while the left part clearly deviates. In the case of  $h = 5.1$  mm (dotted line) it is vice-versa. Therefore the error is supposed to be 0.1 mm leading to  $h = 5.0(1)$  mm. Since the amplitude depends on the distance as well, this implies an uncertainty in the determination of the magnetization of 60 kA/m corresponding to  $\sim 4\%$  for Co or Fe (10% for Ni since the moment is by a factor of 3 smaller, see Table 1.1).

It should be stated that there is an optimum range of choosing  $h$  determined by two competing interests: the sensitivity and the accuracy. To end up with a sensitive setup it can be seen from Fig. 3.8 that with decreasing  $h$  the signal increases rapidly and, therefore, can be detected more easily. On the other hand, the desired accuracy is determined by the uncertainty of  $h$ . The above-mentioned procedure is limited to about 0.1 mm. If the distance is reduced to 3 mm then this error would result in an uncertainty in the determination of the magnetization of about 150 kA/m as the signal scales like  $1/h^3$ . At larger distances  $h$  the uncertainty in  $M$  decreases as well as the sensitivity. Having a distance  $h$  in the range of 4 to 6 mm the sensitivity is still in the submonolayer regime and the

uncertainty is below  $\sim 5\%$ . Consequently, a distance between SQUID and sample ought to be chosen in that range to end up with both, sufficient accuracy and sensitivity.

### 3.4 Sample preparation

The magnetometer is mounted at a standard UHV chamber with turbo-pump, ion-getter-pump, and titanium sublimation pump (TSP). A one day's baking at 450 K is performed to remove adsorbates like  $\text{H}_2\text{O}$  from the chamber walls. The base pressure of the UHV chamber is  $\leq 2 \cdot 10^{-10}$  mbar at room temperature.

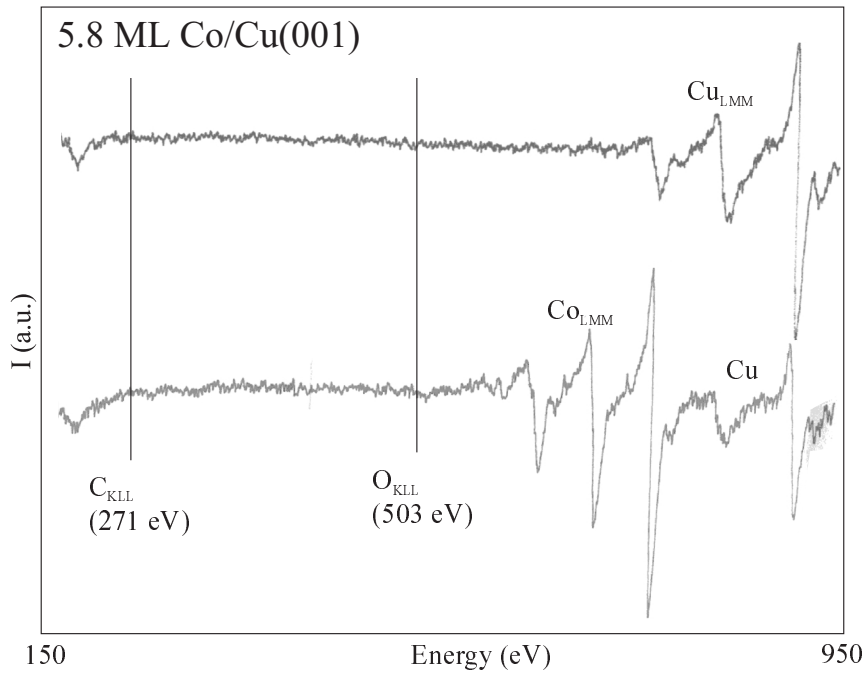


**Figure 3.14:** Auger electron spectra for a clean Cu(001) crystal (top) and after evaporation of a 5.8 ML Co film (bottom). The energies for O and C are indicated confirming that the crystal and the film are not contaminated significantly by O and C (less than  $\sim 1/30$  ML).

The Cu(001) single crystal is cleaned by numerous sputtering and annealing cycles. The sputtering is done with  $\text{Ar}^+$ -ions at 1 or 3 kV accelerating voltage. During sputtering the major part of the sample holder is covered by a Cu shutter to avoid contamination. The annealing temperature is 870 K, which is kept for  $\sim 5$  min to obtain a clean and flat surface [91]. The structural quality of the surface is confirmed by a sharp low-energy electron diffraction (LEED) pattern. The cleanliness of the surface is monitored by Auger electron spectroscopy (AES)

confirming a contamination with carbon, sulfur or oxygen below  $1/30^{th}$  of a ML (Fig. 3.14). The films are evaporated by electron bombardment heating of a high purity rod with the help of a commercial, water-cooled evaporator [89] with a flux-monitor to stabilize the evaporation rate. During evaporation of the metal films the pressure did not exceed  $5 \cdot 10^{-10}$  mbar (the evaporation rate is about 0.1 nm/min). Before and after evaporation the evaporation rate is monitored with the help of a water-cooled quartz crystal microbalance. The thickness determination is done via the evaporation time and the average of the rates before and after evaporation. In all cases the evaporation rate was constant over the whole evaporation time.

Right after preparation the films were magnetically saturated by a pulse driven electromagnet<sup>6</sup> with fields up to 40 kA/m. These pulses are sufficient to overcome the coercive fields of in-plane magnetized Co and Ni films in the ultrathin limit [92]. The field is applied along the in-plane [110] direction which is known to be the easy axis of the magnetization of Co/Cu(001) [93]. The sample can be measured about 5 minutes after evaporation. This minimizes contamination due to residual gases. Subsequently (5 to 10 more minutes), Cu can be evaporated from a Mo-crucible to check the influence of capping layers on the magnetization.

---

<sup>6</sup>A horse-shoe type of electromagnet is chosen which is – in principle – suitable for MOKE measurements as well.

# Chapter 4

## The System Co/Cu(001)

The first results using the new setup of the UHV-SQUID magnetometer were accomplished by thickness- and temperature-dependent measurements of Co ultrathin films grown on Cu(001). They provide a complete set of ground state magnetic moments which are separated into spin and orbital contributions using the results of former XMCD measurements. The effect of subsequent Cu capping of the films permits separating surface and interface magnetic moments. Results for films thinner than 2 ML are presented as well and they are discussed with respect to structural properties and annealing effects. With support of scanning tunneling microscopy (STM) experiments the effect of soft thermal treatment on the magnetic behavior is illustrated.

### 4.1 Structural and magnetic properties of Co/Cu(001)

This introductory section discusses the relevant structural and magnetic properties of the system Co/Cu(001). Co ultrathin films are of great fundamental and practical interest. Co exhibits a relatively high Curie temperature (1388 K) [9] which makes this material promising for room temperature applications even in reduced dimensions. Bulk Co crystallizes in hcp structure and shows a large uniaxial anisotropy (magnetic anisotropy energy (MAE) =  $65 \mu\text{eV}/\text{atom}$  [10])<sup>1</sup>. Furthermore, bulk Co atoms carry a relatively large magnetic moment of  $1.73 \mu_B/\text{atom}$  [10]. There are many applications of ferromagnetic materials of reduced dimensions containing Co: Layered systems of ultrathin Co films show interesting coupling effects such as giant magneto-resistance (GMR), e.g. [94], which can be used in the sense of a “spin valve” [95]. Granular materials containing Co may be used as high-density recording media as well [96]. These applications illustrate the motivation to study low dimensional Co systems. Co/Cu(001) with film

---

<sup>1</sup>The MAE is almost by a factor of 30 larger than for bulk Ni or Fe [10].

thicknesses between 2 and 10 ML grown at room temperature were often chosen as prototype systems to study magnetic properties, e.g. see [60, 93, 97, 98].

The following discussion is restricted to the pseudomorphic growth of Co on a Cu(001) single crystal. The observed growth mode is linked with a sudden change in the Curie temperature  $T_C$ . Tables containing a collection of the theoretical and experimental findings of magnetic moments for the system Co/Cu(001) are given as well.

### 4.1.1 Growth of Co on Cu(001)

Above 2 ML Co/Cu(001) grows in an excellent layer-by-layer mode [99]. They are in a face-centered-cubic phase with small tetragonal distortion (fct) due to the pseudomorphical growth [100]. Below 2 ML controversial results can be found in the literature. An early STM work reported the formation of double layer islands [101]. More recent work showed that this effect is present, but less pronounced [102, 103]. Moreover, Carbon-Oxide titration experiments [104] and several recent STM works with corresponding calculations [102, 105, 106, 107] demonstrated limited intermixing at the Co/Cu interface.

In Fig. 4.1 STM pictures of room temperature grown Co films on Cu(001) of various thicknesses below 2 ML are shown. (a) corresponds to a mass equivalent of 0.6 ML. The substrate (dark gray) the first ML islands (light gray), and bilayer islands (white tones) can be seen. The islands of the first ML have two sizes indicating a bimodal type of growth [102, 105]. The smaller ones (of about 1 nm) are believed to consist mainly of Co adatoms trapped by other Co atoms that are embedded inside the topmost ML of the substrate [102, 105, 107]. The larger islands consist of Co adatoms and Cu atoms of the topmost substrate layer which exchanged their positions with Co ones. Bilayer islands represent an unusual high percentage of coverage ( $\sim 20\%$ ), inconsistent with a perfect layer-by-layer growth. At a coverage of 1.45 ML (Fig. 4.1, (b)) one may see an almost complete first ML (gray), a negligible view of the substrate (dark) and islands of the second ML (light). This supports the findings of [102, 103] and excludes the existence of isolated double layer islands at such coverages reported in [101]. At a coverage of 1.7 ML (Fig. 4.1, (c)) the coalescence of the islands of the second ML takes place. The double layer islands represent now less than 5% of the coverage above the first ML, therefore the growth mode is almost ideal layer-by-layer. Fig. 4.1 (d) shows the surface of 2.03 ML Co/Cu(001) which is a representative picture for an excellent layer-by-layer growth mode according to the existing literature.

### 4.1.2 Sudden increase of $T_C$

The above discussed growth mode of Co/Cu(001) below 2 ML is linked to a change in the magnetic properties of the film. The coalescence sets in at a critical thickness  $d_c$  of about 1.6 to 1.8 ML. In that thickness region an abrupt change

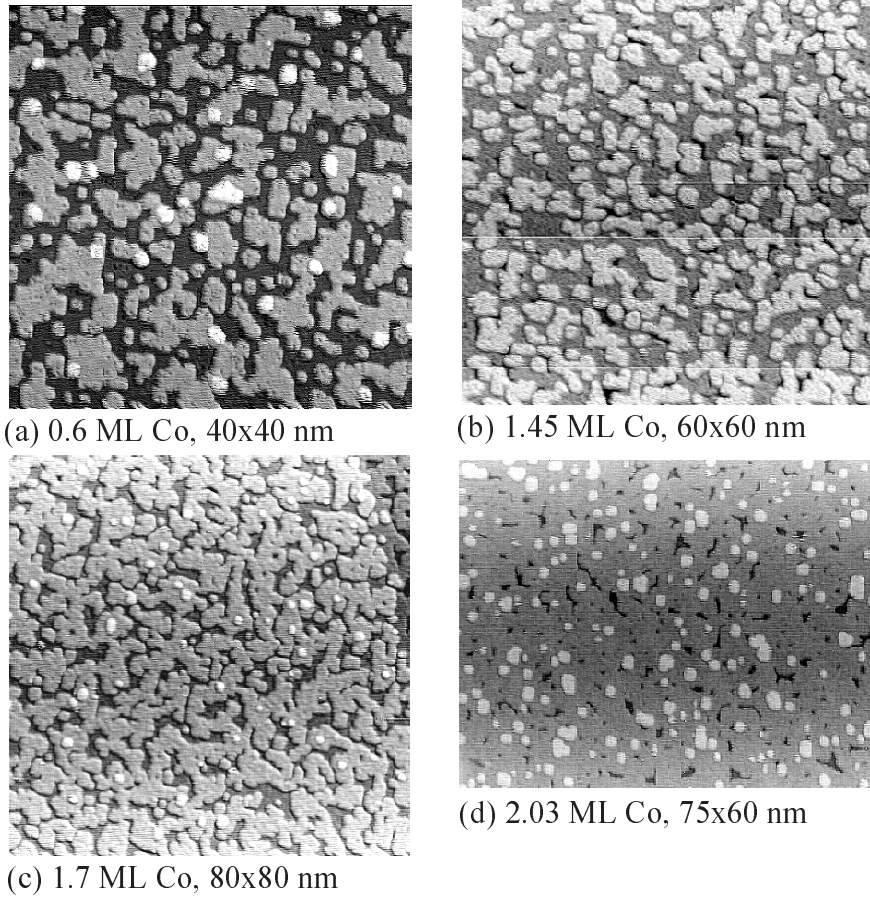


**Figure 4.1:** STM pictures at the initial stage of growth of Co on Cu(001). Below 1.7 ML (a, b) a non-perfect layer-by-layer growth is observed. The coalescence occurs around 1.7 ML (c). Above 2 ML the films are atomically flat (d) and grow in an ideal layer-by-layer mode.

of the Curie temperature  $T_C$  by about 100 K is observed (“ $T_C$ -jump”) [108]. In earlier works ferromagnetic order has been excluded below  $d_c$  [98] whereas later on ferromagnetic order was observed, e.g. [60, 108]. Figure 4.2 summarizes  $T_C$  of Co/Cu(001) as a function of the film thickness measured by various experimental methods. It can be seen that right above  $d_c$  the  $T_C$  exceeds 300 K which may serve as an explanation why some authors conclude that  $d_c$  can be identified with the onset of ferromagnetism at room temperature [98]. The presence of a  $T_C$ -jump causes certain requirements when performing magnetometric measurements at the ultrathin film limit. Room temperature measurements are restricted to film thicknesses above 2 ML. Measurements below  $d_c$  need cooling facilities to reach low temperatures to assure that the measurement takes place below  $T_C$ . The values of  $T_C$  shown in Fig. 4.2 serve to determine the reduced temperature

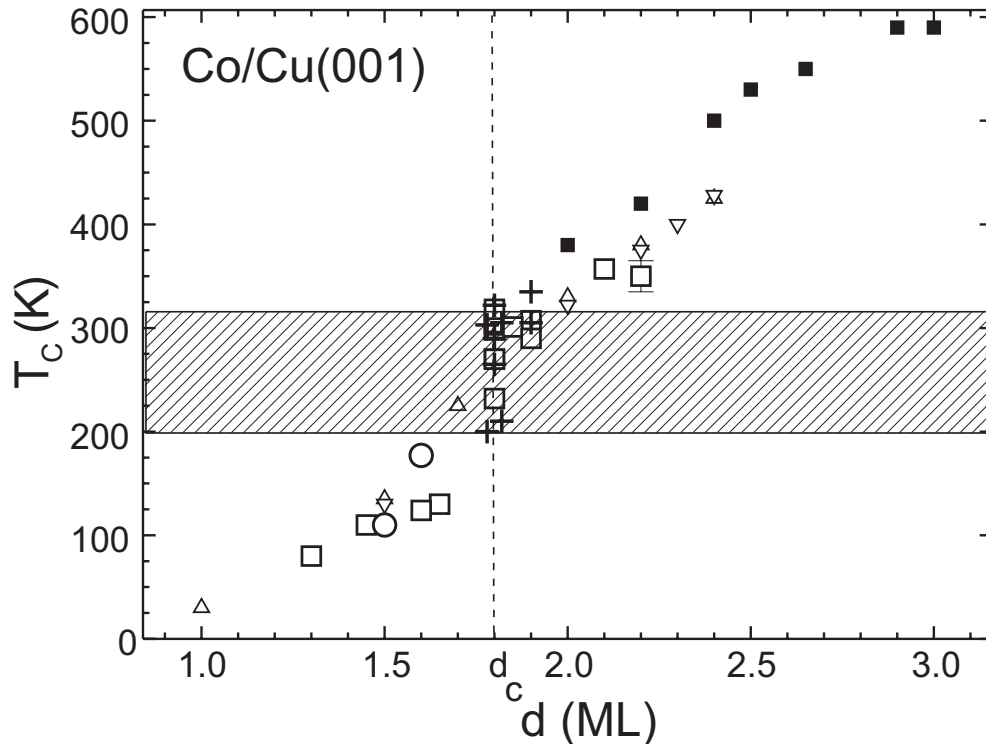


**Figure 4.2:** Thickness dependence of  $T_C$  for Co on Cu(001). Open symbols are experimental data which were derived using various techniques [108]. The full squares are theoretical values taken from [109].

$t = T/T_C$  for the measurements with the UHV-SQUID magnetometer. Above 2.5 ML theoretical values from [109] are used (full squares) since a measurement of  $T_C$  is not possible. This is due to the fact that above 450 K considerable intermixing between Co and Cu occurs.

Moreover, in [108] it was discussed that  $T_C$  at  $d_c$  was time and temperature dependent, i.e. metastable. Due to the island-type growth below  $d_c$  one expects metastable behavior below that thickness as well. Since the novel magnetometer offers submonolayer sensitivity as well as low temperatures, it is possible to study the magnetic properties of Co films not only above  $d_c$  to derive a complete set of magnetic moments (Section 4.3) but also below  $d_c$  (Section 4.5).

### 4.1.3 Magnetic moments for Co/Cu(001) from literature

Considerable theoretical and experimental work concerning the magnetic moments of Co systems can be found in the literature. Tables 4.1 and 4.2 show the layer-resolved theoretical expectations for Co/Cu(001), fcc, and hcp Co.

It is common sense that the surface magnetic moments of Co are enhanced,

Group	System	$\mu_{tot}/\text{atom}$	$\mu_S/\text{atom}$	$\mu_L/\text{atom}$	Ref.
Uppsala	hcp Co bulk	$1.67\mu_B$	$1.58\mu_B$	$0.09\mu_B$	[110]
	surface	$1.86\mu_B$	$1.75\mu_B$	$0.11\mu_B$	
	hcp Co bulk	$1.753\mu_B$	$1.63\mu_B$	$0.123\mu_B$	[27]
	surface	$1.948\mu_B$	$1.79\mu_B$	$0.158\mu_B$	
	1 ML Co/Cu(001)	$2.111\mu_B$	$1.85\mu_B$	$0.261\mu_B$	[27]
	free ML Co	$2.398\mu_B$	$2.06\mu_B$	$0.338\mu_B$	[27]
FHI	Co/Cu(001) 1 ML		$1.711\mu_B$		[106]
	2 ML		$1.589\mu_B$		
	Cu/Co/Cu(001) 1 ML		$1.445\mu_B$		[106]
	2 ML		$1.379\mu_B$		
Vienna	2 ML Co/Cu(001) surface	$1.813\mu_B$			[111]
	interface	$1.652\mu_B$			
	15 ML Co/Cu(001) surface	$1.850\mu_B$			[26]
	center (oscill.)	$1.72\mu_B$			
	interface	$1.660\mu_B$			
	2 ML Co/Cu(001)	$1.74\mu_B$			[112]
CNRS	hcp Co surface	$1.815\mu_B$	$1.69\mu_B$	$0.125\mu_B$	[113]

**Table 4.1:** Summary of various theoretical calculations dealing with Co magnetic moments (Part I).

no matter if in fcc or hcp structure as can be seen in Table 4.1. The values vary by about  $0.1\mu_B/\text{atom}$  which seems to be linked to the used method. Concerning the results of the Vienna group one should note that the enhancement at the surface and the reduction at the interface would cancel out for both systems (15 and 2 ML) upon performing layer-averaged magnetometry. In other words: no enhanced magnetic moment for thin films is predicted in that work. The values derived by the Uppsala group [27] include the effect of the orbital polarization in the calculation. If this effect is “switched off”, the orbital moment is decreased by a factor of about 1.5 to 2 [27]. This is the reason that almost all other studies shown in Tables 4.1 and 4.2 report smaller values for  $\mu_L$ . Comparing with experiments [46, 47, 49] it is of importance to include the orbital polarization to end up with a satisfactory agreement.

Table 4.2 summarizes work done by Freeman *et al.* The first five values refer

System	$\mu_{tot}/\text{atom}$	$\mu_S/\text{atom}$	$\mu_L/\text{atom}$	Ref.
1 ML Co/Cu(001)		$1.79\mu_B$		[114]
hcp Co		$1.76\mu_B$		[115]
surface		$1.64\mu_B$		[115]
center		$1.89\mu_B$		[15]
free ML				
fcc Co(001)		$1.86\mu_B$		[115]
surface		$1.65\mu_B$		
center				
1 ML Co/Cu(001)	$1.901\mu_B$	$1.785\mu_B$	$0.116\mu_B$	[116]
	$1.891\mu_B$	$1.772\mu_B$	$0.094\mu_B$	[117]
1 ML Co/Cu				[118]
(001)	$2.06\mu_B$			
(110)	$2.20\mu_B$			
(111)	$1.83\mu_B$			
free Co(001)				[119]
5 ML	$1.75\mu_B$			
3 ML	$1.81\mu_B$			
1 ML	$2.07\mu_B$			
1 ML Co in Cu(001) lattice	$2.356\mu_B$	$2.12\mu_B$	$0.236\mu_B$	[28]
1 ML Co/Cu(001)	$2.038\mu_B$	$1.92\mu_B$	$0.118\mu_B$	[120]
+ 1 ML Cu cap	$1.857\mu_B$	$1.74\mu_B$	$0.117\mu_B$	

**Table 4.2:** Summary of various theoretical calculations dealing with Co magnetic moments (Part II). All results are from Freeman's group.

to older results which do not include the orbital moment. However, it can be seen that the difference between hcp and fcc Co bulk is quite small ( $\sim 0.02\mu_B/\text{atom}$ ). In [118] the influence of the surface orientation on the magnetic surface moment is studied. This work includes the effect of orbital polarization as well. The (110) surface (for the fcc lattice this is the most open one) exhibits the largest increase of the moment, the closed packed one, (111), the lowest moment. This can easily be understood in terms of coordination number arguments [16] and the next-neighbor distance. The largest enhancement is found for the free standing monolayer in a fcc (001) structure matching the Cu lattice [28] in agreement with the results of the Uppsala group [27]. 1 ML Co on Cu(001) exhibits a smaller value [120]. The surface moment of a Co film grown on Cu(001) should be placed in between these two values and, accordingly, it should be larger than the value for a fcc bulk Co surface.

Contrary to theory, experiments can not provide such a large amount of relevant numbers. On the one hand, this is due to the simple fact, that one can not prepare ideal systems like free standing monolayers. On the other hand, when studying magnetic properties for ideal-like layers on a substrate one faces experimental difficulties concerning cleanness, sensitivity, and cooling capabilities.

System	$\mu_{tot}/\text{atom}$	Ref.
Cu/Co/Cu(001) 10 ML	$1.8(25)\mu_B$ $T = 300 \text{ K}$	[121]
2 ML	$2.1(3)\mu_B$ 10 - 450 K	[122]
Ag/Co/Ag(001) 2 ML	$1.8 - 2.1\mu_B$ 4 - 300 K	[123]
Pd/Co/Pd(111) 12 ML	$1.84(1.73)\mu_B$	[124]
Cu/FeNi/Cu/Co/Cu/FeNi/Cu/Si(001) 23 ML	$1.71(8)\mu_B$	[125]

**Table 4.3:** Summary of experimental results for magnetic moments of Co using polarized neutron diffraction techniques (PND/PNR).

Table 4.3 shows that there exists considerable work on sandwiched Co systems. However, the authors report a magnetization of a 2 ML Co film which is practically temperature independent in the range of 300 to 450 K [122, 123]. This is in contradiction to other experimental findings where the Curie temperature for comparable systems is found to be around room temperature, e.g. [97, 108]. In the case of the Pd sandwich it should be added that the authors conclude that a distinction between an enhanced Co moment ( $1.84\mu_B$ ) and a bulk-like Co moment ( $1.73\mu_B$ ) combined with an interface polarization of the Pd is not possible [124]. The value reported in [125] fits well the existing theoretical predictions for bulk-like films.

Table 4.4 summarizes the outcome of XMCD measurements for three cases of Co. While the results for hcp Co in [46] are taken as a proof for the validity of the sum rule analysis, the two other works relied on a calibration of the experimental parameters with the help of a bulk-like reference sample. In that sense they can be called “relative” measurements. The Co sandwiched between Au shows a constant spin moment from 4 to 11 ML which is bulk-like [49]. The orbital moment is found to increase considerably (almost by a factor of 2) and extrapolation to 1 ML reveals a value which is even larger ( $0.36\mu_B$ ) than the calculated one in [27] ( $0.261\mu_B$ ). The work on 2.1 ML Co/Cu(001) reveals an enhancement of the magnetic moment [47] and a drastic reduction of 30% upon Cu capping [62].

System	$\mu_S/\text{atom}$	$\mu_L/\text{atom}$	Ref.
35 ML Co(hcp)	$1.55\mu_B$	$0.153\mu_B$	[46]
Au/Co/Au(111)			[49]
1 ML (extrapol.)		$0.36\mu_B$	
4 ML	$1.64\mu_B$	$0.224\mu_B$	
11 ML	$1.64\mu_B$	$0.14\mu_B$	
2.1 ML Co/Cu(001)	$1.77(1)\mu_B$	$0.24(5)\mu_B$	[47]
+ Cu cap	$1.29(1)\mu_B$	$0.12(5)\mu_B$	[62]

**Table 4.4:** Summary of experimental results for magnetic moments of Co using XMCD.

## 4.2 Thickness dependence of the magnetization

The thickness dependence of the magnetization of Co/Cu(001) between 17 and 2 ML was measured with the new magnetometer as a function of the temperature. The magnetometer measures the real ground-state properties since the stray field is detected and no electronic transitions occur. The magnetization is derived in an absolute calibrated way and it can be shown that it is increased reducing the films thickness. This results in complete set of magnetic moments measured as a function of the film thickness which provides valuable new input to the field of thin film magnetism.

### 4.2.1 $M$ for the thick film limit

In many types of magnetometry thick films ( $\sim 20-70$  ML) serve as reference – e.g. XMCD, MOKE – to calibrate parameters of the measurements [47, 48, 49, 55]. This procedure implies that thick films behave like bulk samples. But absolute methods like the AGM crosscheck their calibration by a bulk-like reference sample as well [68]. However, *a priori* it is not clear that pseudomorphically grown films have the same properties as the bulk. Especially in the case of Co where the bulk is hexagonal (hcp), changes in the magnetic moment occur upon growing it in fcc structure. It is known that bulk Co has a magnetic moment of  $1.73\mu_B/\text{atom}$  when it is hcp whereas the fcc phase has a moment of  $1.75\mu_B/\text{atom}$  [10]. Taking into account a finite experimental accuracy the difference of  $0.02\mu_B/\text{atom}$  is not significant. Therefore, the calibration with a bulk-like sample should be reliable in the case of Co.

Figure 4.3 shows the stray field distribution for an 8.6 ML film at room temperature. The fit is performed by using the area of the shutter for the film geometry ( $3 \times 3 \text{ mm}^2$ ), the thickness determined by the quartz crystal microbalance, and the calibrating factor determined by using a coil and applying Biot Savart's law (see Chapter 3). The distance is fitted as described in Chapter 3 by adjusting the

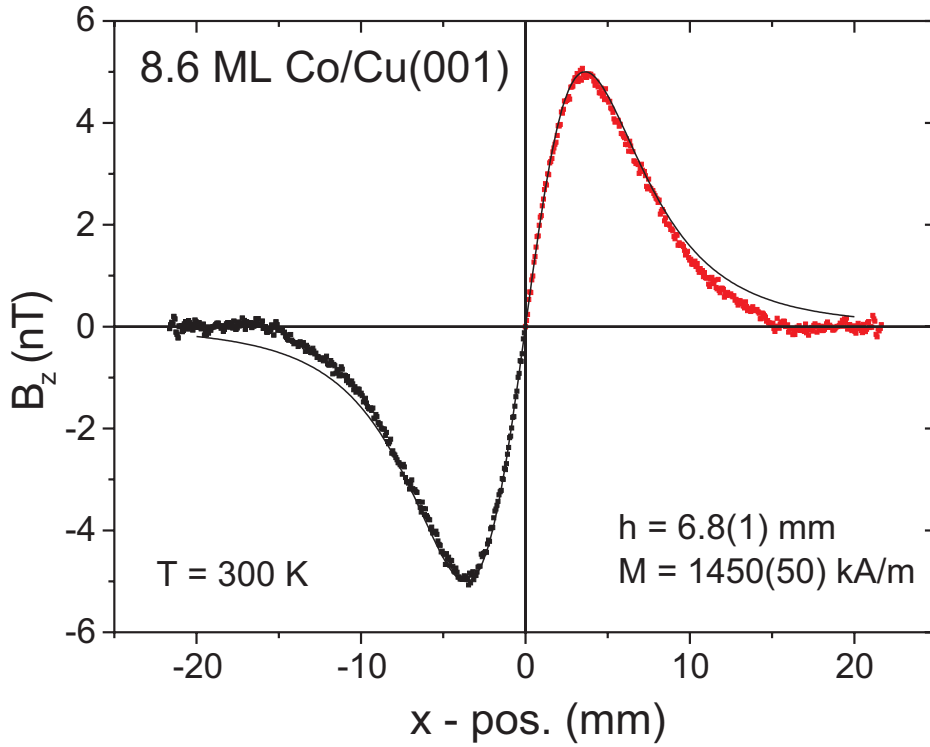


**Figure 4.3:** Measured stray field of a bulk-like Co film at room temperature. The fitted value for the magnetization coincides with the bulk value of [10] (1445 kA/m). Deviations from the fit at  $x$  - pos.  $\geq 11$  mm are due to the fact that the sample starts to move outside the shielding. The measured field at positions  $\geq 17$  mm is a true zero line since the sample is completely outside the shielding.

maxima of the stray field yielding  $h = 6.8(1)$  mm. The amplitude of the signal is then adjusted by fitting the magnetization yielding 1450(50) kA/m. The error is mainly due to the uncertainty in determining  $h$ . This perfectly agrees with the literature value of 1447 kA/m for hcp bulk Co at room temperature [10]. It should be stated again that no adjustable parameter is used. In turn, this proves the reliability of the thickness determination and the calibration of the SQUID. For two other films with thickness 11.6 and 16.5 ML the magnetization at 300 K is found to be 1445 kA/m and 1450 kA/m respectively. The uncertainty of 50 kA/m corresponds to 3.5% only. This is a remarkably small value for an absolute determination of  $M$ . The deviation by 1.1% from the bulk value of fcc Co at room temperature is within the errorbar. Indeed, Co films in this thickness regime are within 4% magnetized like the bulk, no matter if one refers to the fcc or the hcp bulk value. In the following we will always refer to the hcp Co bulk value.

### 4.2.2 The effect of the measuring temperature

During setting up the UHV-SQUID magnetometer Co films of various thicknesses between 2 and 17 ML were measured using different types of sample holders and evaporators. Although these were the first experiments to test the new magnetometer only three out of 30 measured films could not be analyzed in a proper way; one of them due to an instable evaporation rate which made a thickness determination impossible. This clearly demonstrates the reliability and reproducibility of the data measured with the novel UHV-SQUID magnetometer. Apart from

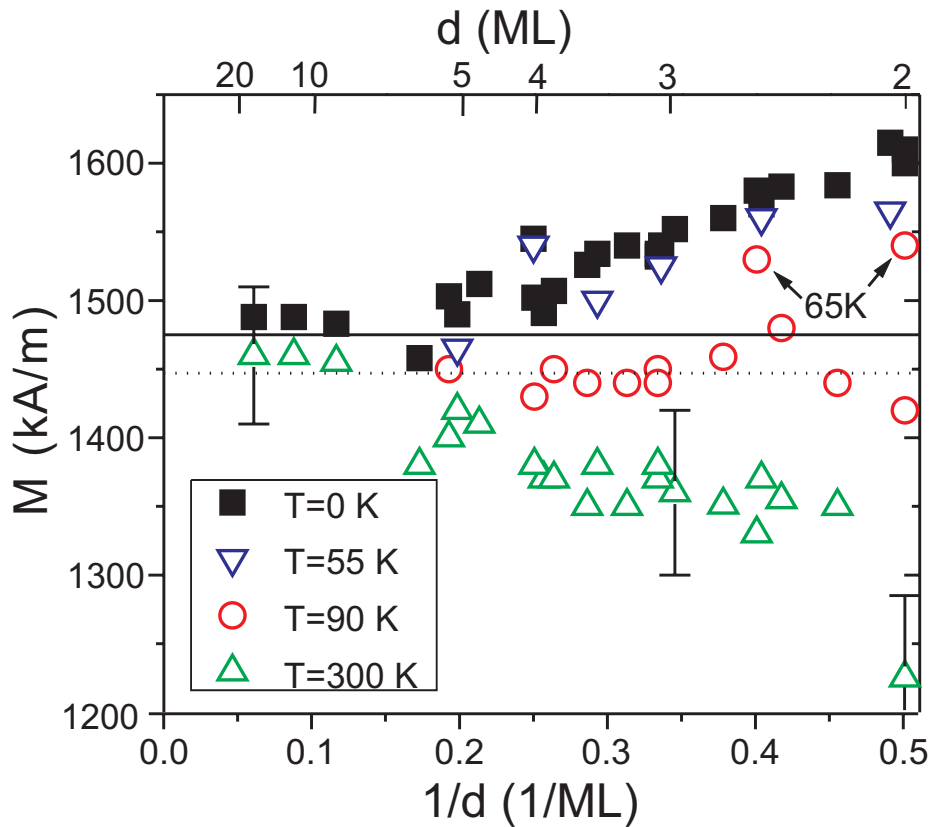


**Figure 4.4:** The magnetization of Co/Cu(001) vs the inverse film thickness at different temperatures [126]. The bulk values for 4 K (full line) and 300 K (dashed line) are indicated [10].

the above mentioned three films all measurements are plotted together vs the inverse film thickness in Fig. 4.4. The measurements were performed at various temperatures. The room temperature data (open up triangles) are discussed first. The films with thicknesses down to 2 ML exhibit a thickness dependent reduced magnetization down to 1225 kA/m. At a first glance one might think that the reduction is due to a reduced magnetization at the interface, e.g. due to strong

intermixing. In [127, 128] a thickness dependent saturation magnetization was reported based on room temperature measurements. This conclusion neglects that  $T_C$  of the thin films is reduced due to the finite-size effect, see Section 1.3 and Fig. 4.2. Therefore the reduced temperature  $t = T/T_C$  is not the same for all the films, i.e. one must not compare the magnetization of the films at 300 K. One can easily see from the data at 90 K (open circles) that there is no reduced magnetization at low coverages. In that case one might conclude that surface and interface magnetization are equal or that the enhancement at the surface and the reduction at the interface cancel out each other as predicted in [26], which is incorrect as well. It is at least possible to extrapolate the measured magnetization

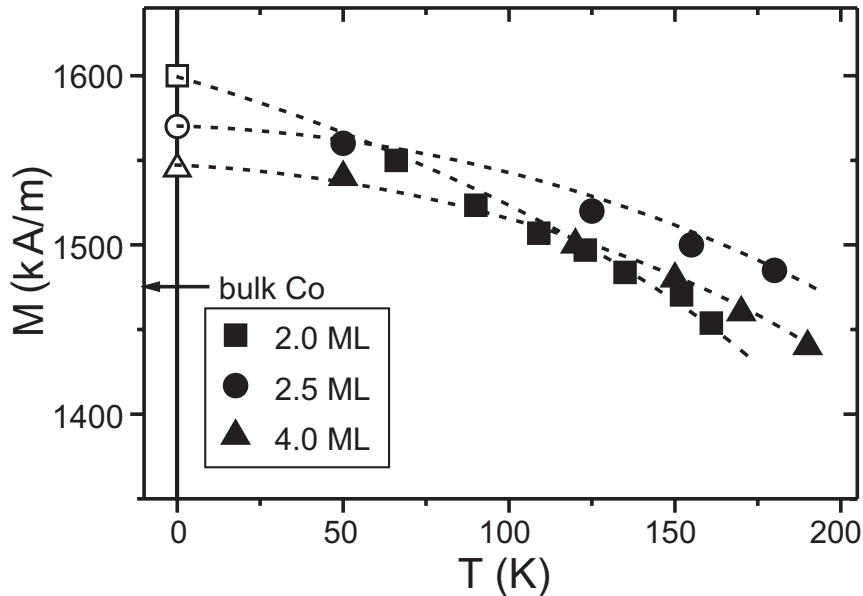


**Figure 4.5:** Temperature dependent measurements for three different films to determine  $M(T = 0)$  via extrapolation using the spin wave law.

in this temperature regime to  $T = 0$  K as it is done e.g. in [18]. This implies the knowledge of  $T_C$  and the exact functional behavior of  $M(T)$ . Uncertainties due to that can be omitted by measuring at even lower temperatures. In Fig. 4.4 results for 55 K are shown which were measured when the lHe cooling was fully established in the chamber.  $M$  is clearly enhanced at the thin limit. Extrapolation to  $T = 0$  K can be done by measuring the temperature dependence of  $M$  as shown in Fig. 4.5. The correction compared to the 55 K measurement is  $\leq 2\%$ , no matter which functional behavior of  $M(T)$  close to  $T = 0$  K is chosen, see Fig. 1.4. The full squares represent all extrapolated values for the magnetization at  $T = 0$  K which represent the true ground-state magnetic properties of the system. For some thicknesses (e.g. at 2 ML) there exist two or three measurements at different low temperatures (using either  $\text{LN}_2$  or lHe for cooling). The

values at  $T = 0$  K were derived by two different methods: either extrapolating from temperature dependent measurements, or by a single low (e.g. 90 K) temperature measurement and subsequent extrapolation with the help of the spin wave law (taking  $T_C$  from Fig. 4.2). The two methods lead to almost the same  $M(T = 0)$  value. Therefore it is justified to provide values at  $T = 0$  K even for films measured without a complete temperature dependent set of data. The magnetization values at  $T = 0$  K nicely follow a linear behavior with respect to the inverse film thickness. The observed enhancement at 2 ML is 10(1)% yielding a magnetization  $M = 1600(60)$  kA/m [126].

The values of  $M(T = 0)$  can be translated into a magnetic moment per atom which is only possible if the saturation magnetization  $M_{sat}$  is measured. This is assured by saturating the films once by an external field pulse of  $\sim 40$  kA/m. resulting in a single-domain state of the film. In the case of in-plane magnetized ultrathin films the single domain state is known to be the thermodynamical ground state [93, 129]. Therefore the hysteresis loop is square-shaped and the remanent magnetization equals the saturation value.

### 4.3 Deconvolution of spin ( $\mu_S$ ) and orbital ( $\mu_L$ ) contribution

The magnetization at  $T = 0$  K is translated into the total magnetic moment ( $\mu_{tot}$ ) per atom. This demands the knowledge of the number of ferromagnetic atoms. This is a relatively easy topic dealing with a single layer of ferromagnetic material with an underlying non-magnetic substrate. It is known that the Cu substrate is polarized by at most  $0.05\mu_B/\text{atom}$  [48] which will be neglected in the following. In case of multilayers with strongly polarized interfaces, e.g. Ni/Pt [59] or Fe/Cr [67], it is not trivial to determine the correct number of atoms which contribute to the total magnetization. These measurements require an element specific knowledge of the magnetization of each constituent which has been done e.g. in [59]. In case of the simple Co/Cu(001) system there are no complications in translating  $M_{sat}(T = 0)$  into real ground state magnetic moments. The outcome will be discussed in the following section.

#### 4.3.1 $M(T = 0)$ and magnetic moments

The results of  $M(T = 0)$  represented by the full squares in Fig. 4.4 can be converted into magnetic moment per atom by a simple scaling factor. The number of atoms per unit cell for fcc Co is 2, the lattice constant is the one of Cu (0.361 nm). This yields the values for  $\mu_{tot}$  denoted by the solid squares in Fig. 4.6. The magnetic moment at the thick film limit,  $1.73(8)\mu_B/\text{atom}$ , equals within the error the bulk value of  $1.73\mu_B/\text{atom}$  [10]. The difference compared to earlier works is that the value at the thick film limit is measured and not taken from

theory to determine the calibrating factors as it has been done for example in [47] or [48]. Consequently, the outcome of the present work does not depend on the used theoretical value but gives direct experimental information. In that sense the derived moments are absolute. Our results show that the tetragonally distorted structure of the films does not have a measurable influence on the total magnetic moment. This may be understood in the following way: In ultrathin films with a small lattice misfit between film and substrate the tetragonal distortion is volume conserving. Only changes in the volume of the magnetic constituents affect the spin magnetic moment, while volume-conserving distortions in the symmetry influence the orbital magnetic moment which is only a small fraction ( $\sim 10\%$ ) of the magnetization. For fcc Co even a change of about 10% in the volume was shown not to affect the spin magnetic moment [130].

In a first approximation it is assumed that the surface ( $\mu_{surf}$ ) and the interface ( $\mu_{inter}$ ) layers of the Co film have different magnetic moments compared to the inner layers ( $\mu_{vol}$ ). A similar moment distribution for a 15 ML Co/Cu(001) was calculated in [26] supporting this assumption. The total moment  $\mu_{tot}$  which is measured with the SQUID is then the average of these contributions:

$$d \cdot \mu_{tot} = (d - 2) \cdot \mu_{vol} + \mu_{surf} + \mu_{inter} \quad (4.1)$$

or, by dividing by the number of layers  $d$ :

$$\mu_{tot} = \mu_{vol} + \frac{\mu_{surf} + \mu_{inter} - 2\mu_{vol}}{d} \quad (4.2)$$

This yields a linear dependence of the magnetic moment with respect to the inverse film thickness. Figure 4.6 reveals such a behavior suggesting that the observed increase of  $\mu$  at the thin film limit is a combined surface/interface effect and the moment distribution assumed above is reasonable. According to eq. (4.2) linear regression (full lines) of the data in Fig. 4.6 can be performed to separate the volume contribution (intercept with the  $y$  axis) and the average of the contributions of both interfaces (slope) — see Table 4.5 for the outcome.

### XMCD measurements of $\mu_L/\mu_S$

The ratio of spin and orbital moment ( $\mu_L/\mu_S$ ) for Co/Cu(001) has been measured before using XMCD [60]. The measurement has been scaled to theory at the thick film limit. The advantage of measuring the ratio is that no calibrating parameters have to be determined, i.e. the degree of polarization of the synchrotron radiation ( $P_c$ ) and the number of 3d-holes ( $n_H$ ). Moreover, the uncertainties due to  $sp$ -background and integration intervals in the determination of the integrated XMCD intensities  $I^+$  and  $I^-$  are not encountered (see e.g. [47], [90], and Section 1.4.3). The ratio  $\mu_L/\mu_S$  as a function of the film thickness  $d$  is given by [60]:

$$\frac{\mu_L}{\mu_S}(d) = \frac{(d - 2) \cdot R_{vol} + R_{inter} + R_{surf}}{d} \quad (4.3)$$

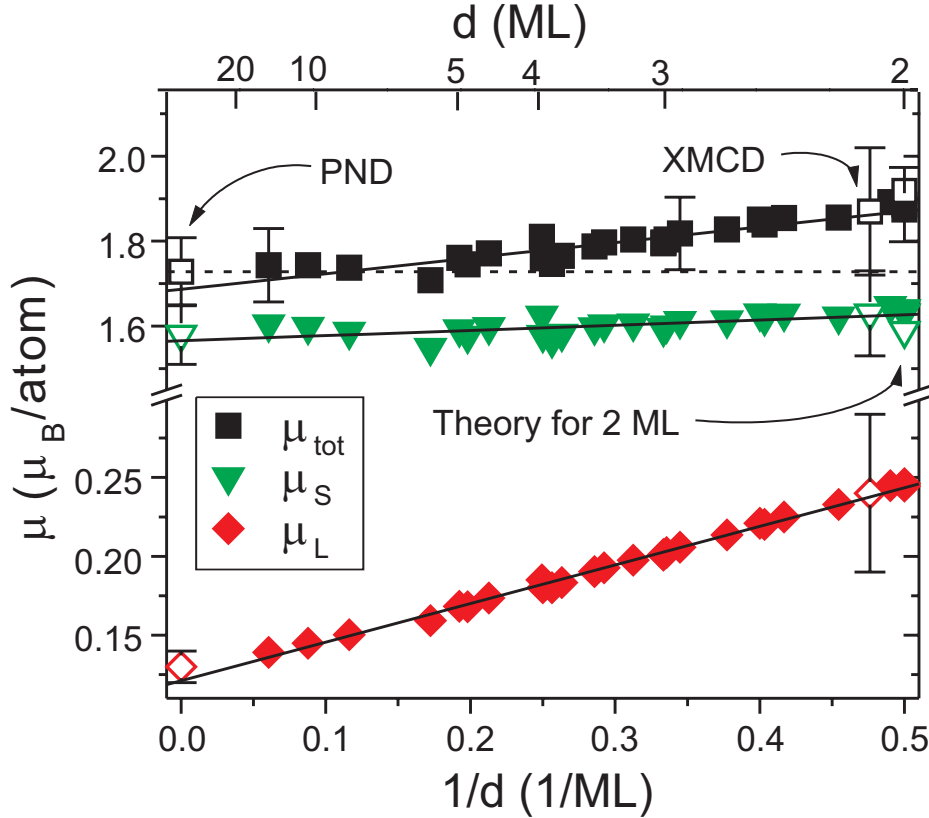


**Figure 4.6:** The total magnetic moment (squares) of Co/Cu(001) vs the inverse film thickness and its separation into spin (down triangle) and orbital (diamonds) contribution [131]. The bulk value is indicated (dashed line) [10]. For comparison experimental results using PND [38] and XMCD [47] are given by the open symbols. Theoretical values for 2 ML are taken from [27] for the total and from [106] for the spin moment.

where  $R_{vol} = 0.078$  corresponds to the bulk value of the ratio,  $R_{surf} = 0.11(3)$  to the surface, and  $R_{inter} = 0.19(5)$  to one ML. These data were derived under the assumption that the increase of the ratio is a pure interface effect, i.e. it should behave linearly with respect to the film thickness. The use of these measurements is justified since the present measurements of  $\mu_{tot}$  yield the same functional behavior.

Combining the findings of the former XMCD measurement for the ratio  $\mu_L/\mu_S$  with the measurements of  $\mu_{tot} = \mu_L + \mu_S$  of the UHV-SQUID magnetometer it is possible to separate  $\mu_L$  from  $\mu_S$  [131]. The resulting spin and orbital moments do not need the calibrating parameters ( $P_c$  and  $n_H$ ) which are required for applying the sum rules. Comparing the measurements of the UHV-SQUID magnetometer with literature (see Table 4.5) one recognizes excellent agreement with old PND data [38] when extrapolating to the bulk limit ( $1/d \rightarrow 0$ ). At the thin film limit

(2 ML) the values are in agreement with experimental values derived by applying the sum rules to XMCD data. Therefore the present measurements may serve as an indirect proof for the reliability of the analysis of the XMCD data in [47].

The measurements with the UHV-SQUID agree with recent theoretical predictions for a 2 ML film as well: the calculated total (open square, [27]) and spin (open down triangle, [106]) moment shown in Fig. 4.6 confirm the results of the present work. If the measurements are extrapolated to 1 ML the outcome (see Table 4.5) matches the values of the total moment derived by theory [27] as well as the extrapolation of the orbital moment in [49]. In summary, the set of magnetic moments derived with the novel UHV-SQUID magnetometer is in excellent agreement with existing literature and bridges between the ultrathin limit and the bulk [126].

thickness	$\mu_{tot}$ in $\mu_B/\text{atom}$	$\mu_S$ in $\mu_B/\text{atom}$	$\mu_L$ in $\mu_B/\text{atom}$	Ref.
bulk	1.68(3)	1.56(3)	0.120(2)	this work
1 ML	2.06(4)	1.69(4)	0.366(6)	this work
2 ML	1.87(3)	1.63(3)	0.244(3)	this work
bulk	1.71(7)	1.58(7)	0.13(1)	[38] (exp.)
2 ML	1.89(15)	1.65(15)	0.24(5)	[47] (exp.)
1 ML	2.11	1.85	0.261	[27] (theo.)
2 ML	1.918	1.73	0.188	[27] (theo.)
1 ML	—	1.71	—	[106] (theo.)
2 ML	—	1.63	—	[106] (theo.)
1 ML	—	bulk	0.355	[49] (exp.)

**Table 4.5:** Linear regression of the datasets for total ( $\mu_{tot}$ ), spin ( $\mu_S$ ), and orbital ( $\mu_L$ ) moment yielding values for the bulk and for 2 ML. Values from the literature are given for comparison.

### 4.3.2 Origin of the enhanced magnetization $M$

From Fig. 4.6 it is obvious that the enhancement of  $\mu_{tot}$  is mainly due to an enhancement of  $\mu_L$  by almost a factor of two [126]. This was previously attributed to a considerable unquenching of the orbital moment at the surface due to the reduced symmetry (missing next neighbors at the vacuum side) [49, 60]. The spin contribution for a 2 ML film is increased by  $0.14\mu_B/\text{atom}$  compared to the bulk. This compares well with a recent theoretical prediction for  $\mu_S$  for such films [106]. This effect is discussed in terms of band confinement which is also due to reduced symmetry [27]. These arguments are equivalent to the discussion with respect to the coordination number of the surface atoms as it has been done in [16].

Up to now, according to eq. (4.2), only the average of  $\mu_{inter}$  and  $\mu_{surf}$  was discussed. Previous calculations for a 15 ML Co/Cu(001) film revealed an enhanced surface contribution ( $\sim 1.85\mu_B/\text{atom}$ ) and a reduced interface one ( $\sim 1.65\mu_B/\text{atom}$ ) which nullify resulting in a bulk-like value [26]. The same was predicted for a 2 ML film [111]. The results in Table 4.5 show that this is not the case. The reduction at the interface does not compensate the enhancement at the surface. By studying the effect of Cu capping it will be possible to deduce values for the two contributing interfaces separately, see Section 4.5.

With the new setup of the UHV-SQUID magnetometer we are in a position to measure a complete set of ground-state magnetic moments for Co/Cu(001) on an absolute scale. Such a complete study can rarely be found in literature. In the case of Co there exists – to the knowledge of the author – only one other study for Au/Co/Au(111) [49]. However, that work is based on room temperature measurements which were fixed to the bulk value. Moreover, the thinnest measured thickness was 4 ML. Therefore the complete thickness dependence of the magnetic moments of Co films shown in Fig. 4.6 represents valuable new input to ultrathin film magnetometry, especially useful for detailed comparison with theoretical predictions, e.g. to figure out which effects should be included within the calculations (orbital moment, orbital polarization, ...).

### 4.3.3 The magnetic dipole operator $\langle T_z \rangle$

In most publications using XMCD magnetometry the total moment is given by the sum of the spin and orbital contribution assuming  $\langle T_z \rangle$  to be small and, therefore, negligible [41, 44, 46]. In [47] a theoretical value for this term was used and the measured spectral intensities of 2.1 ML of Co/Cu(001) were corrected to have a pure  $\langle S_z \rangle$  value. As  $\langle T_z \rangle$  in this case is negative (i.e. antiparallel to the pure spin) the measured value increases if corrected with respect to  $\langle T_z \rangle$ . (The value is indicated in Fig. 4.7 as (1)). In [49] the  $\langle T_z \rangle$  term was deduced from angular dependent measurements but no statement was given if it contributes to the total magnetic moment or not. Calculations revealed for the center layers of Co(0001) a  $\langle T_z \rangle = -0.014$  while it is enhanced to  $-0.24$  at the surface [28]. This is consistent with the experimental results in [49].

In Fig. 4.7 there is some experimental evidence concerning the possible contributions of the total moment (see Section 1.4.4) which is to some extent ambiguous since the effect is smaller than the experimental uncertainty. In the following, the result of the XMCD study in remanence [47] will be compared to the new findings of the UHV-SQUID magnetometer. If one corrects the value (2) with respect to the  $\langle T_z \rangle$  term and the contributions of the  $sp$ -states taken from [27] one ends up with (1) which was published in [47]. The direct outcome of the application of the sum rules is given by (2), this means that no corrections are performed. This value lies slightly above the one derived with the SQUID. If one adds the  $sp$  contributions but does not correct for  $\langle T_z \rangle$ , i.e. assuming that one can

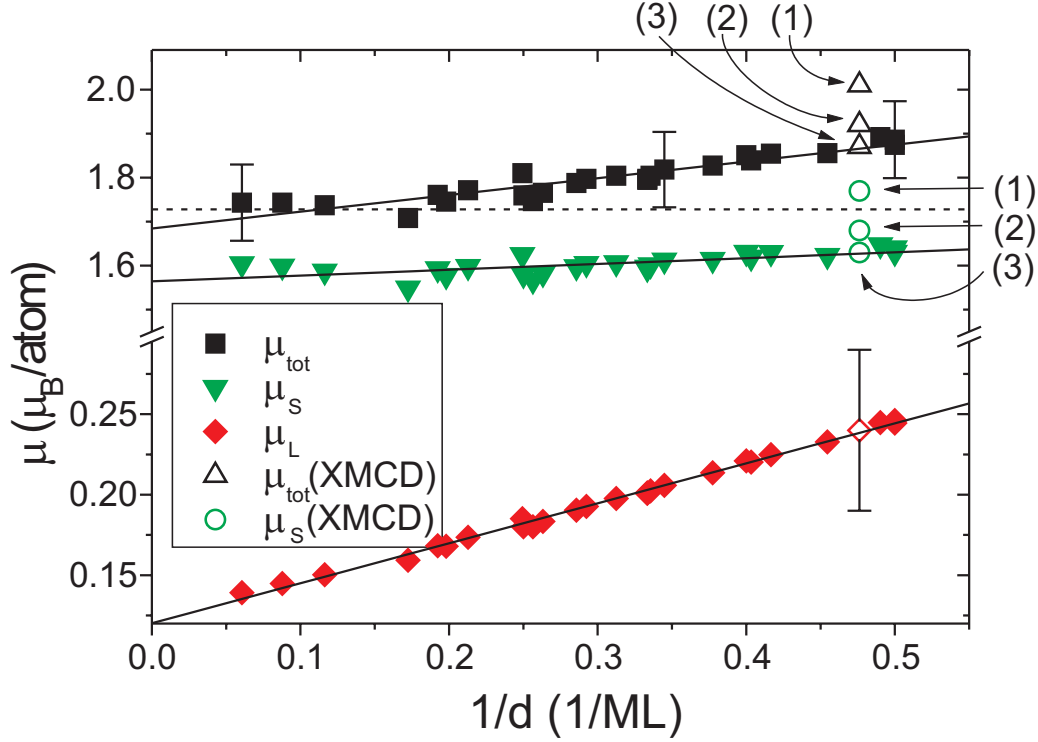


**Figure 4.7:** Measured magnetic moments and its contributions vs the inverse film thickness. Three cases of a sum rule analysis of a 2.1 ML Co/Cu(001) by XMCD are given (open symbols). (1) corresponds to the published values [47] where corrections concerning  $\langle T_z \rangle$  and  $sp$ -contributions were done. (2) are the uncorrected data, (3) implies only corrections with respect to  $sp$  but not for  $\langle T_z \rangle$ .

measure its contribution also with the SQUID, one ends up with (3) which fits best. This suggests that the negative contribution of the  $\langle T_z \rangle$  term is measurable with a classical magnetometry, or, that the remanent measurements indeed sees only the pure spin moment following the suggestions (ii) and (iii) in Section 1.4.4. However, it certainly remains the advantage of XMCD that all three contributing terms can be determined *separately* by angular dependent measurements [49].

To extend this discussion, suggestion (i) of Section 1.4.4 will be followed as well. Then, the total moment would simply be the sum of spin and orbital moment, and the arguments can be turned around. The combination of XMCD and SQUID magnetometry would enable a direct determination of  $\langle T_z \rangle$  combining the two sum rules with the SQUID measurement. This is to subtract the orbital moment derived by the sum rule ( $0.24(5)\mu_B$ ) from the outcome of the SQUID measurement ( $1.87(3)\mu_B$ ) yielding a spin moment of  $1.63(8)\mu_B$ . Since this value equals the value derived by the spectral intensities of the spin sum rule (right side of eq. (1.20)), this leads to the conclusion that  $\langle T_z \rangle$  equals zero. However, this

would be in contradiction with theoretical [28] and experimental [49] findings (but this may be due to the resulting errorbar of about  $0.1\mu_B$  or the finite accuracy of the sum rule itself).

It should be stated that the above discussion is only of relevance if the  $\langle T_z \rangle$  term is non-negligible, e.g. in the ultrathin limit where the reduced symmetry at the surface is predicted to play a crucial role. There has been little experimental work on quantitative magnetometry in that thickness-regime up to now. Consequently, the above question has not been of relevance in most cases so far and the present discussion may contribute in more detail to the disentanglement of spin and orbital contributions in solid state magnetism. At least one should be aware of the complications that may arise.

## 4.4 Magnetic moment profile of Co/Cu(001)

It is the benefit of an UHV-SQUID magnetometer to be able to study the influence of a Cu cap on the magnetic properties of an ultrathin film. This permits separating interface and surface moments to yield a complete moment profile for Co/Cu(001). This results in a determination of the magnetic moment of a surface atom of Co matching the fcc Cu(001) lattice constant. Such numbers derived by experiments can hardly be found in literature although it is of interest to compare the findings with theoretical calculations. The present UHV-SQUID magnetometer is a relatively simple apparatus to measure surface moments.

### 4.4.1 The influence of Cu capping

The motivation to study the effect of capping a ferromagnetic film with a protective layer is to reveal interface and surface moments separately. It is common to prepare systems in UHV and protect them with capping layers of Au, Pt, Pd, Cu etc. for chemical stability. Such capped samples are often measured only after capping with *ex situ* techniques and they are useful for applications. For thick films and multilayers the effect of a protective layer is negligible since only the surface is affected. If the magnetic properties of ultrathin films are studied this is not the case any more. Capping alters significantly the magnetic observables like  $T_C$  and  $M$  in the ultrathin limit [47, 92]. The UHV-SQUID makes the effect on  $M$  sizable on an absolute scale.

The measurements for the bare Co films clearly demonstrate the reliability of the derived data. This encourages to check the quality of the uncapped films by a single room-temperature magnetization measurement. If the quality seemed to be adequate (a value well-comparable to the measurements represented by the open up-triangles in Fig. 4.4) they were immediately capped with  $\sim 5$  ML of Cu. This obviates to measure a complete temperature dependent measurement of the uncapped film which lasts for about 2 h implying the danger of considerable

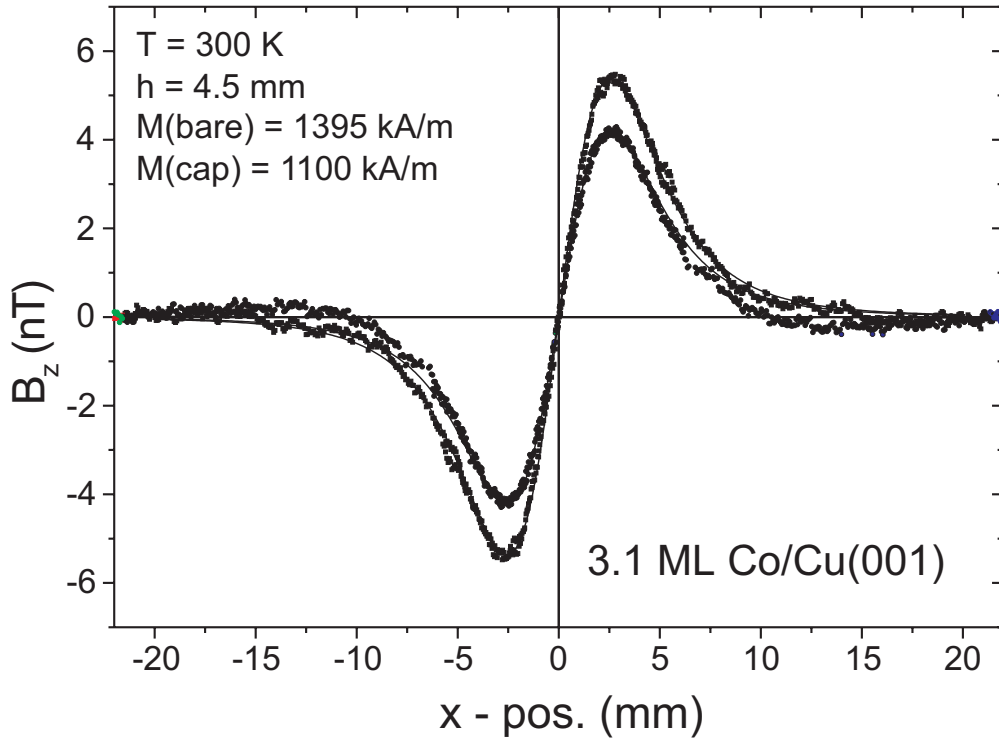


**Figure 4.8:** Measured stray field of a Co film before and after capping with  $\sim 5$  ML of Cu at 300 K. The magnetization changes by about 21% due to the capping [132].

contamination by residual gases. Contrary to that, the procedure of capping after one single room-temperature scan takes only 15 min. The capped film is then measured as a function of temperature to enable extrapolation to  $T = 0$  K. In Fig. 4.8 the effect of a Cu protective layer is shown for a 3.1 ML Co film. The bare film has a magnetization of 1395(60) kA/m at  $T = 300$  K. Capping with 5 ML of Cu reduces the magnetization by about 21% to 1100(60) kA/m. This reduction is caused by two influences: (i) The  $T_C$  of the capped film is known to be lower than for the uncapped [97]. Therefore, the reduced temperature  $t = T/T_C$  of the measurement changes, leading to a lower magnetization of the film. (ii) The surface layer of the film is turned into an interface layer which is, in a first approximation, equivalent to the one next to the substrate. This was shown to affect the magnetic moment of 2 ML Co/Cu(001) [62]. To discuss ground-state moments one has to focus on (ii). This is to measure at various low temperatures and extrapolate to  $T = 0$  K to avoid uncertainties due to determination of  $T_C$ . As stated above, this procedure is followed here. The results are shown in Fig. 4.9. For the uncapped films the  $T = 0$  K measurements shown in Fig. 4.6 were taken. Only the values at  $T = 0$  K are shown in the line of the above mentioned option (ii). Only films with an integer number of layers (2, 3, and 4 ML) were capped to

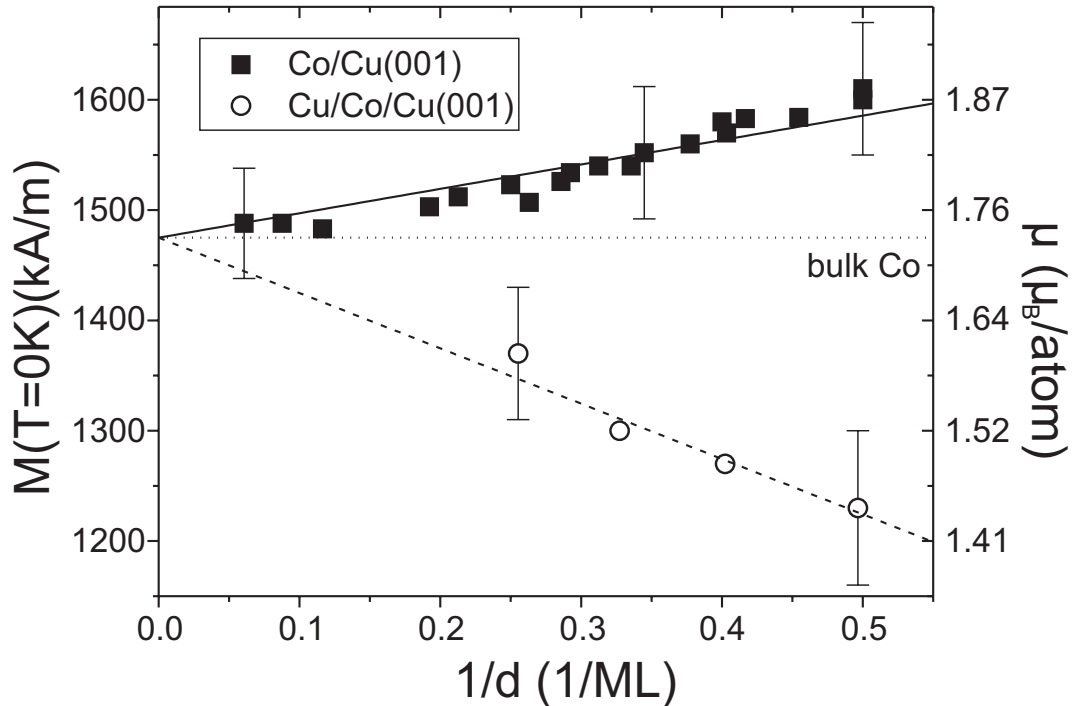


**Figure 4.9:** Magnetic moments for Co/Cu(001) (squares) and Cu/Co/Cu(001) (circles) vs the inverse Co film thickness [132]. The straight lines are derived by linear regression fixing the intercept with the  $y$  axis to the bulk value.

end up with a flat interface between film and cap. A single film with maximum surface roughness (2.5 ML) was chosen to test if there is a strong difference in the reduction compared to 2 or 3 ML. The smooth linear behavior with respect to the inverse film thickness (Fig. 4.9) suggests that the reduction is not affected significantly by the surface roughness. The effect of capping is pronounced at 2 ML (24%) while it decreases down to 8% at 4 ML which is almost within the errorbar. Therefore, measurements revealing the effect of capping as discussed above are only meaningful if they are performed on films thinner than  $\sim 5$  ML.

#### 4.4.2 The separation of surface and interface moments

Figure 4.9 shows that the magnetic moment of the capped films is strongly reduced at the thin film limit. This is caused by replacing the surface (vacuum side) by a Cu-facing interface. In analogy to eq. (4.2) a model is chosen where only the interface and the surface layers are affected by the proximity to vacuum and Cu respectively. The volume contribution (the inner layers) is fixed to the bulk value, supported by the findings of thick films which are magnetized like the bulk (Fig. 4.6). The interface contribution is reduced by a factor  $R$ , while the

surface moment is increased by  $E$ . Then the thickness dependence of the average magnetic moment for the uncapped film is given by:

$$\mu_{tot}(d) = \mu_{tot}(bulk) + \frac{\mu_{tot}(bulk) \cdot (R + E - 2)}{d} \quad (4.4)$$

whereas for the capped film  $E$  is substituted by  $R$ . This implies that both interfaces are assumed to be equivalent.

Fixing the bulk value to  $1.73\mu_B/\text{atom}$  is justified since linear extrapolation of the data to  $1/d \rightarrow 0$  leads within 1.5% to the same value for both, the capped and the uncapped thickness-series. Linear regression of the data sets and an analysis according to eq. (4.4) lead to an interface magnetic moment which is reduced by 17(3)% to  $1.43\mu_B/\text{atom}$  ( $R = 0.83(3)$ ) and a surface one which is enhanced by 32(5)% to  $2.28\mu_B/\text{atom}$  ( $E = 1.32(5)$ ) with respect to the bulk [132]. Recent experimental work using XMCD report a comparable value ( $1.41\mu_B/\text{atom}$ ) for a 2 ML capped Co film (= two interface layers) [62], but XMCD is also sensitive to changes in the electronic structure. In that sense the present work is an independent proof for the reliability of the XMCD measurements.

The values for the surface and interface moments have been deduced under the assumption that the two interfaces, namely Co on Cu (interface A) and Cu on Co (interface B), are identical. However, it is known [102, 105] that the first ML of Co on Cu is an interface alloy with 25% Cu concentration while interface B is not intermixed. This is due to the fact that the surface energy of Cu is lower compared to Co [105, 106] which hinders the Co atoms to exchange their positions with the deposited Cu atoms.

How much does the limited intermixing affect the results? There are two extreme limits: (i) There is intermixing at interface A, however this has almost no influence on the magnetic moments of the ultrathin films. This was shown, for example, recently for ultrathin Ni/Cu(001) films in the thickness range of 4-5 ML [133]. Consequently, the values for the surface and interface moments of Co are correct within the experimental error bar. (ii) As in bulk Co-rich CoCu alloys there is a linear reduction of the Co moment with the Cu concentration [48]. Then the moment at the diffused interface A should be 25% smaller and, consequently, one has to recalculate the Co moments at the surface. The outcome of such a calculation is a surface moment of  $2.51\mu_B/\text{atom}$ , a moment of interface A ( $1.63\mu_B/\text{atom}$ ), and interface B ( $1.23\mu_B/\text{atom}$ ). In the following we restrict ourselves to (i) because the outcome can be taken as a lower limit for the surface moment. Moreover, in the case (ii) the reduction of the moments at the interface to the substrate is certainly overestimated because contrary to a bulk alloy this interface alloy is in contact with an almost pure Co layer which should increase the moment of the interface alloy [133].

In Fig. 4.10 the measured moment distribution of Co/Cu(001) is sketched. The reduction at the interface is more pronounced than predicted by theoretical calculations; for a 15 ML film Co on Cu(001) an interface moment of  $1.65\mu_B/\text{atom}$

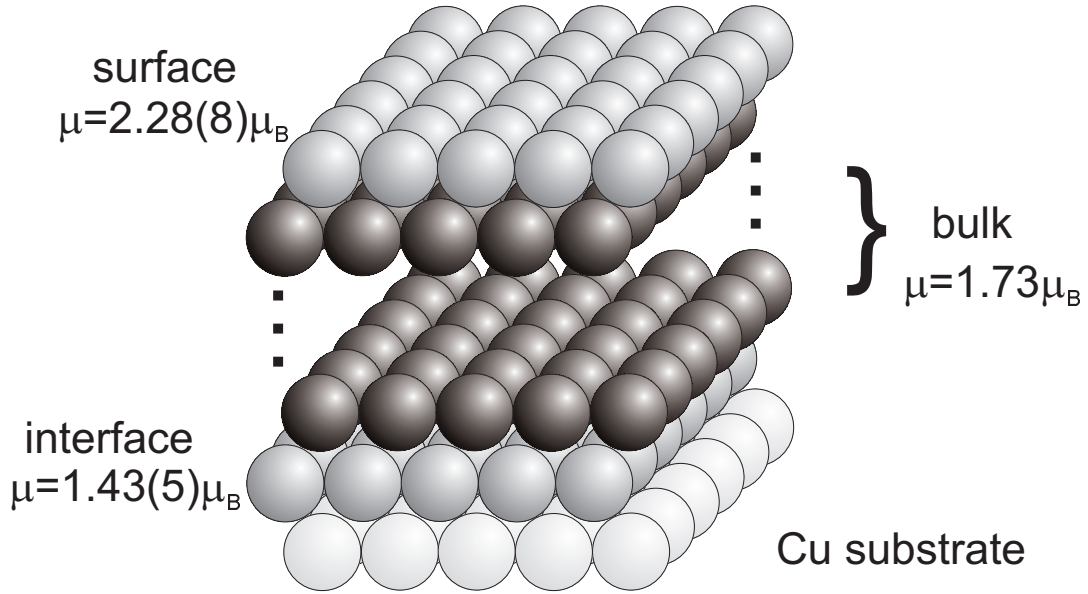


**Figure 4.10:** Moment distribution in Co/Cu(001) when both interfaces are assumed to be equivalent (see text) [132].

is derived [26]. This may be attributed to the fact that the interface is assumed to be ideally flat which is certainly not the case in the experiment (see discussion above). The enhancement of the surface magnetic moment can also be discussed with respect to theoretical values for the free standing ML ( $2.40\mu_B/\text{atom}$ ) and the ML Co/Cu(001) ( $2.11\mu_B/\text{atom}$ ) [27]. The measured value of  $2.28(8)\mu_B/\text{atom}$  lies in between. This is well understood by considering that the free standing ML has the maximum enhanced moment since it has the most reduced symmetry. On the other hand the 1 ML Co/Cu(001) faces on the one side the Cu(001) and on the other the vacuum, that is it has a negative (proximity to Cu) and a positive (vacuum side) contribution to its moment. Contrary to that, the surface of the studied films is in proximity to a ferromagnetically ordered Co layer which gives a more positive contribution to the moment than being in proximity to a non-magnetic Cu layer. In summary, the measured enhancement of the surface magnetic moment by 32(5)% is consistent with theoretical findings on MLs [132].

The moment profile for Co/Cu(001) represents new experimental input to thin film magnetism. It contains the full information of measurements of the ground-state magnetic properties of capped and uncapped films as a function of the film thickness. The functional behavior suggests that both, the reduction and the enhancement are pure interface effects. However, the UHV-SQUID magnetometer can not provide layer-resolved magnetic information directly. Due to the relatively small errorbars the measurements of the total magnetic moment allow a meaningful comparison between theory and experiment. It is the benefit

System	Surface moment per atom	Ref.	Method
Co(001)	$+32 \pm 5\%$	this work	UHV-SQUID
Fe(110)	$+39 \pm 16\%$	[18]	UHV-TOM
Ni(001)	$+5 \pm 5\%$	[19]	SPLEED
Ni(111)	$+10 \pm 20\%$	[20]	SPLEED

**Table 4.6:** Experimentally determined surface moments for the 3d transition metals in different crystallographic structures.

of comparing quantitative measurements with theoretical calculations that it is possible to show which effects should be taken into account within the calculation. It is obvious that calculations which neglect the orbital moment, e.g. [106], derive an enhancement at the film surface which is too small. From the values given in [27] one can see that if one wants to compare the results on an absolute scale, the calculations should take into account the orbital polarization as well. This was found for thick Co films before [46].

Table 4.6 summarizes the values for experimentally determined surface moments. While the SPLEED method seems to derive insignificant enhancement for the case of Ni surfaces, TOM and SQUID detect strong enhancement of the Fe and Co magnetic moment at the surface. Note that the possibility to reach low temperatures and the complete thickness dependence of the magnetic moment of Co measured in the present work yields a smaller uncertainty of the surface moment determination compared to the TOM measurement.

## 4.5 Films below 2 ML

The growth of Co/Cu(001) below 2 ML and the effect of the sudden increase of  $T_C$  at the critical thickness  $d_c = 1.7(1)$  ML have been discussed before. The possibility to measure the magnetization at low temperatures with submonolayer sensitivity triggered some experiments at and below  $d_c$  to study the influence of soft thermal treatment.

In Fig. 4.11 a measurement of 1.75 ML Co/Cu(001) at 55 K is shown (larger signal). This film shows a clear ferromagnetic signal at 300 K which indicates that it is placed above  $d_c$ . The temperature dependent measurement shown in the inset allows to extrapolate to  $T = 0$  K leading to a magnetization of 1690(90) kA/m corresponding to  $1.98(8)\mu_B/\text{atom}$ . This is enhanced by 14% with respect to bulk Co. The extrapolation is possible because the reduced temperature  $t = T/T_C$  is about 0.17 since  $T_C = 320$  K according to Fig. 4.2. The strongly enhanced magnetic moment matches the previously measured films above 2 ML suggesting that the observed linear behavior can be extended up to  $d_c$  [134].

In case of a 1.5 ML Co/Cu(001) film (Fig. 4.11, smaller signal) the film ex-

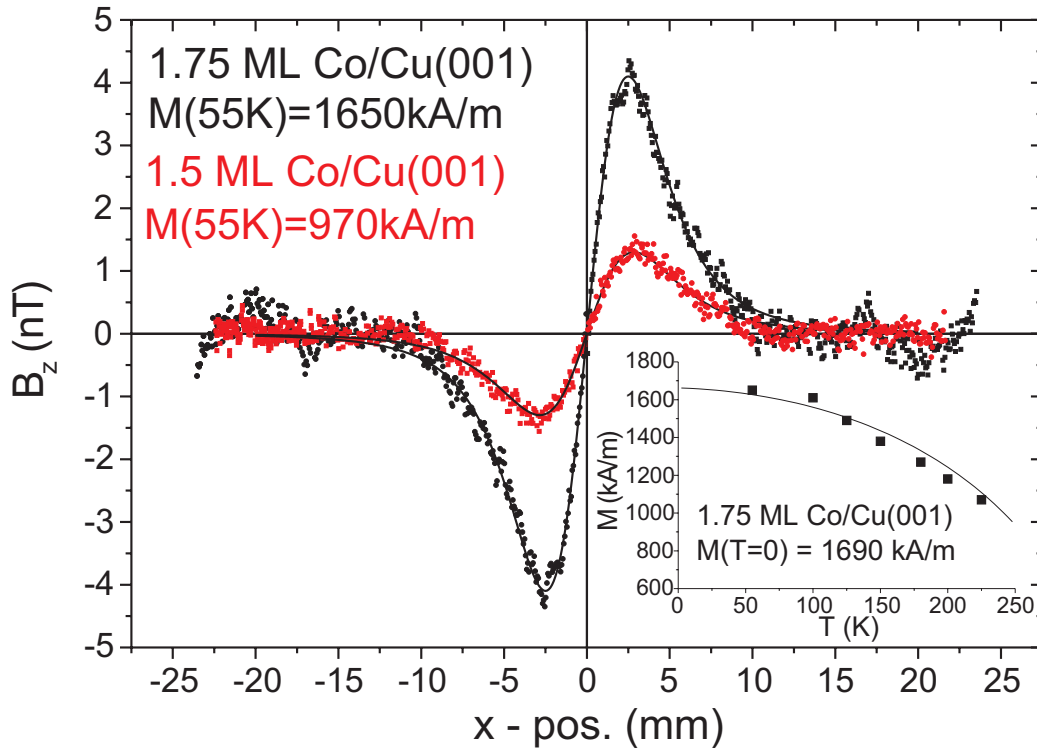


**Figure 4.11:** Measured stray field of a 1.75 ML Co/Cu(001) film at 55 K showing a magnetization of 1650(80) kA/m. The inset shows a temperature dependent measurement and the extrapolation to  $T = 0$  K resulting in  $M = 1690$  kA/m [134]. The stray field of a 1.5 ML thick film at 55 K is shown for comparison. The fitted magnetization is strongly reduced to 970(90) kA/m.

hibits no ferromagnetic signal down to  $\sim 90$  K. This shows that it is placed below  $d_c$ . Therefore, the reduced temperature is about 0.6 (at the lowest measuring temperature of 55 K) which makes the extrapolation to  $T = 0$  K questionable. Consequently, only a result for the magnetization can be given which is 970(90) kA/m at 55 K [134].

All films below  $d_c$  were first measured in the as-grown state. The outcome of these experiments is summarized in Fig. 4.12 (open symbols). Since the signal-to-noise ratio of such thin films is about 3–5 the fitted values of  $M$  for different stray field scans scatter. This is reflected in the relatively large errorbars of 200 kA/m in Fig. 4.12. The data points represent an average value of the different measurements of one single film. This may explain the difference of the fitted  $M$  shown in Fig. 4.11 (970(90) kA/m) and the averaged  $M = 800(200)$  kA/m in Fig. 4.12. Subsequently, the films below  $d_c$  were annealed up to 400 K for about 5 minutes and measured again (full symbols in Fig. 4.12). The thinnest film at 1.3 ML was measured only after annealing and exhibited a magnetization of about

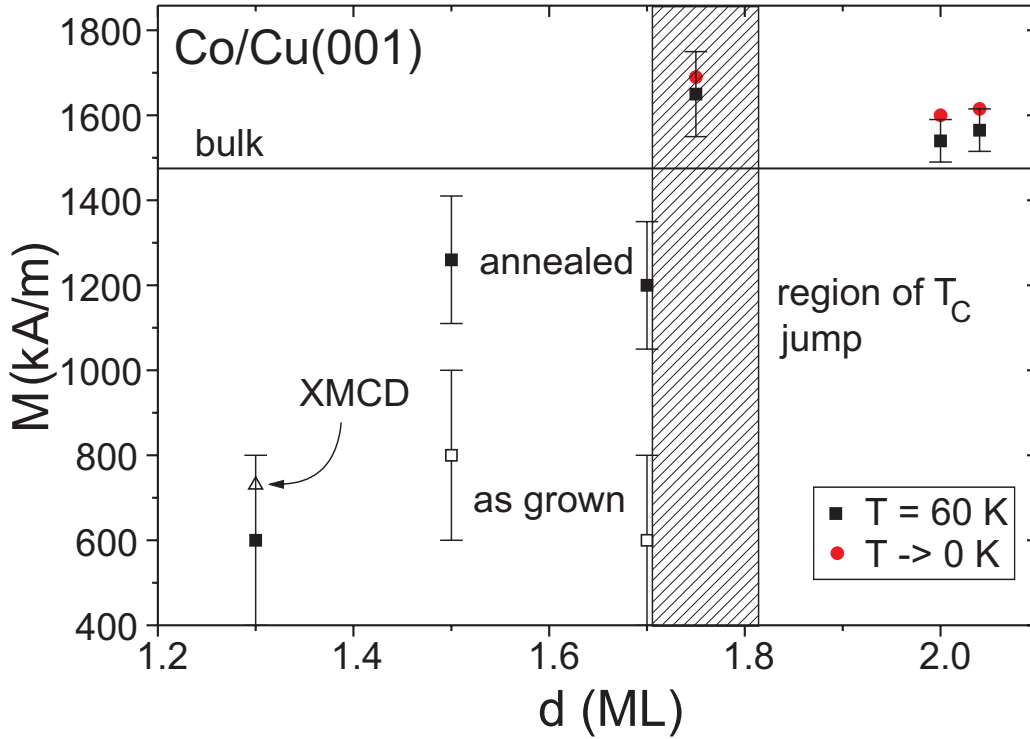


**Figure 4.12:** Magnetization of films with thickness under 2 ML. Some of the films were annealed to 400 K for about 5 minutes. The XMCD value is from [135].

600(200) kA/m at 60 K which is consistent with a recent XMCD study which revealed 730 kA/m at 40 K for a film of the same thickness [135]. In the case of 1.5 and 1.7 ML the magnetization increased considerably ( $\sim 50\%$ ) after thermal treatment. The magnetization of the films above  $d_c$  did not change significantly upon soft thermal treatment.

In addition to the UHV-SQUID measurements MOKE experiments in the same thickness range were performed. Some hysteresis loops are shown in Fig. 4.13 for 1.6 ML (a), 1.5 ML (b), and 1.4 ML (c). In the as-deposited state (solid line) film (a) exhibits a rounded hysteresis loop with finite remanence and coercivity. This may be taken as an evidence for ferromagnetism supported by the SQUID measurements which clearly show a remanent signal below  $d_c$ . It should be noted that recent calculations show that an ensemble of islands could lead to rounded hysteresis loops provided that magnetic dipole coupling between the islands is present [136]. STM work with element specificity supports such a model [102]. Indeed, a loose Cu-network has been shown to act as a skeleton for the aggregation of Co in the first ML of growth. Co forms large clusters which may be considered to be coupled via dipolar forces. The total concentration of Co in the first ML has been found to be about 75% [102].

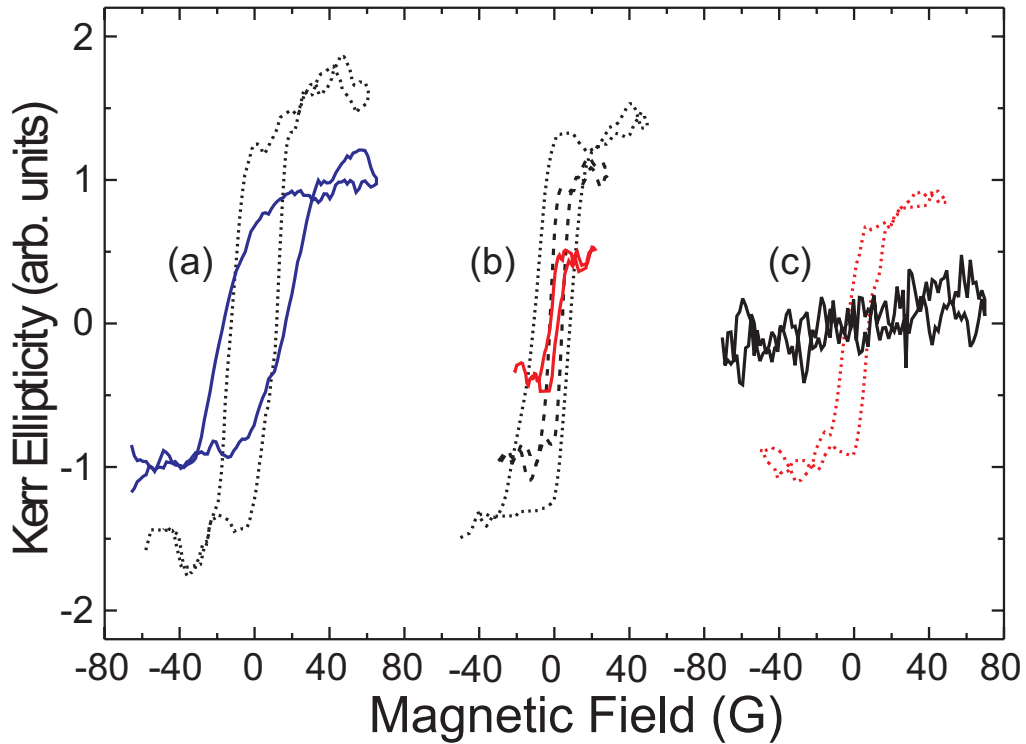


**Figure 4.13:** Hysteresis loops of Co/Cu(001) at three different thicknesses below  $d_c$ . The film thicknesses were 1.6 (a), 1.5 (b), and 1.4 ML (c) respectively. Solid lines correspond to the as-deposited state, dotted lines to the annealed films.

Soft thermal treatment (as described above) modifies significantly the hysteresis loops (dotted lines in Fig. 4.13). The signal increases by about 50% and the hysteresis itself becomes more square-like. To compare the loops of the different films one has to use the same reduced temperature. Since the temperature of the measurements (110 K in the case of the MOKE setup) are far above  $T = 0$  K one can not conclude from an increased MOKE signal if the magnetization or the  $T_C$  is increased. In Fig. 4.13 (b) loops for 1.5 ML Co/Cu(001) are shown before (solid) and after annealing (dotted line). Obviously, the temperature of 110 K is close to  $T_C$  for the as-deposited film. For the annealed film  $T_C$  was found to be at about 215 K where the MOKE signal vanished. A loop recorded at 165 K (dashed line) may illustrate this. For the 1.4 ML film (Fig. 4.13 (c)) the as-deposited film is clearly paramagnetic (i.e. the measuring temperature of 110 K is above  $T_C$ ). After annealing the  $T_C$  is found to be  $\sim 135$  K and one can see a clear hysteresis loop at 110 K. Metastability of room-temperature grown films upon annealing reported in [108] seems to be a general property of all films below  $d_c$ .

The observed magnetic properties of Co/Cu(001) films below  $d_c$  can be un-

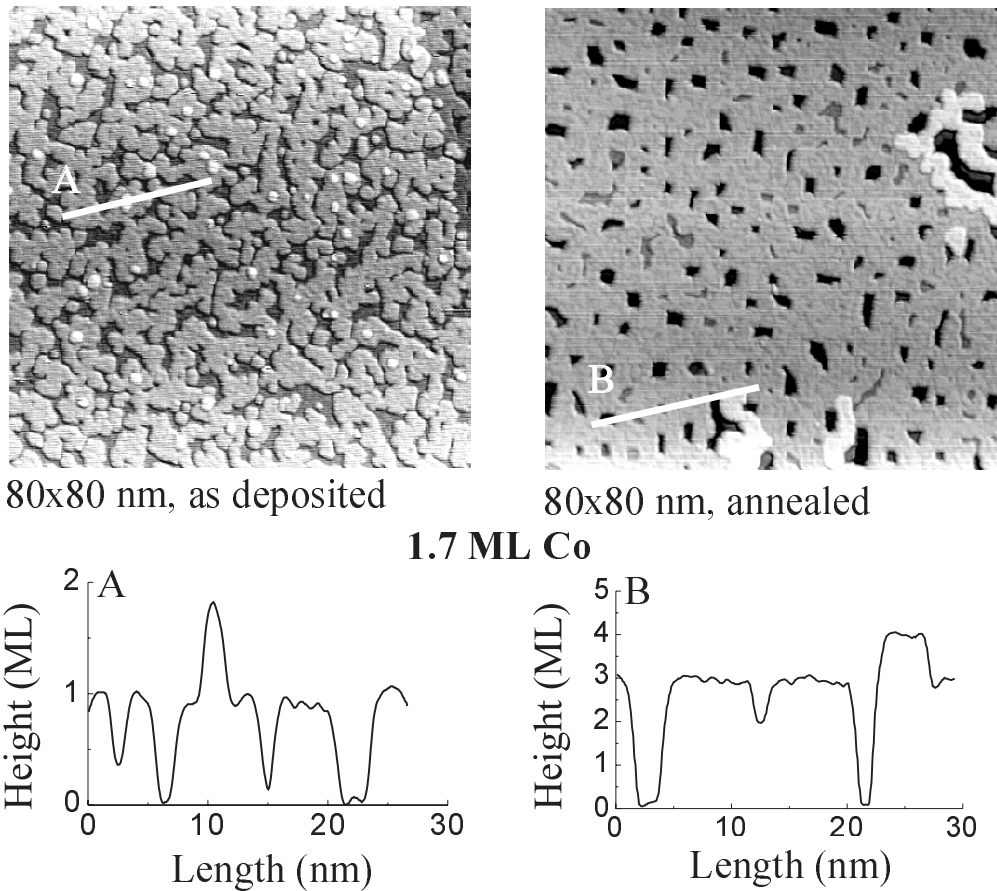


**Figure 4.14:** Effect of soft thermal treatment (10 min at 400 K) for a 1.7 ML Co/Cu(001) film. The roughness in the as-deposited state is  $\pm 1$  ML while the annealed film shows large holes of 3 ML depth (see line-scans).

derstood in more detail by studying the related structural changes with the help of the STM. This was done for a 1.7 ML Co film which was measured before and after the above-mentioned thermal treatment. The STM pictures are shown in Fig. 4.14 together with two representative line scans which are indicated by the white lines. In the as-deposited state the substrate is almost completely covered by the first ML. The islands (gray) cover a large percentage of the surface and the roughness is  $\pm 1$  ML. The islands are assumed to consist of a mixture of Co and Cu (see Section 4.1.1). After annealing there is a drastic change in the structure. The film looks much smoother with few holes which are 3 ML deep (see linescan “B”). The suggested model is a phase separation between Co and Cu similar to the one observed in Co/Ag multilayers upon annealing [137]. Then, Figure 4.14 can be understood in the following way: Cu and Co (which are immiscible in the bulk) separates forming doublelayers of Co covered with

Cu whereas the first layer of Co could contain some amount of Cu. Recent total energy calculations have demonstrated that a doublelayer of Co capped with Cu is the most favorable constellation when the system is in its thermodynamic equilibrium [106, 107]. These findings support that Cu covered doublelayers are formed upon annealing. Another evidence for this is the fact that  $M(60\text{ K})$  of the 1.5 ML and the 1.7 ML film measured with the SQUID after annealing equals  $M(60\text{ K})$  of the capped 2 ML film in Fig. 4.9 irrespective of the film thickness.

Above  $d_c$  the topmost layer consists almost purely of Co which leads on the one hand to the nice layer-by-layer growth. On the other hand, the energetic barrier for the Cu to move on top of the Co becomes larger. Consequently, the films can stand thermal treatment up to 450 K without considerable changes in their magnetic properties.

# Chapter 5

## The system Ni/Cu(001)

This Chapter reports first results for Ni films grown on Cu(001) measured with the UHV-SQUID. This demonstrates the ability to measure other systems besides Co as well. Ultrathin Ni films require even lower temperatures and higher sensitivity compared to Co since both, the Curie temperature, and the magnetic moment are lower. Ni exhibits interesting magnetic properties which will be discussed briefly before presenting the results. The derived magnetization values between 4 and 9 ML with and without a Cu-protective layer are in good agreement with new theoretical calculations as well as with a recent XMCD study.

### 5.1 Structural and magnetic properties of Ni/Cu(001)

The growth of Ni on Cu(001) is quite different compared to Co. The first 3-5 ML grow layer-by-layer. Then the growth is dominated by a pyramidal growth mode leading to a surface roughness of 0.5 to 1.5 nm from 9 to 45 ML [138, 139]. It was shown that the structural properties like the roughness of the Ni films does not significantly alter the magnetic anisotropy of ultrathin Ni films [138], or, in the case of exchange processes at the interface, the magnetization [140].

The magnetic properties of ultrathin Ni films grown on Cu(001) attracted a broad experimental and theoretical interest in the past, see [141, 142] for an overview. This is mainly due to the fact that Ni exhibits a spin reorientation transition from in-plane to out-of-plane magnetization at a film thickness of about 7-8 ML [143]. Out-of-plane magnetized films are of practical interest since high density data recording requires out-of-plane bits which can be of smaller size than the in-plane ones. The reorientation transition is governed by an interplay of surface and volume contribution to the anisotropy where the latter is enhanced compared to the bulk because of a tetragonal distortion due to pseudomorphic growth [142, 143]. It has been excluded that the spin reorientation transition is induced by structural changes in the film.  $I(E)$ -LEED measurements reveal

that the tetragonal distortion of the film due to the pseudomorphic growth is maintained up to 11 ML with no significant changes in the lattice spacing [144]. The surface anisotropy, and therefore the spin reorientation transition, can be affected by capping (or contaminating) the film [145]. More recent experiments show that the reorientation transition occurs at about 10 ML and can be shifted by gas adsorption or metallic capping layers down towards thinner films [145, 146].

Moreover, a second reorientation transition should occur at about 5 ML. This transition is a pure in-plane one where the in-plane easy axis changes from the [100] to the [110] direction [147]. However, the films seem to be almost isotropic in the film plane since the anisotropy is very small.

Quantitative measurements of the magnetization of ultrathin Ni films can hardly be found. TOM studies provide results on surfaces and interfaces of Ni(111) [17, 30]. Few data using XMCD are available for Ni single layers grown on Cu(001) [47, 62]. From 3 to 5 ML these studies reveal magnetization values between 250 and 450 kA/m at 40 K, no matter if the films were measured along the [100] or the [110] in-plane direction indicating that the films are almost isotropic in the film plane. The results can be compared with the bulk value of 528 kA/m corresponding to  $0.619\mu_B/\text{atom}$  [10].

Theoretical calculations predict quite different bulk values for Ni(001) like  $0.638\mu_B/\text{atom}$  [27],  $0.57\mu_B/\text{atom}$  [148], or  $0.69\mu_B/\text{atom}$  [149]. 1 ML Ni/Cu(001) is predicted to be in a ferromagnetic state with a reduced moment of  $0.54\mu_B/\text{atom}$  [27], or  $0.13\mu_B/\text{atom}$  [148]. For a 4 ML Ni/Cu(001) film, layer resolved calculations reveal enhanced surface spin(orbital) ( $0.74(0.068)\mu_B/\text{atom}$ ) and reduced interface ( $0.46(0.043)\mu_B/\text{atom}$ ) magnetic moments [149]. Compared to the bulk value reported in that work, this is an enhancement by 1.1%. 2 MLs of Cu cap reduce the magnetic moment by 11.5% which is caused by a reduction of the magnetic moment of the topmost layer down to  $0.46\mu_B$  [149].

## 5.2 First results for capped and uncapped Ni films

The UHV-SQUID measurements of Ni/Cu(001) are less complete compared to the Co/Cu(001) ones. Before measuring Ni films the accessible temperature range was improved down to 40 K by optimizing the sample mounting according to the discussion in Section 3.1.3. This was necessary since the  $T_C$  of Ni films with  $d < \sim 6$  ML is below room temperature. Since the magnetic moment of Ni is reduced by a factor of 3 compared to Co, the expected stray field of Ni films is only in the order of 1 nT. Therefore measurements of Ni films prove the sensitivity of the UHV-SQUID magnetometer. Low-temperature (40 K) measurements have been carried out between 4 and 9 ML of Ni/Cu(001) with and without Cu capping layers and will be discussed in the following.

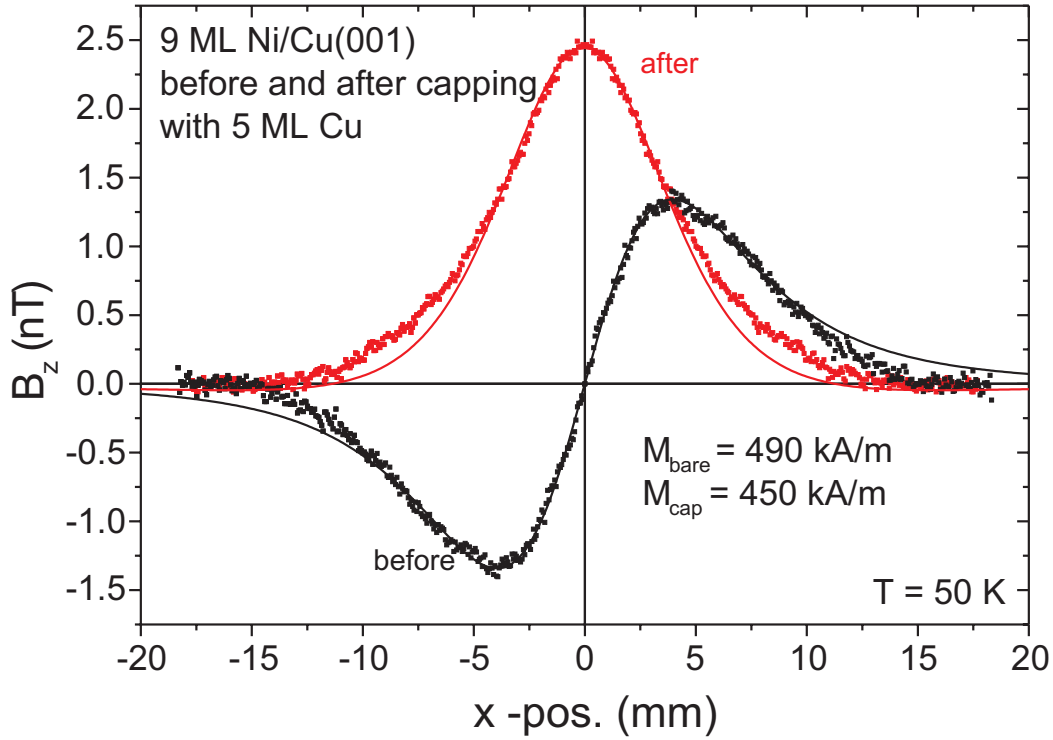


**Figure 5.1:** Stray field distribution for a 9 ML Ni/Cu(001) film before and after capping with 5 ML of Cu. The magnetization of the capped film is obviously out-of-plane while the uncapped shows in-plane anisotropy. The fitted magnetization values do not differ significantly within the error of 90 kA/m.

In the thick film limit a 9 ML Ni/Cu(001) film changes the easy axis of magnetization upon Cu capping. In Fig. 5.1 the stray field is shown before and after capping with Cu. While the distribution of the bare film is unambiguously originating from an in-plane magnetized film the capped one shows only a single peak as is expected for an out-of-plane magnetization (see Fig. 3.9).  $M$  of the out-of-plane magnetized film is fitted according to eq. (3.5) yielding 450(100) kA/m while the in-plane film shows  $M = 490(80)$  kA/m. No significant reduction of  $M$  is detectable within the experimental uncertainty<sup>1</sup> although the easy axis is rotated by 90°. A similar change of the anisotropy of a 9 ML Ni film upon Cu capping was observed recently with FMR [146] which is consistent with the findings of MOKE in [145] as well. This indicates that the film is right below the reorientation transition.

Contrary to that, a 8 ML Ni film with (and without) a cap of 5 ML of Cu exhibits a signal which unambiguously corresponds to an in-plane magnetized

<sup>1</sup>The error for the out-of-plane film is larger since the determination of  $h$  is less safe, see Section 3.3.2.

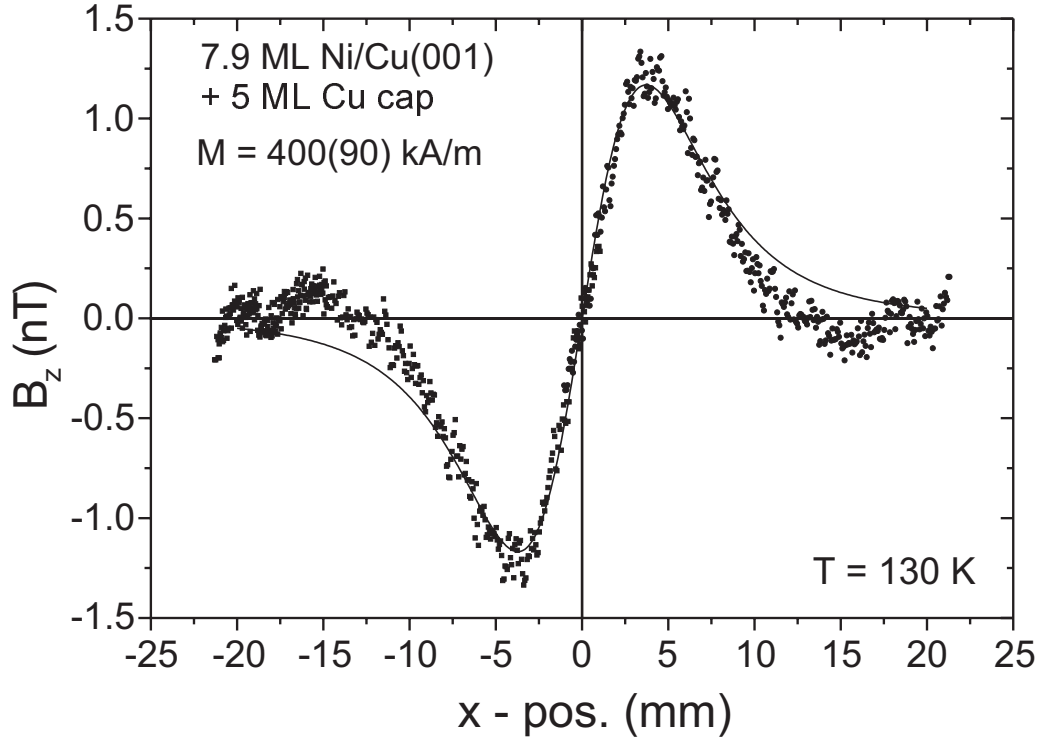


**Figure 5.2:** Capped 7.9 ML Ni film at 130 K showing clear in plane magnetization which confirms that the film is placed well below the reorientation transition. Due to the measuring temperature the magnetization is reduced compared to the bulk value of 528 kA/m.

film over the whole temperature range from 40 to 130 K. This suggests that this film is well below the reorientation transition. In turn, this confirms that the film is prepared in a smooth and clean way. Another film of the same thickness exhibits a stray field indicating an out-of-plane anisotropy but a clear Carbon peak was detectable in the Auger electron spectrum. The magnetization of the clean film is found to be bulk-like (480(90) kA/m) without a Cu cap and no significant reduction due to the Cu capping is detectable.

The 4 ML film exhibits a slightly reduced magnetization of 490(80) kA/m (Fig. 5.3). However, the measuring temperature of 40 K corresponds to a reduced temperature of 0.16 assuming a  $T_C$  of 250 K [62, 151]. The magnetization is therefore about 93(2)% of  $M(T = 0)$ . A simple correction using the spin wave law leads to a  $M(T = 0)$  of 524(95) kA/m which is bulk-like. Contrary to previous measurements using XMCD [47] no reduction of the magnetic moment for 4 ML of Ni/Cu(001) is found. The magnetic moment of the Ni film is  $0.61(11)\mu_B/\text{atom}$  assuming the easy axis to be along the in-plane [110]-axis which is the more likely

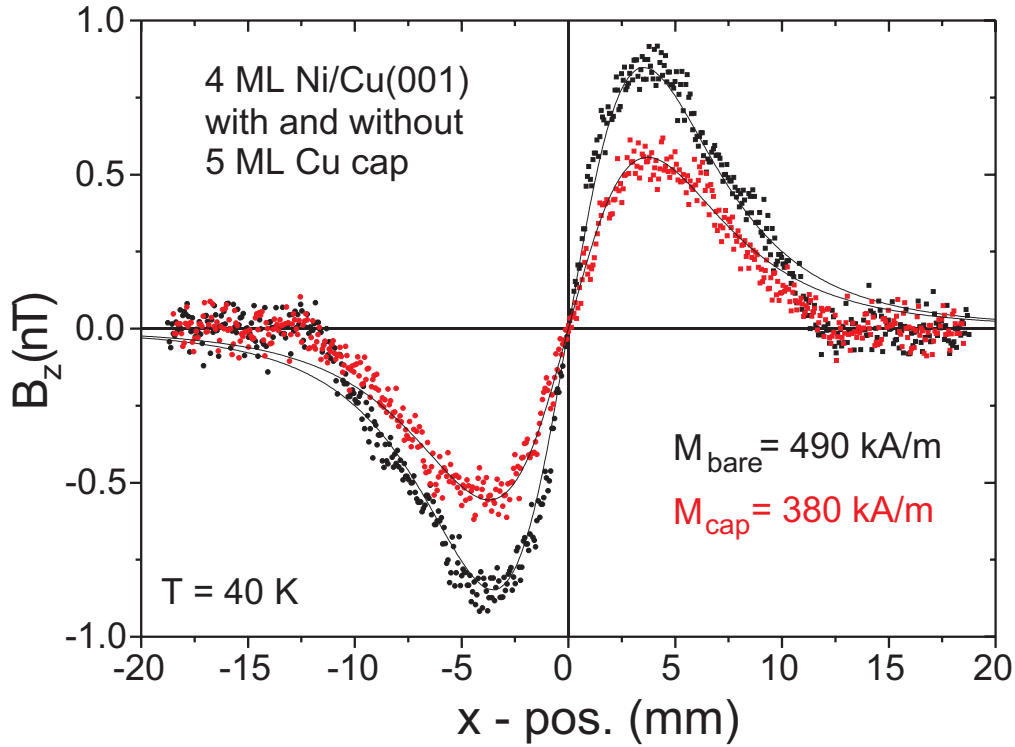


**Figure 5.3:** Stray field of a 4 ML Ni film with and without Cu cap [150]. Magnetization values are given for a temperature of 40 K. A clear reduction of 22% due to Cu capping is visible.

case.<sup>2</sup> This value is in good agreement with the theoretical prediction claiming a slight enhancement of 1.1% compared to the bulk for such a film [149].

Capping with 5 ML of Cu reduces the magnetization of the 4 ML Ni film by  $\sim 22\%$  down to 380 kA/m at 40 K [150], see Fig. 5.3. The signal-to-noise ratio of the measurement in Fig. 5.3 is 5 for a single scan without any data smoothing confirming the high sensitivity of the UHV-SQUID. According to [62] a reduction of  $T_C$  by about 30 K is assumed due to the cap. Therefore the reduced temperature changes to 0.19 and the measured  $M$  is only 92% of the  $T = 0$  K value leading to  $M(T = 0) = 410(90)$  kA/m. Consequently, the pure effect of the Cu capping is 21%. Although correcting the effects of a reduced  $T_C$  relying on a rough estimate, this clearly shows that the observed reduction of  $M$  is mainly due to the Cu capping and not to changes in the reduced temperature. The magnetic moment of a capped 4 ML Ni/Cu(001) film can be estimated to be  $0.48(12)\mu_B/\text{atom}$ . The reduction of the magnetic moment due to Cu capping is found to be more pronounced than expected by theory [149].

<sup>2</sup>If one assumes the easy axis to be the in-plane [100], the uncapped film would have a magnetic moment of  $0.87\mu_B/\text{atom}$  while the capped one would have  $0.68\mu_B/\text{atom}$ .

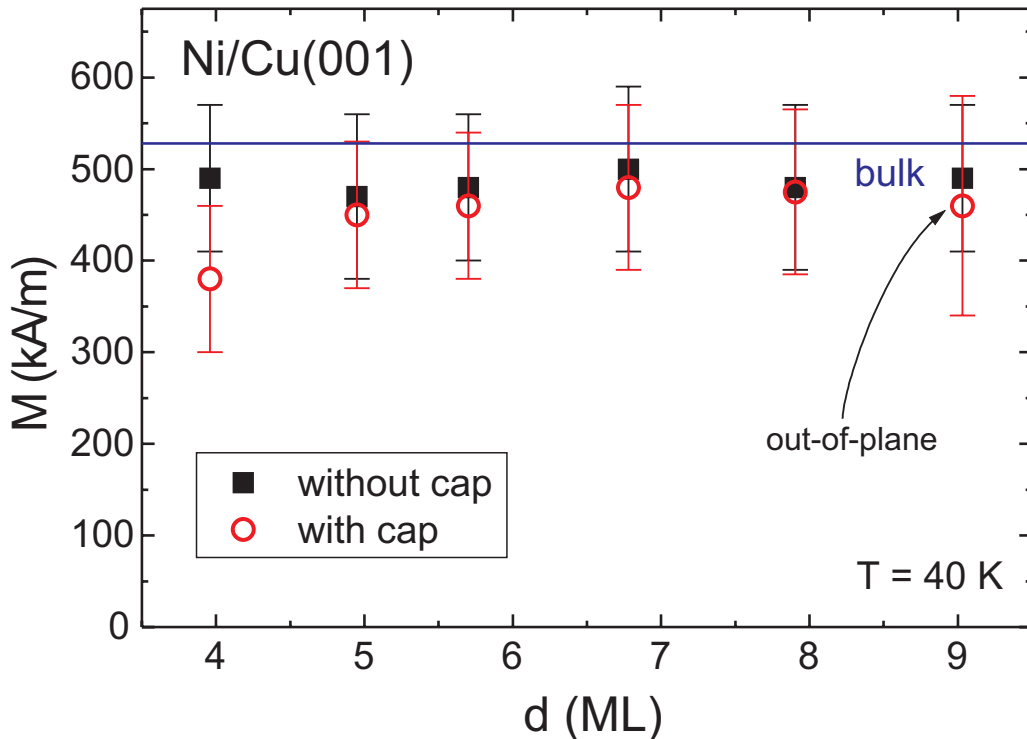


**Figure 5.4:** Summary of the first results on Ni/Cu(001) for capped and uncapped films [150]. The effect of capping is negligible above 5 ML. The magnetization of the 4 ML film is affected by about 20% due to a 5 ML Cu cap. Effects for  $T_C$  were not corrected. All films exhibit almost bulk-like magnetization with a slight reduction.

All measurements on Ni/Cu(001) films are summarized in Fig. 5.4 [150]. The circles correspond to the capped films, the squares represent uncapped films at 40 K. The influence of a Cu cap is negligible between 5 and 9 ML and increases to 20% at 4 ML film-thickness. It is obvious that all films exhibit a bulk-like magnetization if they are uncapped. The main message of Fig. 5.4 is that the magnetic moment of Ni films between 4 and 9 ML (below the reorientation transition) is not reduced to the extent reported in [47] which is consistent with more recent findings of theory [149] and experiment [62]. Besides that the measurements of Ni/Cu(001) reveal the first stray field distribution for an out-of-plane magnetized film shown in Fig. 5.1.

In summary, the results on Cu-capped and uncapped Ni/Cu(001) films are in agreement with recent findings of FMR [146] and MOKE [145] concerning the orientation of the magnetization. A bulk-like magnetization for the uncapped films between 4 and 9 ML is found which supports recent experiments using XMCD [62, 152] and calculations for the total moment [149]. The effect of Cu capping is almost negligible above 5 ML. This is well-understood since the effect of

a capping layer should contribute like  $1/d$ . At 4 ML there is a reduction due to the Cu cap of 21% which is more pronounced than theoretically predicted (11.4%) [149]. Since it has been demonstrated that there are no principle obstacles to measure Ni films with in- and out-of-plane anisotropy, i.e. cooling capabilities and sensitivity are sufficient, one can await further experimental results for the Ni/Cu(001) which go beyond these first experiments.

# Conclusion and outlook

In this work the set-up of a novel UHV compatible high- $T_C$  SQUID magnetometer has been described. It offers the possibility to measure *in situ* in UHV the magnetization with high accuracy ( $\sim 5\%$ ) and submonolayer sensitivity ( $\leq 0.3$  ML of Co) within few minutes. The sample temperature can be ranged from 40 to 300 K and standard UHV-preparation and characterization techniques can easily be applied since usual UHV equipment for the sample manipulation is used. The calibration of the magnetometer is independent of the studied magnetic material and is achieved with the help of a calibrating coil applying Biot-Savart's law. In that sense the magnetometer provides absolute values of the measured magnetization.

Thickness and temperature dependent measurements of ultrathin Co/Cu(001) films demonstrate the performance of the magnetometer, the reliability and reproducibility of the derived results. A complete set of ground-state magnetic moments has been revealed bridging between earlier work on thick films and more recent results on 2 ML. The outcome is a bulk-like magnetic moment of  $1.73(7) \mu_B/\text{atom}$  for films thicker than 8 ML and a by 10% enhanced moment of  $1.89(8) \mu_B/\text{atom}$  at 2 ML. The increase of the magnetic moment follows a linear behavior with respect to the inverse film thickness. This suggests that the enhancement is a combined surface/interface effect. The measured total magnetic moment is deconvoluted into spin and orbital contribution using former XMCD measurements of the ratio of the moments. The observed enhancement of the total magnetic moment can be attributed to an increase of the orbital moment by a factor of two. This can be understood in terms of significant unquenching of the orbital moment due to the reduced symmetry at the film surface, i.e. lower coordination number of the surface atoms. The surface and the interface contribution could be separated by measuring the Co films before and after capping with a Cu protective layer. This results in a moment profile for Co films on Cu(001) with bulk-like inner layers ( $1.73 \mu_B/\text{atom}$ ), a strongly enhanced surface moment of  $2.28(8) \mu_B/\text{atom}$ , and a pronounced reduction at the interface ( $1.43(5) \mu_B/\text{atom}$ ). The findings are consistent with recent theoretical calculations.

Due to the high sensitivity and the access to low temperatures the novel UHV-SQUID permits to study metastable magnetic properties below 2 ML of

Co/Cu(001) as well. These are discussed with respect to a recent theoretical total energy calculation and an STM study. A phase separation of Co and Cu caused by the annealing process is the suggested model.

In a second step the experiments have been extended to Ni/Cu(001). Only first results are available which indicate that the films between 4 and 9 ML are more or less magnetized like the bulk (528 kA/m). The influence of a Cu cap is negligible above 5 ML film-thickness whereas there is 20% reduction of the magnetization at 4 ML. A first measurement of an out-of-plane magnetized film is presented as well. Orientation and value of the derived magnetizations are in agreement with recent experimental and theoretical findings. Besides these first findings it could be shown that the magnetometer is not restricted to Co and that there is sufficient sensitivity to study even ultrathin Ni films.

For future experiments the possibility to monitor the magnetic properties *in situ* permits to study the influence of the preparation conditions on the magnetization. It is known that 2 ML Co films grown on a N<sub>2</sub> sputtered Cu(001) crystal forms Co dots or wires [153]. These films should exhibit a higher magnetic moment compared to a flat film due to the increased number of low-coordinated surface and step-edge atoms. For Ni it was observed recently by FMR that in the case of a pre-oxidized Cu(001) crystal O<sub>2</sub> acts as a surfactant leading to drastic changes in the magnetic anisotropy [146]. The UHV-SQUID may enable measuring the magnetization of these films. It is also possible to change the magnetic properties of Ni films by reconstructing the Ni surface with carbon [154, 155]. These examples may demonstrate that there is a large variety of interesting future measurements using the novel UHV-SQUID.

In competition with established techniques like AGM or TOM the UHV-SQUID can not offer access to field dependent studies and therefore anisotropies. On the other hand, it has the ability to reach low temperatures down to 40 K and permits fast and highly sensitive experiments. Moreover, the design of the magnetometer enables compatibility with other measuring techniques and it was designed to fit UHV chambers used for ferromagnetic resonance (FMR) studies, XMCD, MOKE, or STM. Since the magnetometer is quite cost-effective there is the potential to use it as a standard magnetometric technique for magnetic characterization of as-grown samples or as a calibrating reference for MOKE or FMR. In combination with XMCD measurements on the same film the validity of the sum-rule analysis for ultrathin films may be checked. An indirect proof has already been given in the present work. In summary, the above discussed features of the UHV-SQUID magnetometer make this machine promising for a large number of applications in the field of ultrathin film magnetometry.

# Appendix A

## Drawings of the Magnetometer

In the following pages the drawings of relevant parts of the magnetometer are given. They may serve as a reference to rebuilt the UHV-SQUID magnetometer in its present form. The dewar (Fig. A.1), the  $\mu$ -metal screening (Fig. A.2) and the glass finger (Fig. A.3) are shown. Figure A.3 also indicates how the pieces are put together to result in a sufficiently screened dewar to run a high- $T_c$  SQUID magnetometer inside an UHV chamber. In Fig. A.4 the two mounting Cu parts of the sample holder are shown.

The dewar is made of non-magnetic stainless steel according to Fig. A.1 by the workshop of the Physics Department of the FU-Berlin. While the CF 35 rotateable flange and the KF 16 pumping flange for the isolating vacuum are commercially available (Leybold), the CF 16 flange at the end of the dewar had to be self-built. The dewar provides the possibility to run the high- $T_c$  SQUID in combination with an UHV chamber. One filling of liquid nitrogen is sufficient for about 1 to 2 hours. The mounted glass finger tip (Fig. A.3), i.e. a glass-to-metal transition welded to a CF 16 flange, is also commercially available (Varian, MDC Caburn, etc.) but has to be modified. The glass tube is cut under an angle of  $55^\circ$  and the end is sealed with a flat piece of suitable glass (Pyrex, Duran, etc.). This has been done by H. Müller, glasblower in Adlershof, Berlin. The best choice for the glass-to-metal transition turned out to be Pyrex to Kovar as it can stand best the temperature gradients which occur during the  $\text{LN}_2$  filling and the bake-out.

The  $\mu$ -metal shielding was fabricated by Magnetic Shield Ltd., England following Fig. A.2. It is crucial for sufficient shielding of fluctuating magnetic fields that the shielding has at least a double wall and – as a rule of thumb – the length of the shielding is more than three times longer than its diameter. The slit for the sample should be as small as possible. In the present set-up it is  $(4 \times 8)$  mm<sup>2</sup>. For larger holes it could be necessary to surround the slit with a small  $\mu$ -metal cylinder.

## A.1 The UHV-compatible metal dewar

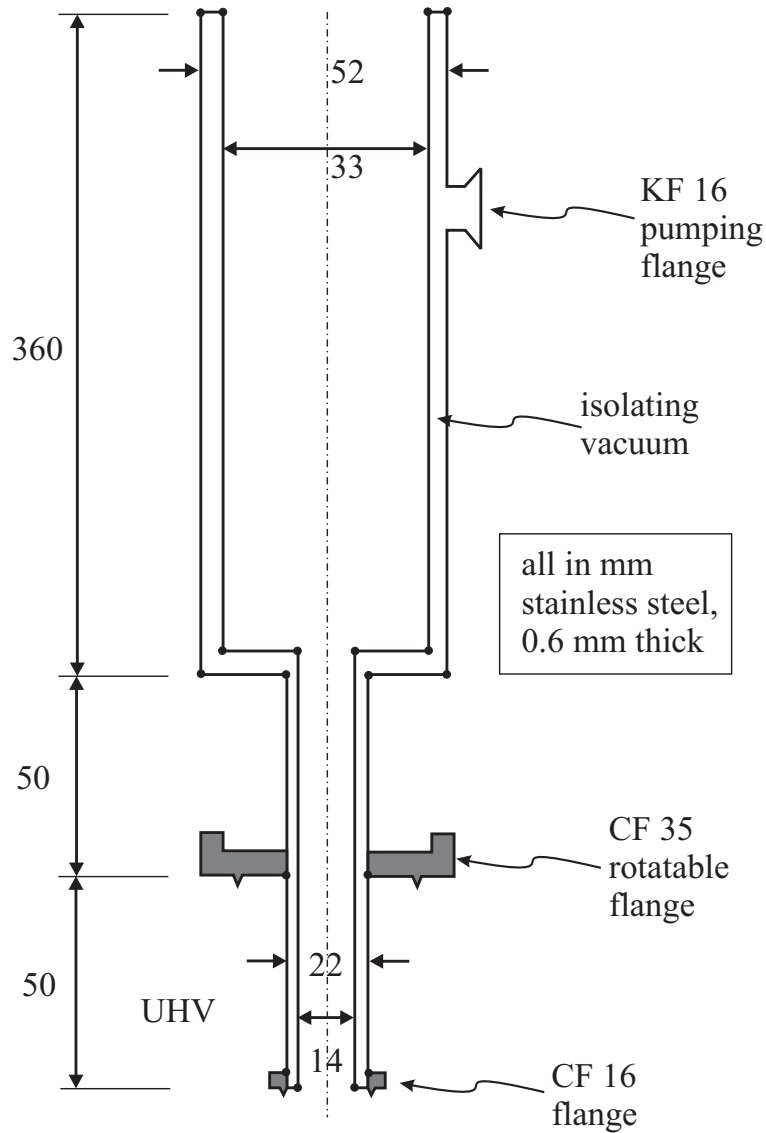


**Figure A.1:** Detailed drawing of the metal dewar to keep the SQUID under liquid nitrogen.

The metal dewar is made of “non-magnetic” stainless steel. The isolating vacuum is pumped down to about  $10^{-5}$  mbar. Since the glass finger, which is attached to the CF 16 flange, has only a single wall there is thermal contact via the outer wall of the dewar towards the CF 35 flange. To minimize the loss of cooling power the CF 35 flange should be surrounded with thermal isolating material like Styropor and Al-foil.

## A.2 The $\mu$ -metal shielding

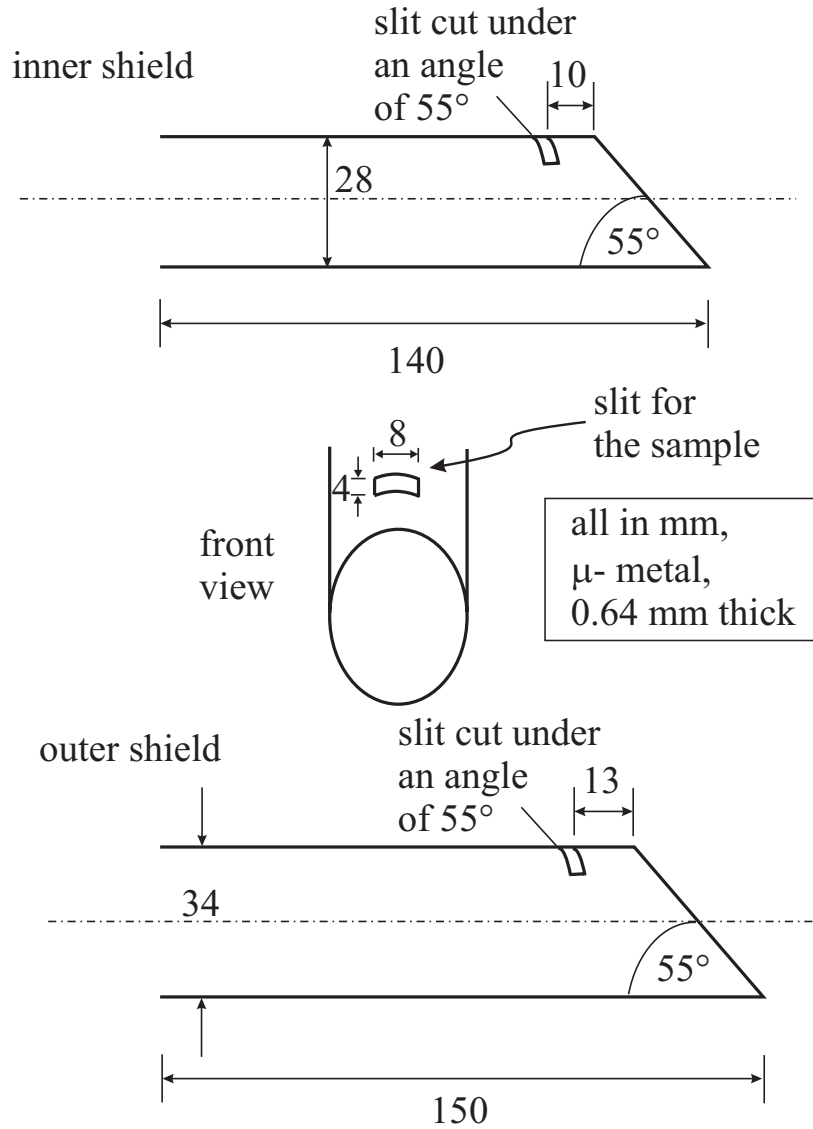


**Figure A.2:** Detailed drawing of the  $\mu$ -metal shielding.

The two parts of the  $\mu$ -metal shielding are assembled according to Fig. A.3 yielding a double shielding which fits inside a CF 35 flange. Since the cylinders are in contact with the wall of the glass finger they are cooled down by the liquid nitrogen and, therefore, they serve not only as a magnetic, but also as a thermal (radiation) shielding for the sample.

### A.3 The glass finger tip

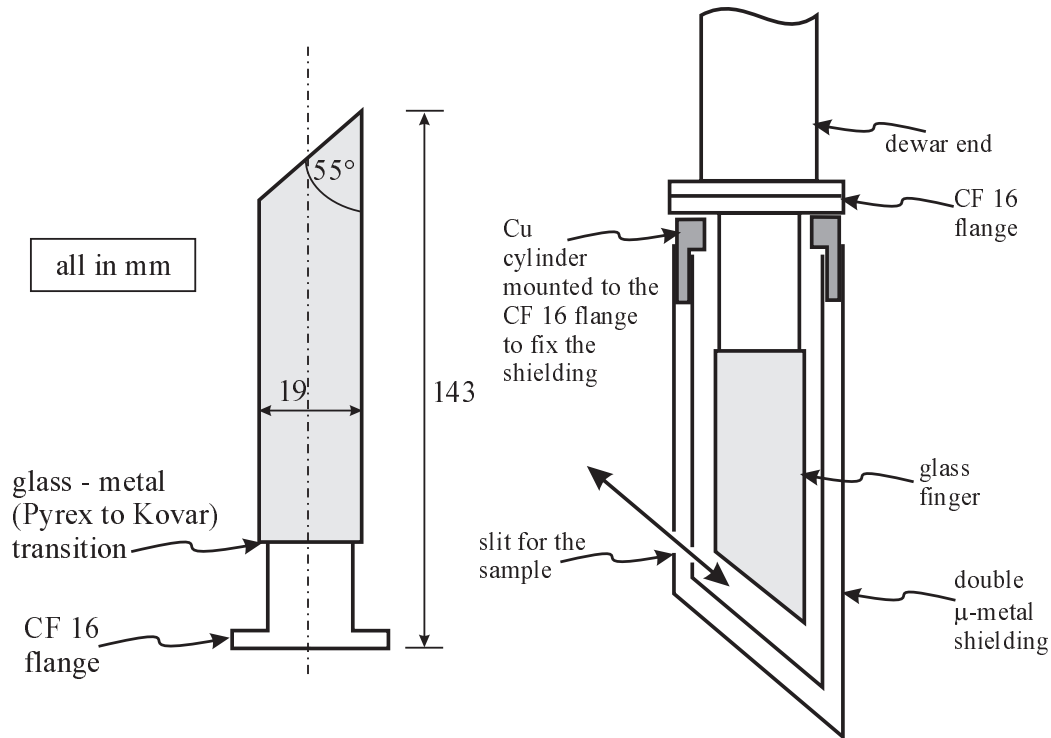


**Figure A.3:** The glass finger tip and sketch of use. The double  $\mu$ -metal shielding is mounted with a Cu cylinder at the CF 16 flange of the glass finger.

The  $\mu$ -metal shielding is mounted with a Cu cylinder which, on one side, fits in between the cylinders and, on the other side, is mounted with the help of two M2 screws drilled inside two of the M4 screws of the CF 16 flange connecting glassfinger and dewar. This allows to design different glassfinger tips with a suitable shielding which can be used with the same dewar. An elongation of the vacuum-side of the dewar with a standard CF 16 extension tube is possible depending on the geometry of the vacuum chamber used.

### A.4 The sample holder (parts)

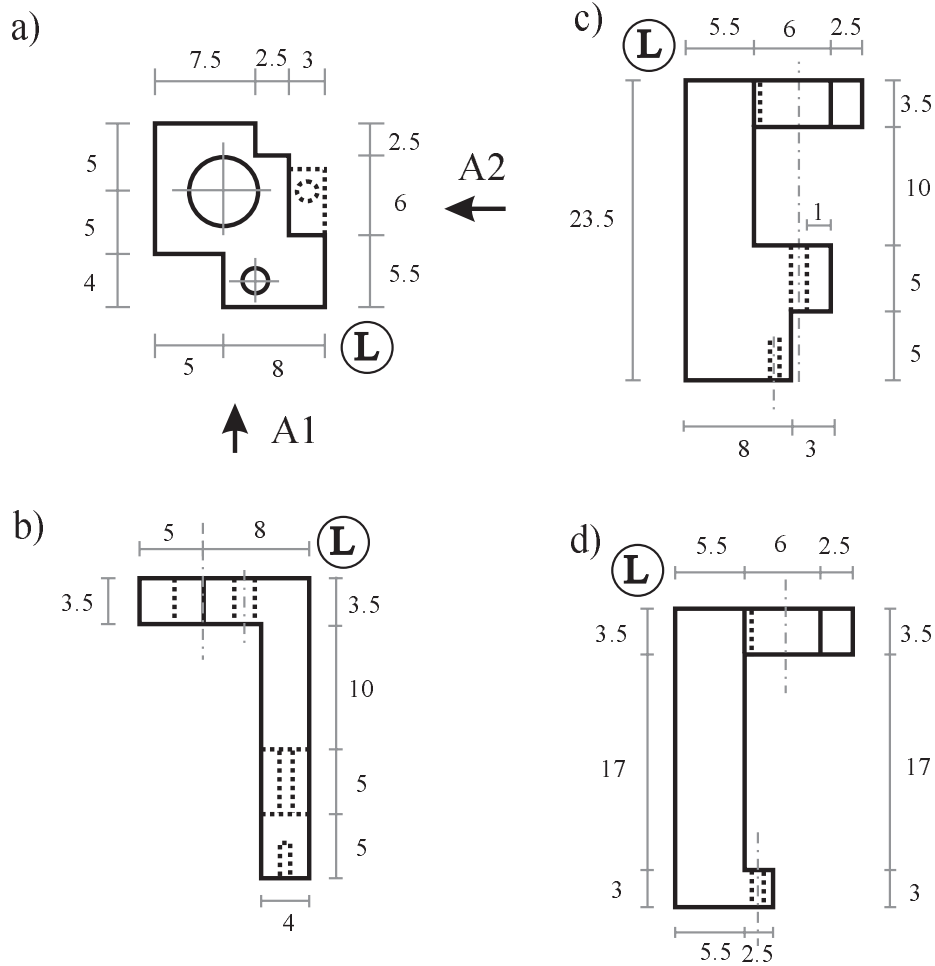


**Figure A.4:** Details of the parts of the sampleholder which allows electrically isolated mounting of the Cu tubes and the thermocouple ceramics. The mounting consists of two parts. Its top view is given in a), The diameter of the holes is 5 mm and 1.5 mm respectively. The side view (direction A1) is given by b). The front view (direction A2) is given by c) for the part with thermocouple holder and by d) for the one without.

The two parts of the sample holder can be put together in a “T”-shaped way (see Fig. 3.3). They are electrically isolated with respect to each other. Each part is mounted with a screw and an isolating ceramic to the cryostat of the manipulator. The small hole at the bottom of each part serves for the mounting of the Cu tubes. The part sketched in c) provides an additional hole for the ceramic of the thermocouple. The small hole in a) serves for the electrical connection to enable resistive heating of the sample.

# Appendix B

## Motor control unit

The magnetic stray-field of the sample is recorded with the help of a computer. The necessity to determine the distance between SQUID and sample by fitting the shape of the stray field distribution requires high density of the measured data points. A motor control unit was designed to provide the following features:

- bisection of the SQUID output voltage ( $\pm 10 \text{ V} \rightarrow \pm 5 \text{ V}$ )
- bipolar power supply for the manipulator motor
- power supply for the trigger light barrier
- reduction of the trigger-signal by factors of 8, 16, 32, etc.
- control of the motor by both, manual switch and computer (up  $\leftrightarrow +5 \text{ V}$ , halt  $\leftrightarrow 0 \text{ V}$ , down  $\leftrightarrow -5 \text{ V}$ )
- end switches to limit the range of motion of the manipulator

The motor control unit was built by our group engineer W. Wisny. The three main parts of the unit are shown in Figs. B.1, B.2 and B.3. Figure B.4 sketches the plug assembly for the tree connecting cables indicated in Fig. 3.5. This Figure shows the block diagram of the computer aided data acquisition.

### B.1 Main power supply

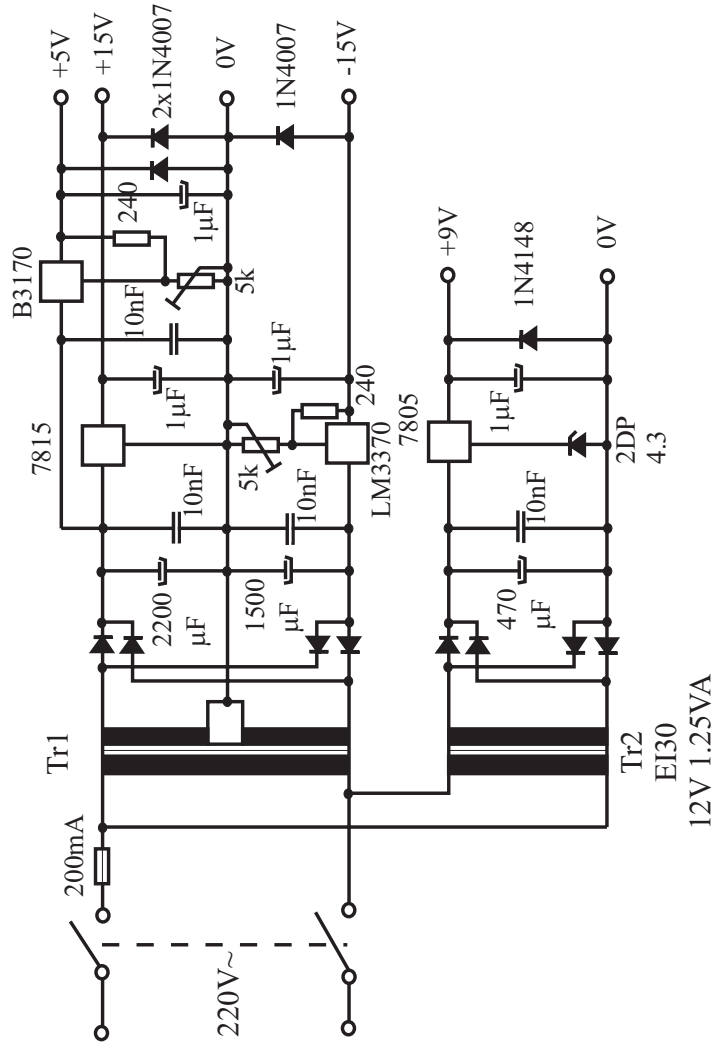


**Figure B.1:** The main power supply of the motor control unit is given for completeness. It provides the voltages necessary for the operation of the motor, the trigger unit, and the OP of the voltage bisection.

## B.2 Bipolar power supply for the motor drive

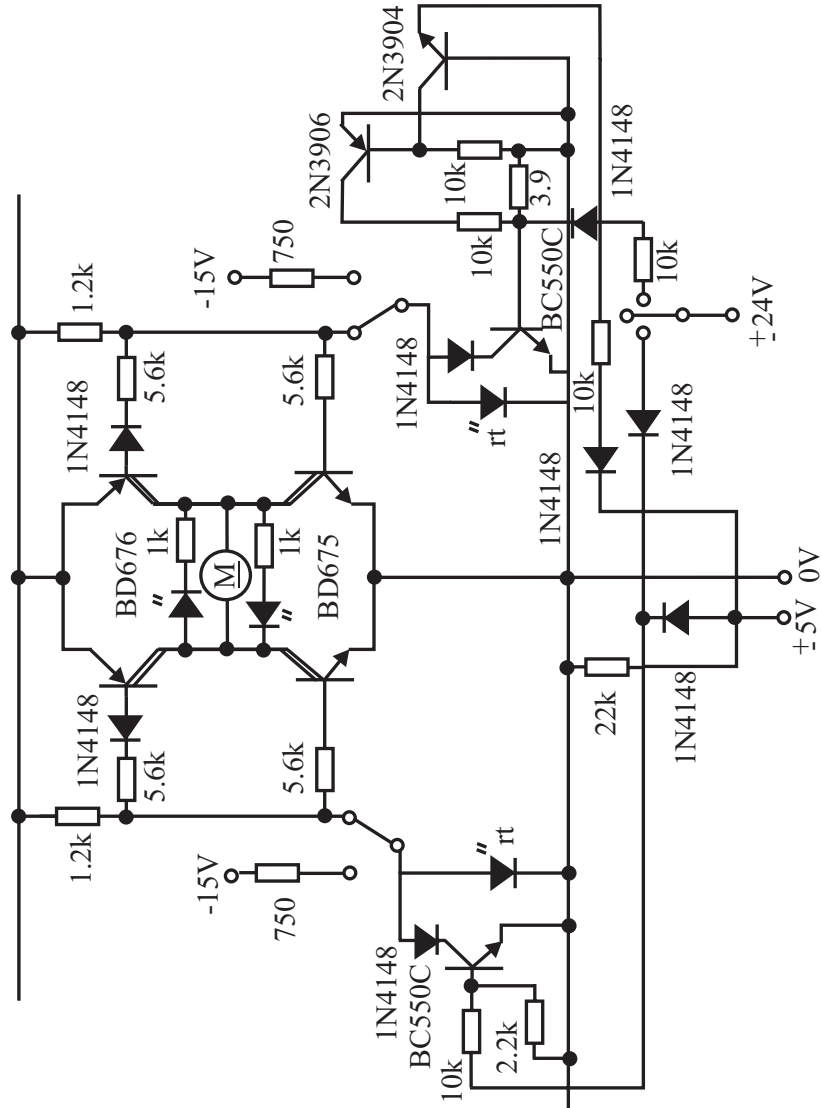


**Figure B.2:** The bipolar power supply for the manipulator motor “M”.

Applying a voltage of  $\pm 5$  V (right side, middle) drives the motor up or down to allow external control by a computer. The switch on the right side ( $\pm 24$  V) enables driving the manipulator manually. The two switches in the middle part of the drawing are the end-switches sketched in Fig. 3.5.

### B.3 Trigger unit and voltage bisection

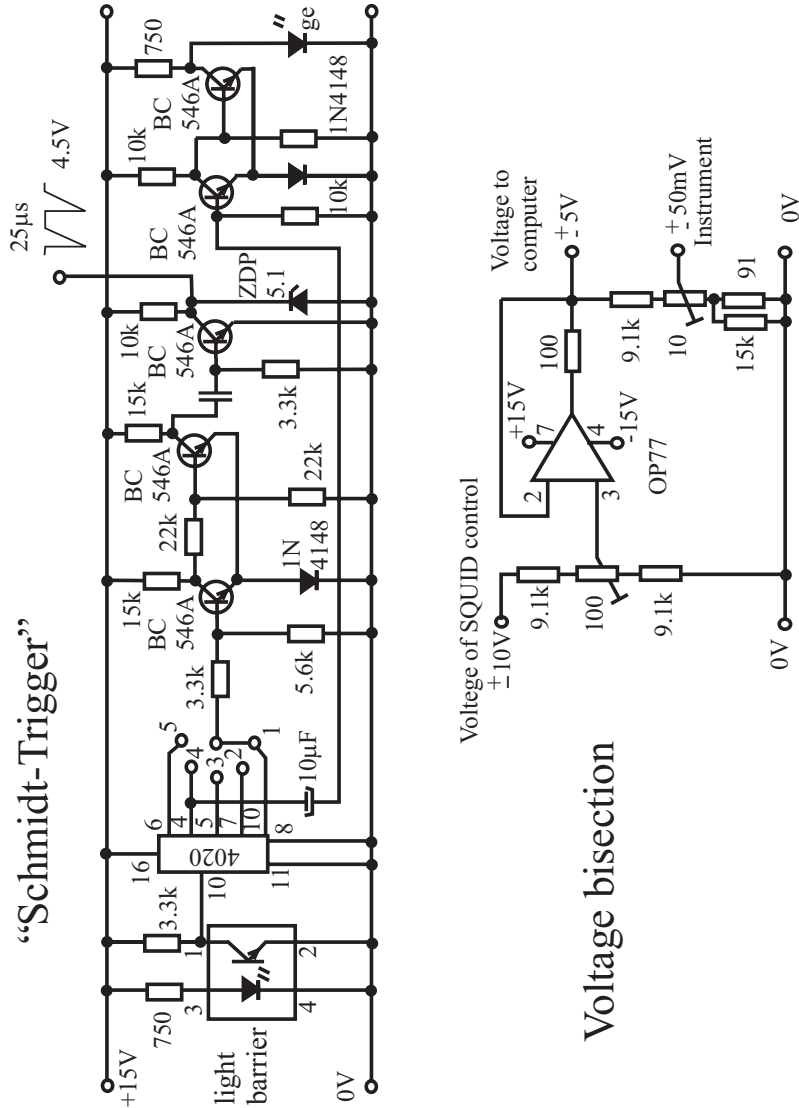
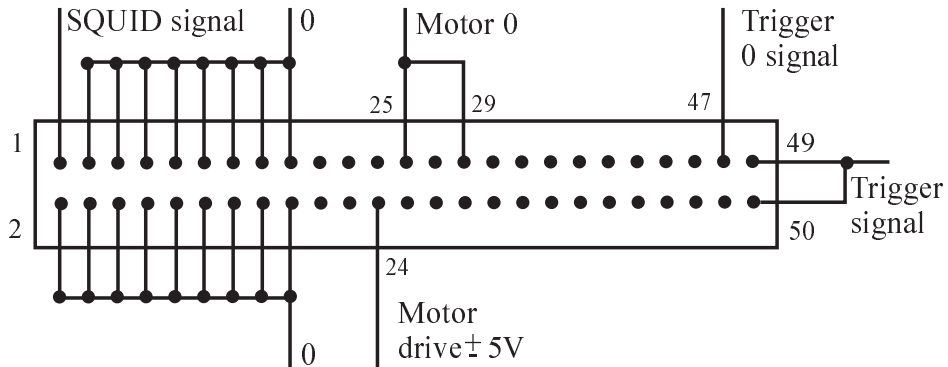


**Figure B.3:** Trigger unit and voltage bisection.

In the lower part of the trigger unit the light barrier is shown which is interrupted by a disk mounted on the axis of the manipulator motor. The IC (4020) provides the possibility to divide the incoming pulses by factors of 8, 16, 32, etc. which can be chosen by the switch indicated right above the IC. The output is sketched on the upper left part: The pulses are  $25 \mu\text{s}$  broad and have a voltage difference of 4.5 V. This shape is according to the requirements of the "clock" input of the AD-DA card.

## B.4 Plug assembly

cable between motor control and computer (50 pin):



cable between motor control and motor (15 pin):

1. up LED
2. up end LED
3. down LED
4. down end LED
5. motor (+)
6. motor (-)
7. trigger diode (+)
8. trigger(+)
9. up LED (-)
- 10.
11. down LED (-)
- 12.
- 13.
- 14.
15. trigger (-)

cable to manipulator (7 pin):

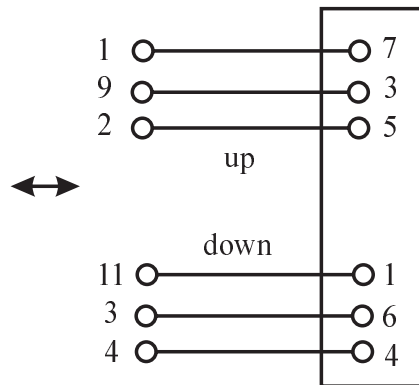


**Figure B.4:** The plug assembly of the three connecting wires.

# Appendix C

## Computer programs

### C.1 Programs to calculate the stray field

This short Fortran90 program calculates the  $z$  component of the magnetic stray field of an in-plane magnetized film according to the analytical solution of eq. (3.4). The obtained data sets were used to fit the measured ones.

```
      program strayfieldsimulation

      double precision h,M,xstep,xinter,u,b,var1,var2,zaehl,nenn
      double precision a,feld,am,bm,hm,xinterm,xstepm,zaehl2,d
      character datei*15

c Eingabe Parameter

      print *, 'Ausgabefile: '
      read '(a)', datei
      print *, 'Hoehe h in mm '
      read *, hm
      print *, 'Magnetisierung in Gauss'
      read *, M
      print *, 'x-Schrittweite in mm'
      read *, xstepm
      print *, 'x-Intervall in mm'
      read *, xinterm
      print *, 'Probengroesse in mm (x)'
      read *, am
      print *, 'Probengroesse in mm (y)'
      read *, bm
      print *, 'Probendicke in ML'
```

```

      read  *, d

      h=hm/1000
      a=am/1000
      b=bm/1000
      xstep=xstepm/1000
      xinter=xinterm/1000

      open(1, file=datei, status='unknown')

c Laufvariable setzen

      do u=-xinter,xinter,xstep
      var1=(4*u**2+4*u*a+a**2+b**2+4*h**2)**0.5
      var2=(4*u**2-4*u*a+a**2+b**2+4*h**2)**0.5
      zaehl=(4*var1*u**2-4*var2*h**2+4*var1*u*a+var1*a**2+
      ;4*var1*h**2-4*var2*u**2+4*var2*u*a-var2*a**2)
      nenn=(4*u**2-4*u*a+a**2+4*h**2)*var2*
      ;(4*u**2+4*u*a+a**2+4*h**2)*var1
      feld=0.0001416*d*h*M*b*(zaehl/nenn)
      write (1,*) u*1000,feld
      enddo

      close(1)
      end

c -----END PROGRAM-----

```

The following program is to calculate the stray field for an out-of-plane magnetized film. For this topic it is more convenient to solve the integral numerically. It is important to choose the variable for "Integrationsintervall" called "intervall"  $\leq 10^{-4}$  to calculate a proper value of the integral.

This program can be used for an in-plane magnetized film as well. The only changes required are to replace the line of the following program reading

```
integral=integral+intervall**2*(3*h**2/r**5-1/r**3)
```

by

```
integral=integral+intervall**2*(u-x)/r**5
```

and the line

```
feld=M*d*1.77/100000*integral
```

by

```
feld=3*h*M*d*1.77/100000*integral
```

Both, analytical and numerical solution calculate exactly the same stray field distribution for an in-plane film.

```
program outofplanestrayfield
```

```
double precision h,M,xstep,xinter,u,b,x,y,v
double precision a,feld,am,bm,hm,xinterm,xstepm,d
double precision intervall,integral,r,pi
```

```
character datei*15
```

c Eingabe Parameter

```
print *, 'Ausgabefile: '
read '(a)', datei
print *, 'Hoehe h in mm '
read *, hm
print *, 'Magnetisierung in Gauss'
read *, M
print *, 'x-Schrittweite in mm'
read *, xstepm
print *, 'x-Intervall in mm'
read *, xinterm
print *, 'Probengroesse in mm (x)'
read *, am
print *, 'Probengroesse in mm (y)'
read *, bm
print *, 'Probendicke in ML'
read *, d
```

```

print *, 'Integrationsintervall'
read *, intervall

pi=3.141592654
h=hm/1000
a=am/1000
b=bm/1000
xstep=xstepm/1000
xinter=xinterm/1000
integral=0
v=0

open(1, file=datei, status='unknown')

```

c Laufvariable setzen

```

do u=-xinter,xinter,xstep
  do x=-a/2,a/2,intervall
    do y=-b/2,b/2,intervall
      r=((u-x)**2+y**2+h**2)**(.5)
      integral=integral+intervall**2*(3*h**2/r**5-1/r**3)
    enddo
  enddo
  feld=M*d*1.77/100000*integral
  write (1,*) u*1000,feld
  integral=0
enddo

close(1)
end

```

c -----END PROGRAM-----



```
{
    unsigned char low, high;
    low  = inportb(ad_dac0l);
    high = inportb(ad_dac0h);
    *dum = (high << 8) + low;
}

void Set_CsrGcr(unsigned int csr, unsigned int gcr, unsigned int tmr)

{
    outport(ad_csr, csr);
    outport(ad_tmr, tmr);
    outport(ad_gcr, gcr);
}

void init_ad(unsigned int *csr)
{
    outport(ad_dio, 0x0);
    outport(ad_csr, 0x0);
    delay(100);
    Get_dac0(&dum);
    *csr = 0x3;
}

void Wait_For_AD(void)
{
    unsigned char csr;
    do
    {
        csr = inport(ad_csr);
    }
    while(csr < 0x80);
}

void Set_dac(unsigned int wert1 ,unsigned int wert2)
/* DA Cannel 1 mit Wert besetzen */
{
    outportb(ad_dac1l, (wert1));
    outportb(ad_dac1h, (wert2));
}

void Read_Channel0(unsigned int *dum)
{
```

```
    Wait_For_AD();
    Get_dac0(dum);
}

void Motor (char drive)
{
    unsigned int wert1;
    unsigned int wert2;

    switch (drive)
    {
        case 'd': wert1 = 255;
                 wert2 = 255;
                 break;
        case 'u': wert1 = 0;
                 wert2 = 0;
                 break;
        case 's': wert1 = 0;
                 wert2 = 8;
                 break;
    }

    Set_dac (wert1 , wert2);
}

/*>>>>>>>> AD-DA-Wandlerdefinition ENDE>>>>>>>>*/
```

The listing below shows the control-program itself. The maximum recordable number of data points is 4000. The name of the output file may be specified, the number of recorded data-points, and the reduction-factor of the trigger. The chosen conversion mode of the ADC is “continuous conversion, external trigger and oscillator” defined by the first number in the command “Set\_CsrGcr(0x3, 0x0, 0x0);”. The second number specifies a gain of 1 of the active read-out channel #0. The last number sets the divisor of the “clock” to “1”. After initialization the manipulator is driven up by the required number of steps and down again while recording the output voltage of the SQUID upon each triggering signal of the motor control unit. Then, the data are written to the specified file (ASCII format). The numbers correspond to the real output voltage of the SQUID, i.e. they are multiplied by 2 and the number of turns of the motor is translated into mm (125 turns of the motor correspond to 1 mm, the reduction factor of the trigger unit is taken into account as well).

```

/*-----Squidsteuerprogramm, Version 1.0 -----*/

#include <stdio.h>
#include "C:\AD_DA4.C"

/* Beginn Hauptprogramm */
main()
{
    int step;
    int um;
    int umd;
    int divisor;
    char drive;
    unsigned int dum;
    unsigned int mess1[4000];
    unsigned int mess2[4000];
    double x, y;

    char filename[12];

    FILE *ausgabe;          /* init. file */
    char *aus_datei;       /* name file */

    printf("Abspeichern unter? (max. 12 Zeichen) \n");
    scanf("%s", filename);
    aus_datei = filename;
    ausgabe=fopen(aus\_datei,"w");

```

```

/* initialize card */
define_ad();
init_ad(&csr);

/* Eingabe der Parameter */
printf("Geben Sie die Zahl der Schritte an (max. 4000) \n");
scanf("%d",&step);
printf("Teilereinstellung des Triggers? \n");
scanf("%d",&divisor);

/* Beginn Durchlaufschleife */
Set_CsrGcr(0x3, 0x0, 0x0);
drive = 'u';
Motor(drive);          /* Motor ansteuern (hoch) */

/* Beginn Schrittschleife (hoch) */
for(um = 1 ; um <= step ; um++)
{
    Read_Channel0(&dum);          /* Kanal auslesen */
    mess1[um-1] = dum;
}
    outport(ad_csr , 0x0);
drive = 's';
Motor(drive);          /* Motor ansteuern (halt) */

for(um = 1 ; um <= step ; um++)
{
    x = um * divisor / 125.;
    y = (mess1[um-1] - 2048.) / 2048. * 10.;
    fprintf(ausgabe," %e " , x);    /* File schreiben */
    fprintf(ausgabe, " %e \n", y);
}
delay(2000);

Set_CsrGcr(0x3, 0x0, 0x0);
drive = 'd';
Motor(drive);          /* Motor ansteuern (ab) */

/* Beginn schrittschleife (ab) */
for(um = 1 ; um <= step ; um++)
{
    umd = step - um +1;

```

```
        Read_Channel0(&dum);      /* Kanal auslesen */
        mess2[umd-1] = dum;
    }
    outport(ad_csr , 0x0);
    drive = 's';
    Motor(drive);      /* Motor ansteuern (halt) */

    for(um = 1 ; um <= step ; um++)
    {
        x = um * divisor / 125.;
        y = (mess2[um-1] - 2048.) / 2048. * 10.;
        fprintf(ausgabe," %e " , x);      /* File schreiben */
        fprintf(ausgabe, " %e \n", y);
    }
    delay(2000);

    fclose (ausgabe);      /* close file */
    return;
}

/*>>>>>>>>> CARD CONTROL PROGRAM END>>>>>>>>>*/
```

# Bibliography

- [1] N. D. Mermin and H. Wagner, *Phys. Rev. Lett.* **17**, 1133 (1966)
- [2] D. L. Mills, *J. Magn. Magn. Mater.* **100**, 515 (1991)
- [3] H. J. Elmers, *Int. J. Mod. Phys.* **9**, 3115 (1995)
- [4] J. A. C. Bland and B. Heinrich, eds., *Ultrathin Magnetic Structures*, Vol. I and II, Springer Verlag, Berlin (1994)
- [5] B. D. Josephson, *Phys. Rev. Lett.* **1**, 251 (1962)
- [6] A. Barone and G. Paterno, eds., *Physics and Application of the Josephson Effect*, Wiley, New York (1982)
- [7] J. Clarke, *SQUID concepts and systems*, in *Superconducting electronics*, eds. H. Weinstock and M. Niesenoff, NATO ASI, pp. 87–148, Springer Verlag, Berlin (1989)
- [8] U. Gradmann, *Magnetism in Ultrathin Transition Metal Films*, in *Handbook of Magnetic Materials*, ed. K. H. J. Buschow, Vol. 7, pp. 1–96, Elsevier Science Publishers, Amsterdam (1993)
- [9] C. Kittel, *Einführung in die Festkörperphysik*, R. Oldenbourg Verlag, München, Wien (1999)
- [10] M. B. Stearns, *Properties of Magnetic Materials*, in *Landolt Börnstein*, ed. H. P. J. Wijn, Vol. 19a of *New Series Group III*, Springer Verlag, Berlin (1986)
- [11] A. Abragam and B. Bleaney, *Electron Paramagnetic Resonance of Transition Ions*, Clarendon Press, Oxford (1970)
- [12] S. A. Al'tshuler and B. M. Kozyrev, *Electron Paramagnetic Resonance*, Academic Press, New York (1964)
- [13] D. Jiles, *Introduction to Magnetism and Magnetic Materials*, Chapman and Hall, London (1991)

- [14] M. Weinert and A. J. Freeman, *J. Magn. Magn. Mater.* **38**, 23 (1983)
- [15] A. Freeman and R. Wu, *J. Magn. Magn. Mater.* **104 - 107**, 1 (1992)
- [16] M. Albrecht, U. Gradmann, T. Furubayashi and W. A. Harrison, *Europhys. Lett.* **20**, 65 (1992)
- [17] E. Bergter, U. Gradmann and R. Bergholz, *Solid State Commun.* **53**, 565 (1985)
- [18] K. Wagner, N. Weber, H. J. Elmers and U. Gradmann, *J. Magn. Magn. Mater.* **167**, 21 (1997)
- [19] R. Feder, S. F. Alvarado, E. Tamura and E. Kiesker, *Surf. Sci.* **127**, 83 (1983)
- [20] G. A. Mulhollan, A. R. Köymen, D. M. Lind, F. B. Dunning, G. K. Walters, E. Tamura and R. Feder, *Surf. Sci.* **204**, 503 (1988)
- [21] E. Tamura, R. Feder, G. Waller and U. Gradmann, *Phys. Stat. Solidi (b)* **157**, 627 (1990)
- [22] A. Ormeci, B. M. Hall and D. L. Mills, *Phys. Rev. B* **44**, 12369 (1991)
- [23] J. Shen, R. Skromski, M. Klaua, H. Jenniches, S. S. Manoharan and J. Kirschner, *Phys. Rev. B* **56**, 2340 (1997)
- [24] J. Hauschild, H. J. Elmers and U. Gradmann, *Phys. Rev. B* **57**, R677 (1998)
- [25] J. Hauschild, U. Gradmann and H. J. Elmers, *Appl. Phys. Lett.* **72**, 3211 (1998)
- [26] L. Szunyogh, B. Újfalussy, C. Blaas, U. Pustogowa, C. Sommers and P. Weinberger, *Phys. Rev. B* **56**, 14036 (1997)
- [27] O. Hjortstam, J. Tyregg, J. M. Willis, B. Johansson and O. Eriksson, *Phys. Rev. B* **53**, 9204 (1996)
- [28] A. J. Freeman and R. Wu, *J. Magn. Magn. Mater.* **200**, 498 (1999)
- [29] G. A. T. Allan, *Phys. Rev. B* **1**, 352 (1970)
- [30] R. Bergholz and U. Gradmann, *J. Magn. Magn. Mater.* **45**, 389 (1984)
- [31] J. Korecki, M. Przybylski and U. Gradmann, *J. Magn. Magn. Mater.* **89**, 325 (1990)
- [32] W. Döring, *Z. Naturforsch.* **16a**, 1146 (1961)

- [33] R. P. Erickson and D. L. Mills, *Phys. Rev. B* **46**, 861 (1992)
- [34] P. Bruno, *Phys. Rev. B* **39**, 865 (1989)
- [35] S. Chikazumi, *Physics of Ferromagnetism*, Oxford Science Publications, Oxford (1997)
- [36] C. Kittel, *Phys. Rev.* **76**, 743 (1949)
- [37] A. N. Anisimov, M. Farle, P. Pouloupoulos, W. Platow, K. Baberschke, P. Isberg, R. Wäppling, A. M. N. Niklasson and O. Eriksson, *Phys. Rev. Lett.* **82**, 2390 (1999)
- [38] R. M. Moon, *Phys. Rev. A* **136**, 195 (1964)
- [39] K. Ayuel and P. F. de Châtel, *Phys. Rev. B* **61**, 15213 (2000)
- [40] B. T. Thole, P. Carra, F. Sette and G. van der Laan, *Phys. Rev. Lett.* **68**, 1943 (1992)
- [41] P. Carra, B. T. Thole, M. Altarelli and X. Wang, *Phys. Rev. Lett.* **70**, 694 (1993)
- [42] J. Kanamori, *Anisotropy and Magnetostriction of Ferromagnetic and Antiferromagnetic Materials*, in *Magnetism*, eds. G. T. Rado and H. Suhl, Vol. 1, pp. 127–199, Academic Press, New York and London (1963)
- [43] C. Cohen-Tannoudji, B. Diu and F. Laloë, *Quantum Mechanics*, Vol. II, Wiley, New York (1977)
- [44] W. L. O'Brien and B. P. Tonner, *Phys. Rev. B* **50**, 12672 (1994)
- [45] D. L. Mills, *private communication* (2000)
- [46] C. T. Chen, Y. U. Idzerda, H.-J. Lin, N. V. Smith, G. Meigs, E. Chaban, G. H. Ho, E. Pellegrin and F. Sette, *Phys. Rev. Lett.* **75**, 125 (1995)
- [47] P. Srivastava, F. Wilhelm, A. Ney, M. Farle, H. Wende, N. Haack, G. Ceballos and K. Baberschke, *Phys. Rev. B* **58**, 5701 (1998)
- [48] M. G. Samant, J. Stöhr, S. S. P. Parkin, G. A. Held, B. D. Hermsmeier, F. Herman, M. van Schilfhaarde, L. C. Duda, D. C. Mancini, N. Wassdahl and R. Nakajima, *Phys. Rev. Lett.* **72**, 1112 (1994)
- [49] D. Weller, J. Stöhr, R. Nakajima, A. Carl, M. G. Samant, C. Chappert, R. Mégy, P. Beauvillain, P. Veillet and G. A. Held, *Phys. Rev. Lett.* **75**, 3752 (1995)

- [50] J. Stöhr, *J. Magn. Magn. Mater.* **200**, 470 (2000)
- [51] M. Faraday, *Phil. Trans. R. Soc.* **136**, 1 (1846)
- [52] J. Kerr, *Phil. Mag.* **3**, 321 (1877)
- [53] S. D. Bader, *J. Magn. Magn. Mater.* **100**, 440 (1991)
- [54] U. Pustogova, W. Hübner and K. H. Bennemann, *Phys. Rev. B* **49**, 10031 (1994)
- [55] M. Farle, W. A. Lewis and K. Baberschke, *Appl. Phys. Lett.* **62**, 2728 (1993)
- [56] J. L. Erskine and E. A. Stern, *Phys. Rev. B* **12**, 5016 (1975)
- [57] G. Schütz, W. Wagner, W. Wilhelm, P. Kienle, R. Zeller, R. Frahm and G. Materlik, *Phys. Rev. Lett.* **58**, 737 (1987)
- [58] H. Ebert and G. Schütz, eds., *Spin-Orbit-Influenced Spectroscopies of Magnetic Solids*, Vol. 466 of *Lecture Notes in Physics*, Springer-Verlag, Berlin (1996)
- [59] F. Wilhelm, P. Pouloupoulos, G. Ceballos, P. Srivastava, H. Wende, K. Baberschke, D. Benea, H. Ebert, M. Angelakeris, N. K. Flevaris, D. Niarchos, A. Rogalev and N. B. Brookes, *Phys. Rev. Lett.* **85**, 413 (2000)
- [60] M. Tischer, O. Hjortstam, D. Arvanitis, J. Hunter-Dunn, F. May, K. Baberschke, J. Tyregg, J. M. Wills, B. Johansson and O. Erickson, *Phys. Rev. Lett.* **75**, 1602 (1995)
- [61] P. Srivastava, F. Wilhelm, A. Ney, H. Haack, H. Wende and K. Baberschke, *Surf. Sci.* **402 - 404**, 818 (1998)
- [62] F. Wilhelm, U. Bovensiepen, A. Scherz, P. Pouloupoulos, A. Ney, H. Wende, G. Ceballos and K. Baberschke, *J. Magn. Magn. Mater.* **222**, 163 (2000)
- [63] T. Nawrath, H. Fritzsche, F. Klose, J. Nowikow and H. Maletta, *Phys. Rev. B* **60**, 9525 (1999)
- [64] H. Fritzsche, *private communication* (2000)
- [65] T. Nawrath, H. Fritzsche and H. Maletta, *J. Magn. Magn. Mater.* **212**, 337 (2000)
- [66] P. J. Flanders, *J. Appl. Phys.* **63**, 3940 (1988)
- [67] C. Turtur and G. Bayreuther, *Phys. Rev. Lett.* **72**, 1557 (1994)
- [68] M. Zöfl, *private communication* (2000)

- [69] M. Weber, R. Koch and K. Rieder, *Phys. Rev. Lett.* **73**, 166 (1994)
- [70] M. Löhndorf, J. Moreland, P. Kabos and N. Rizzo, *J. Appl. Phys.* **87**, 5995 (2000)
- [71] T. Höpfl, D. Sander, H. Höche and J. Kirschner, *Rev. Sci. Instr.* **72**, 1495 (2001)
- [72] J. H. E. Griffiths and J. R. MacDonald, *J. Sci. Instr.* **28**, 56 (1951)
- [73] H. Fritzsche, *Struktur und Magnetismus ultradünner Eisen- und Kobalt-Epitaxieschichten*, PhD Thesis, Technische Universität Clausthal (1995)
- [74] J. Lohau, S. Kirsch, A. Carl and E. F. Wassermann, *Appl. Phys. Lett.* **76**, 3094 (2000)
- [75] J. G. Bednorz and K. A. Müller, *Z. Phys. B* **64**, 189 (1986)
- [76] D. Koelle, R. Kleiner, F. Ludwig, E. Dantsker and J. Clarke, *Reviews of Modern Physics* **71**, 631 (1999)
- [77] S. Chantraphorn, E. F. Fleet, F. C. Wellstood, L. A. Knauss and T. M. Eiles, *Appl. Phys. Lett.* **76**, 2304 (2000)
- [78] J. R. Kirtley, C. C. Tsuei, K. A. Moler, V. G. Kogan, J. R. Clem and A. J. Tuberfield, *Appl. Phys. Lett.* **74**, 4011 (1999)
- [79] W. G. Jenks, S. S. H. Sadeghi and J. P. Wikswo, *J. Phys. D: Appl. Phys.* **30**, 293 (1997)
- [80] D. P. Pappas, G. A. Prinz and M. B. Ketchen, *Appl. Phys. Lett.* **65**, 3401 (1994)
- [81] S. Spangna, R. E. Sager and M. B. Maple, *Rev. Sci. Instr.* **66**, 5570 (1995)
- [82] F.I.T. Meßtechnik GmbH, Bodenburger Str. 25/26, D-31158 Bad Salzdetfurth, Germany, *SQUID magnetometer model HM1* (1994)
- [83] N. R. Nowaczyk, H.-U. Worm, A. Knecht and J. H. Hinken, *Geophys. J. Int.* **132**, 721 (1998)
- [84] C. Rüdts, *ac Suszeptibilitätsmessungen an ultradünnen Nickel Filmen auf Wolfram(110) im Ultrahochvakuum*, Diploma thesis, Freie Universität Berlin (2000)
- [85] S.H.E. Corporation, 4174 Sorrento Valley Blvd. San Diego, CA 92121 (not existing any more), *S.H.E. Model 30, DFC Digital Flux Converter* (1981)

- [86] C. Gerthsen, *Physik*, Springer Verlag, Berlin (1977)
- [87] J. R. Kirtley, M. B. Ketchen, K. G. Stawiasz, J. Z. Sun, W. J. Gallagher, S. H. Blanton and S. J. Wind, *Appl. Phys. Lett.* **66**, 1138 (1995)
- [88] O. Snigirev, K. E. Andreev, A. M. Tishin, S. A. Gudoshnikov and J. Bohr, *Phys. Rev. B* **55**, 14429 (1997)
- [89] Omicron Vakuumphysik GmbH, Idsteiner Str. 78, D-65232 Taunusstein, Germany, *UHV evaporator EFM3* (1993)
- [90] A. Ney, *Magnetischer Röntgenzirkulardichroismus an Ein-, Zwei- und Dreifachlagen der 3d-Übergangsmetalle*, Diploma thesis, Freie Universität Berlin (1998)
- [91] M. Ritter, M. Stindtman, M. Farle and K. Baberschke, *Surf. Sci.* **348**, 215 (1995)
- [92] W. L. O'Brien, T. Droubay and B. P. Tonner, *Phys. Rev. B* **54**, 9297 (1996)
- [93] H. P. Oepen, M. Benning, H. Ibach, C. M. Schneider and J. Kirschner, *J. Magn. Magn. Mater.* **86**, L137 (1990)
- [94] S. S. P. Parkin, A. Modak and D. J. Smith, *Phys. Rev. B* **47**, 9136 (1993)
- [95] W. J. Gallagher, S. S. P. Parkin, Y. Lu, X. P. Bian, A. Marley, K. P. Roche, R. A. Altman, S. A. Rishton, C. Jahnes, T. M. Shaw and G. Xiao, *J. Appl. Phys.* **81**, 3741 (1997)
- [96] K. Takano, G. Zeltzer, D. K. Weller and E. E. Fullerton, *J. Appl. Phys.* **87**, 6364 (2000)
- [97] C. M. Schneider, P. Bressler, P. Schuster, J. Kirschner and R. Miranda, *Phys. Rev. Lett.* **64**, 1059 (1990)
- [98] P. Krams, F. Lauks, R. L. Stamps, B. Hillebrands and G. Güntherodt, *Phys. Rev. Lett.* **69**, 3674 (1992)
- [99] J. J. de Miguel, A. Cebollada, J. M. Gallego, R. Miranda, C. M. Schneider, P. Schuster and J. Kirschner, *J. Magn. Magn. Mater.* **93**, 1 (1991)
- [100] J. R. Cerdá, P. L. de Andres, A. Cebollada, R. Miranda, E. Navas, P. Schuster, C. M. Schneider and J. Kirschner, *J. Phys.: Condens. Matter* **5**, 2055 (1993)
- [101] A. K. Schmidt and J. Kirschner, *Ultramicroscopy* **42 - 44**, 483 (1992)
- [102] J. Fassbender, R. Allenspach and U. Dürig, *Surf. Sci.* **383**, L742 (1997)

- [103] U. Ramsperger, A. Vaterlaus, P. Pfäffli, U. Maier and D. Pescia, *Phys. Rev. B* **53**, 8001 (1996)
- [104] M. T. Kief and J. W. F. Egelhoff, *Phys. Rev. B* **47**, 10785 (1993)
- [105] F. Nouvertné, U. May, M. Bammig, A. Rampe, U. Korte, G. Güntherodt, R. Pentcheva and M. Scheffler, *Phys. Rev. B* **60**, 14382 (1999)
- [106] R. Pentcheva and M. Scheffler, *Phys. Rev. B* **61**, 2211 (2000)
- [107] N. A. Levanov, V. S. Stepanyuk, W. Hergert, D. I. Bazhanov, P. H. Dederichs, A. Katsnelson and C. Massobrio, *Phys. Rev. B* **61**, 2230 (2000)
- [108] U. Bovensiepen, P. Pouloupoulos, W. Platow, M. Farle and K. Baberschke, *J. Magn. Magn. Mater.* **192**, L386 (1999)
- [109] P. Bruno, *Magnetic Thin Films, Multilayers, and Surfaces*, in *MRS Proc.*, eds. S. Parkin et al., Vol. 231, p. 299, Pittsburg, Pennsylvania (1992)
- [110] O. Eriksson, A. M. Boring, R. C. Albers, G. W. Fernando and B. R. Cooper, *Phys. Rev. B* **45**, 2868 (1992)
- [111] L. Szunyogh, *private communication* (2000)
- [112] U. Pustogowa, L. Szunyogh, H. Ebert and P. Weinberger, *Solid State Commun.* **108**, 343 (1998)
- [113] J. L. Rodríguez-López, J. Dorantes-Dávila and G. Pastor, *Phys. Rev. B* **57**, 1040 (1998)
- [114] C. Li, A. J. Freeman and C. L. Fu, *J. Magn. Magn. Mater.* **83**, 51 (1990)
- [115] A. J. Freeman and R. Wu, *J. Magn. Magn. Mater.* **100**, 497 (1991)
- [116] R. Wu and A. J. Freeman, *J. Appl. Phys.* **79**, 6500 (1996)
- [117] A. B. Shick, D. L. Novikov and A. J. Freeman, *Phys. Rev. B* **56**, R14259 (1997)
- [118] M. Kim, L. Zhong, X. Wang and A. J. Freeman, *J. Magn. Magn. Mater.* **186**, 277 (1998)
- [119] M. Kim, A. J. Freeman and R. Wu, *Phys. Rev. B* **59**, 9432 (1999)
- [120] V. I. Gavrilenko and R. Wu, *Phys. Rev. B* **60**, 9539 (1999)
- [121] J. A. C. Bland, D. Pescia and R. F. Willis, *Phys. Rev. Lett.* **58**, 1244 (1987)

- [122] R. F. Willis, J. A. C. Bland and W. Schwarzacher, *J. Appl. Phys.* **63**, 4051 (1988)
- [123] J. A. C. Bland, A. D. Johnson, C. Norris and H. J. Lauter, *J. Appl. Phys.* **67**, 5397 (1990)
- [124] V. V. Pasyuk, H. J. Lauter, M. T. Johnson, F. J. A. den Broeder, E. Janssen, J. A. C. Bland and A. V. Petrenko, *Appl. Surf. Sci.* **65/66**, 118 (1993)
- [125] A. Samad, B. C. Choi, S. Langridge, J. Penfold and J. A. C. Bland, *Phys. Rev. B* **60**, 7304 (1999)
- [126] A. Ney, P. Pouloupoulos, M. Farle and K. Baberschke, *Phys. Rev. B* **62**, 11336 (2000)
- [127] W. Weber, C. H. Back, A. Bischof, C. Würsch and R. Allenspach, *Phys. Rev. Lett.* **76**, 1940 (1996)
- [128] U. Kohl, M. Dippel, G. Filleböck, K. Jacobs, B.-U. Runge and G. Schatz, *Surf. Sci.* **407**, 104 (1998)
- [129] R. Allenspach, *J. Magn. Magn. Mater.* **129**, 160 (1994)
- [130] V. L. Moruzzi, *Phys. Rev. Lett.* **57**, 2211 (1986)
- [131] A. Ney, P. Pouloupoulos, F. Wilhelm, A. Scherz, M. Farle and K. Baberschke, *J. Magn. Magn. Mater.*, *in press* (2001)
- [132] A. Ney, P. Pouloupoulos and K. Baberschke, *Europhys. Lett.* **54**, 820 (2001)
- [133] J. Lindner, P. Pouloupoulos, M. Farle and K. Baberschke, *Phys. Rev. B* **62**, 10431 (2000)
- [134] A. Ney, P. Pouloupoulos and K. Baberschke, *submitted to Rev. Sci. Instr.* (2001)
- [135] A. Scherz, F. Wilhelm, P. Pouloupoulos, H. Wende and K. Baberschke, *J. Syn. Rad.* **8**, 472 (2001)
- [136] D. Manske and P. Jensen, *private communication* (2001)
- [137] L. F. Schelp, G. Tosin, M. Carara, M. N. Baibich, A. A. Gomes and J. E. Schmidt, *Appl. Phys. Lett.* **61**, 1858 (1992)
- [138] P. Pouloupoulos, J. Lindner, M. Farle and K. Baberschke, *Surf. Sci.* **437**, 277 (1999)

- [139] J. Shen, J. Giergiel and J. Kirschner, *Phys. Rev. B* **52**, 8454 (1996)
- [140] J. Lindner, P. Pouloupoulos, F. Wilhelm, M. Farle and K. Baberschke, *Phys. Rev. B* **62**, 10431 (2000)
- [141] K. Baberschke, *Appl. Phys. A* **62**, 417 (1996)
- [142] M. Farle, *Rep. Prog. Phys.* **61**, 755 (1998)
- [143] B. Schulz and K. Baberschke, *Phys. Rev. B* **50**, 13467 (1994)
- [144] W. Platow, U. Bovensiepen, P. Pouloupoulos, M. Farle, K. Baberschke, L. Hammer, S. Walter, S. Müller and K. Heinz, *Phys. Rev. B* **59**, 12641 (1999)
- [145] R. Vollmer, T. Gutjahr-Löser, J. Kirschner, S. van Dijken and B. Poelsema, *Phys. Rev. B* **60**, 6277 (1999)
- [146] J. Lindner, *private communication* (2001)
- [147] B. Schulz, *Magnetische Eigenschaften ultradünner Ni/Cu(001)-Filme: Eine Untersuchung mittels ferromagnetischer Resonanz im UHV*, PhD Thesis, Freie Universität Berlin (1995)
- [148] A. Ernst, M. Lueders, W. M. Temmerman, Z. Szotek and G. van der Laan, *J. Phys.: Condens. Matter* **12**, 5599 (2000)
- [149] Z. Yang, V. I. Gavrilenko and R. Wu, *Surf. Sci.* **447**, 212 (2000)
- [150] A. Ney, K. Lenz, P. Pouloupoulos and K. Baberschke, *submitted to J. Magn. Magn. Mater.* (2001)
- [151] U. Bovensiepen, P. Pouloupoulos, M. Farle and K. Baberschke, *Surf. Sci.* **402 - 404**, 396 (1998)
- [152] A. Scherz, *private communication* (2001)
- [153] S. L. Silva, C. R. Jenkins, S. M. York and F. M. Leibsle, *Appl. Phys. Lett.* **76**, 1128 (2000)
- [154] H. Wende, R. Chauvistré, N. Haack, G. Ceballos, F. Wilhelm, K. Baberschke, P. Srivastava and D. Arvanitis, *Surf. Sci.* **465**, 187 (2000)
- [155] H. Wende, *private communication* (2001)

# Publications / Contributions to Conferences

1. P. Srivastava, F. Wilhelm, A. Ney, N. Haack, H. Wende, and K. Baberschke  
*Modifications in the electronic and band structure of 3d single-, bi- and trilayers on Cu(001)*  
Surf. Sci. **402-404**, 818 (1998)
2. P. Srivastava, F. Wilhelm, A. Ney, M. Farle, H. Wende, N. Haack, G. Ceballos, and K. Baberschke  
*Magnetic moments and Curie temperature of Ni and Co thin films and coupled trilayers*  
Phys. Rev. B **58**, 5701 (1998)
3. U. Bovensiepen, F. Wilhelm, P. Srivastava, P. Pouloupoulos, M. Farle, A. Ney, and K. Baberschke  
*Two susceptibility maxima and element specific magnetizations in indirectly coupled ferromagnetic layers*  
Phys. Rev. Lett. **81**, 2368 (1998)
4. F. Wilhelm, P. Srivastava, A. Ney, N. Haack, G. Ceballos, M. Farle, and K. Baberschke  
*Influence of exchange coupling on the Ni magnetization in Co/Cu/Ni trilayers*  
J. Magn. Magn. Mater. **198-199**, 458 (1999)
5. A. Ney, F. Wilhelm, M. Farle, P. Pouloupoulos, P. Srivastava, and K. Baberschke  
*Oscillation of the Curie temperature and interlayer exchange coupling in magnetic trilayers*  
Phys. Rev. B **59**, R 3938 (1999)
6. F. Wilhelm, P. Srivastava, H. Wende, A. Ney, N. Haack, G. Ceballos, M. Farle, and K. Baberschke  
*Magnetism of thin films and in Fe/Ni, Co/Fe bilayers on Cu(001)*  
J. Syn. Rad. **6**, 699 (1999)

7. F. Wilhelm, U. Bovensiepen, A. Scherz, P. Pouloupoulos, A. Ney, H. Wende, G. Ceballos, and K. Baberschke  
*Manipulation of the Curie temperature and the magnetic moments of ultrathin Ni and Co films by Cu-capping*  
J. Magn. Magn. Mater. **222**, 163 (2000)
  8. A. Ney, P. Pouloupoulos, M. Farle, and K. Baberschke  
*Absolute determination of Co magnetic moments: a novel UHV-high-Tc-SQUID magnetometry*  
Phys. Rev. B **62**, 11336 (2000)
  9. A. Ney, P. Pouloupoulos, F. Wilhelm, A. Scherz, M. Farle, and K. Baberschke  
*Absolute determination of the magnetic moments of Co monolayers: A combination of UHV magnetometries*  
J. Magn. Magn. Mater. (in press, 2001)
  10. A. Ney, P. Pouloupoulos, and K. Baberschke  
*Surface and interface magnetic moments of Co*  
Europhys. Lett. **54**, 820 (2001)
  11. A. Ney, P. Pouloupoulos, and K. Baberschke  
*High-Tc UHV-SQUID Magnetometer for Magnetic Monolayers*  
submitted to Rev. Sci. Instr. (2001)
  12. A. Ney, K. Lenz, P. Pouloupoulos, and K. Baberschke  
*Absolute magnetometry on ultrathin 3d-metal films by UHV-SQUID*  
submitted to J. Magn. Magn. Mater. (2001)
- 
1. A. Ney, F. Wilhelm, M. Farle, P. Pouloupoulos, P. Srivastava, and K. Baberschke  
*Oszillationen der Curietemperatur und Interlagenkopplung in Co/Cu/Ni/-Cu(001) Dreilagensystemen*  
Frühjahrstagung der Deutschen Physikalischen Gesellschaft (Münster, 1999)
  2. A. Ney, P. Pouloupoulos, M. Farle, and K. Baberschke  
*SQUID Magnetometrie im UHV an Co/Cu(001) ultradünnen Filmen*  
Frühjahrstagung der Deutschen Physikalischen Gesellschaft (Regensburg, 2000)

3. A. Ney, P. Pouloupoulos, and K. Baberschke  
*Thickness dependence of the Co magnetic moment measured by UHV high- $T_c$ -SQUID*  
International workshop on band-ferromagnetism at finite temperatures (242. WE-Heraeus Seminar) (Wandlitz, 2000)
4. A. Ney, K. Lenz, P. Pouloupoulos, and K. Baberschke  
*Absolute magnetometry on ultrathin 3d-metal films by UHV-SQUID*  
4<sup>th</sup> international conference on metallic multilayers (MML'01) (Aachen, 2001)

# Acknowledgments

A PhD thesis results not only from one single person. Many people contribute to the success, especially during construction of a new machine technicians and workshop-members are of immense value. All members of the “babgroup” were helpful and interested throughout the whole time of the work. I am gratefully indebted to all these persons. My special thanks go to:

**Prof. Dr. K. Baberschke** who gave me the opportunity to start this work in his group. He followed the progress of the novel magnetometer with continuous interest, helpful comments, and valuable discussions.

**Prof. Dr. M. Farle** for the starting ideas of the setup and valuable help and numerous discussions in the early stage of the experiment.

**Prof. Dr. P. Fumagalli** for his willingness to co-asses this thesis and for helpful discussions not only within his group-seminar.

**Prof. Dr. F. Forstmann** for helpful remarks and critical questions concerning the physics of the  $\langle T_z \rangle$  term.

**Dr. Panos Pouloupoulos** for numerous discussions, for valuable help in understanding the results and presenting them, for careful proof-reading of the manuscript (and lots of other manuscripts) and, last but not least, for the excellent STM pictures and nice MOKE loops. Not to forget the nice evenings in the far-out of Teltow ...

**Jürgen Lindner and Ramona Nünthel** for various discussions, comments and for proof-reading of the manuscript. Not to forget the great time we had, not only in Chandolino. Just thinking of nice evenings including theater, soccer and beer ...

**Christoph Rüdtt** not only for seaching hundreds of “typos” but also for Ver-breiten von schwäbischer Gemütlichkeit.

**Kilian Lenz** for taking over all the stuff that fast - it seems to work well ... Good luck! Unfortunately, we won't be out for Chandolino.

**Andreas Scherz, Heiko Wende and the whole BESSY crew** for a great time during the Diploma, for relinquishing the good old BESSY-chamber for the new SQUID, and for a close look and various helpful comments on this work.

**Ela Kosubek** for being all the time that helpful and friendly, keeping everything nice and fine, and for telling some secrets about Corel.

**Wolfgang Wisny** not only because of the great motor-control unit but also for explaining or repairing broken electronics or just talking about life and its “Inponderabilien”.

**The F. I. T.** for the SQUID, technical assistance and generous help in solving various problems.

**Jon Tobias Hoeft and Franziskus Heigl** for being physicists and forgetting about that in the evenings . . . Jon, I hope, that we will stay here in Berlin for a while!

**my parents** for generous help and support all the time during my studies. Without them not a single page of this work would exist — thanks a lot, Ma and Pa!!!

and finally . . .

**Verena** for just being there, for sunshine on rainy days, for support which DFG can not provide, and for bearing me all the time (hard job!).

# Curriculum vitae

## I. Personal Data

Name: Andreas Ney

Nationality: German

Place and Date of Birth: Bad Homburg v. d. H., July 21<sup>th</sup>, 1972

Permanent Address: Freie Universität Berlin  
Institut für Experimentalphysik  
Arnimallee 14  
D-14195 Berlin  
Germany  
Tel.: +49-30-838 56143  
Fax.: +49-30-838 53646  
email: ney@physik.fu-berlin.de

## II. Educational Qualifications/Research Experience

summer 1979 to  
summer 1983                      Elementary school “Grundschule Oberhöchstadt” in  
Kronberg i. Ts.

summer 1983 to  
summer 1992                      Gymnasialzweig “Altkönigschule Kronberg” in  
Kronberg i. Ts.

May 25<sup>th</sup>, 1992                      Abitur.

summer 1992 to  
summer 1993                      “Grundwehrdienst” (military service) in  
Tauberbischofsheim.

since winter 1993                      Studies of physics at the Freie Universität Berlin.

April 7<sup>th</sup>, 1995                      “Diplom-Vorprüfung” (pre-diploma) in physics

October 1996 to September 1998	Tutor in the laboratory course in physics for medicine students
August 1997 to November 1997	Internaship at BMW–Rolls Royce in Dahlewitz.
August 1996 to April 1998	Diploma thesis “ <i>Magnetischer Röntgenzirkular- dichroismus an Ein-, Zwei- und Dreifachschichten der 3d Übergangsmetalle</i> ” at the Institut für Experimentalphysik, Freie Universität Berlin; advisor: Prof. Dr. K. Baberschke
April 9 <sup>th</sup> , 1998	“Diplom” in physics
from June 1998	Started Ph. D. work in Prof. Dr. K. Baberschke’s group

# Zusammenfassung

In der vorliegenden Arbeit wird der Aufbau eines neuartigen UHV kompatiblen hoch- $T_c$  SQUID Magnetometers beschrieben. Es bietet die Möglichkeit, innerhalb weniger Minuten *in situ* im UHV die Magnetisierung mit hoher Genauigkeit ( $\sim 5\%$ ) und Empfindlichkeit ( $\leq 0.3$  ML) zu bestimmen. Dabei kann die Proben-temperatur zwischen 40 und 300 K betragen. Die Präparation und Charakterisierung erfolgt mittels Standardtechniken da für die Probenmanipulation ebenfalls übliches UHV Zubehöhr verwendet werden kann. Die Kalibration des Magnetometers ist unabhängig vom untersuchten ferromagnetschen Material und wird mit einer Spule und Anwendung des Gesetzes von Biot-Savart erreicht. In diesem Sinne liefert das Magnetometer die gemessene Magnetisierung in absoluten Einheiten.

Dicken- und temperaturabhängige Messungen an Co/Cu(001) ultradünnen Filmen demonstrieren die Leistungsfähigkeit des Magnetometers, die Zuverlässigkeit und Reproduzierbarkeit der Ergebnisse. Ein kompletter Satz magnetischer Grundzustandsmomente kann nun die Lücke zwischen älteren Arbeiten an dicken Filmen und neueren an 2 ML Filmen schließen. Man erhält ein volumenkristallartiges magnetisches Moment von  $1.73(7)\mu_B$  pro Atom für Filme dicker als 8 Lagen und ein um 10% erhöhtes Moment von  $1.89(8)\mu_B$  pro Atom bei 2 Lagen. Ferner konnte das gemessene magnetische Moment in seine Spin- und Bahnbeiträge aufgespalten werden, indem frühere XMCD-Messungen des Verhältnisses der beiden Größen verwendet wurden. Die beobachtete Erhöhung des magnetischen Moments wird durch einem Anstieg des Bahnmoments um einen Faktor 2 verursacht. Dies ist mit einem signifikanten "Unquenching" des Bahnmoments aufgrund der reduzierten Symmetrie an der Oberfläche erklärbar, d.h. mit einer niedrigeren Koordinationszahl der Atome an der Oberfläche verglichen mit dem Volumen. Das magnetische Moment steigt linear mit der inversen Filmdicke an. Dies legt nahe, daß es sich bei der Erhöhung um einen kombinierten Oberflächen- und Grenzflächeneffekt handelt. Oberflächen- und Grenzflächenbeiträge konnten voneinander getrennt werden, indem die Magnetisierung vor und nach dem Bedecken eines Co-Films mit einer Cu-Deckschicht gemessen wurde. Man erhält ein magnetisches Profil der Co-Filme, wobei die inneren Lagen wie der Volumenkristall ( $1.73\mu_B/\text{Atom}$ ) magnetisiert sind, während die Oberflächenlage ein stark erhöhtes Moment von  $2.28(8)\mu_B/\text{Atom}$  hat und die Grenzflächenlage eine

ausgeprägte Reduktion auf  $1.43(5)\mu_B/\text{Atom}$  aufweist. Die Ergebnisse sind konsistent mit neueren theoretischen Berechnungen.

Dank der hohen Empfindlichkeit des UHV-SQUIDs und der Zugänglichkeit von tiefen Temperaturen konnten metastabile magnetische Eigenschaften von Co/Cu(001) Filmen unterhalb von 2 ML untersucht werden. Diese werden im Vergleich mit neueren “total-energy” Rechnungen und einer STM Untersuchung diskutiert. Es wird eine Phasenseparation von Co und Cu vorgeschlagen, die durch leichtes Heizen verursacht wird.

In einem zweiten Schritt sind die Experimente auf Ni-Filme ausgedehnt worden. Es sind bisher nur erste Ergebnisse vorhanden, die eine dem Volumenkristall vergleichbare Magnetisierung (528 kA/m) der Filme zwischen 4 und 9 Lagen zeigen. Der Einfluß einer Cu-Deckschicht ist unterhalb 5 ML Filmdicke vernachlässigbar klein, während bei 4 ML eine 20%ige Reduktion beobachtet wird. Eine erste Messung an einem senkrecht magnetisierten Film ist auch gezeigt. Die gefundene Orientierung und der Wert der Magnetisierung sind in Übereinstimmung mit neueren experimentellen und theoretischen Arbeiten. Diese ersten Resultate zeigen nicht nur, daß das Magnetometer nicht an Co-Filme gebunden ist, sondern auch, daß es empfindlich genug ist, sogar ultradünne Ni-Filme zu untersuchen.

Für zukünftige Experimente bietet sich die Möglichkeit, den Einfluß der Präparationsbedingungen auf die magnetischen Eigenschaften direkt *in situ* zu untersuchen. Es ist bekannt, daß 2 ML Co, die auf einem N<sub>2</sub> gesputterten Cu-Substrat aufgewachsen werden, punkt- oder streifenähnliche Strukturen bilden [153]. Solche Filme sollten aufgrund der niedrigeren Koordinationszahl der Oberflächenatome im Vergleich zu glatten Filmen eine erhöhte Magnetisierung aufweisen. Im Falle von Ni ist kürzlich mittels FMR beobachtet worden, daß O<sub>2</sub> als “Surfactant” wirkt und sich daher die magnetische Anisotropie von Ni auf einem voroxidierten Cu(001) Kristall ändert [146]. Das UHV-SQUID kann hierbei Messungen der magnetischen Moments beisteuern. Es ist weiterhin möglich, die Änderung der magnetischen Eigenschaften von Ni-Filmen zu untersuchen, wenn die Oberfläche durch Kohlenstoff rekonstruiert wird [154, 155]. All diese Beispiele zeigen, daß es eine Vielzahl weiterer, interessanter Anwendungen für das neue UHV-SQUID gibt.

Im Vergleich mit anderen, etablierten Techniken wie AGM oder TOM bietet das neue UHV-SQUID keine Möglichkeit zur Untersuchung der Feldabhängigkeit der Magnetisierung und damit der magnetischen Anisotropie. Auf der anderen Seite bietet es Zugang zu tiefen Temperaturen bis hinab zu 40 K und ermöglicht schnelle und hochempfindliche Messungen. Darüberhinaus gewährleistet das Design des Magnetometers einfache Kombination mit anderen Meßmethoden. Es ist speziell für die UHV-Kammern geeignet, die Messungen der Ferromagnetischen Resonanz (FMR), MOKE, XMCD oder STM dienen. Das Magnetometer ist eine außerordentlich preiswerte Methode zur Charakterisierung von wie-gewachsenen, ultra-dünnen Filmen und kann zusätzlich als Kalibrierreferenz für MOKE oder FMR verwendet werden. Seine hohe Empfindlichkeit und die Verwendung

von üblichen Probenhaltern bietet die Möglichkeit, in Verbindung mit XMCD-Messungen an ein und demselben Film die Gültigkeit der XMCD-Summenregeln an dünnen Filme direkt zu überprüfen. Eine indirekte Überprüfung gelang bereits in der vorliegenden Arbeit. Zusammenfassend kann man sagen, daß die diskutierten Merkmale des neuartigen UHV-SQUID Magnetometers viele verschiedenartige Anwendungen auf dem Gebiet der Dünnschichtmagnetometrie versprechen.